TOPICS IN THEORETICAL ASTROPHYSICS: PRECESSION OF WARPED DISKS, OSCILLATIONS OF PRESUPERNOVA STARS, AND THERMAL EVOLUTION AND NUCLEOSYNTHESIS OF YOUNG NEUTRON STARS

A Dissertation

Presented to the Faculty of the Graduate School

of Cornell University

in Partial Fulfillment of the Requirements for the Degree of

Doctor of Philosophy

by

Akiko Shirakawa

May 2007

TOPICS IN THEORETICAL ASTROPHYSICS: PRECESSION OF WARPED DISKS, OSCILLATIONS OF PRESUPERNOVA STARS, AND THERMAL EVOLUTION AND NUCLEOSYNTHESIS OF YOUNG NEUTRON STARS

Akiko Shirakawa, Ph.D.

Cornell University 2007

This thesis consists of three parts. In the first part, we study the magnetically driven precession of warped disks. An accretion disk around a rotating magnetized star is subjected to the magnetic torques that induce warping and precession of the disk. We study the global hydrodynamical warping/precession modes of the disk under the combined influences of the magnetic torques, relativistic frame dragging, and the classical precession due to oblateness of the neutron star. We apply our analysis to two types of accreting systems: low-mass X-ray binaries (LMXBs) and accreting X-ray pulsars. We argue that some features of low-frequency quasi-periodic oscillations (QPOs) in LMXBs and milli-Hertz QPOs in accreting X-ray pulsars can be explained by the magnetically driven precession of warped disks.

The second part is related to the hydrodynamically-driven mechanism for asymmetric supernova explosions / neutron star kicks. We explore the possibility that the gravity modes in the core of a presupernova star may be amplified in the silicon burning shell to produce the global asymmetric perturbations that lead to an

asymmetric supernova explosion. By performing a linear analysis of the oscillations in the cores of presupernova stars, we estimate the growth/damping rates of the modes. We find that most of the modes are damping modes with a few exceptions. We also find that, even for a growing mode, the timescale of mode growth is much longer than the remaining time before the core collapse. We conclude that the gravity modes in a presupernova core cannot provide the global asymmetric perturbations that lead to an asymmetric supernova explosion.

In the last part, we attempt to predict the innate chemical composition of a neutron star atmosphere. There has been great progress in X-ray observations and now thermal radiation from neutron stars is being studied in detail. There has also been significant progress in modeling thermal spectra from neutron stars. However, the unknown chemical composition of the neutron star surface is assumed in these models. Our goal is to predict the chemical composition of a neutron star atmosphere by evolving its thermal structure and the chemical composition from the earliest possible time. We study necessary steps to achieve this goal. We study models for a static atmosphere of a young neutron star, cooling of the bulk of a young neutron star, the nuclear statistical equilibrium abundances, nucleosynthesis, and the possible role of diffusion.

BIOGRAPHICAL SKETCH

Akiko Shirakawa was born in Osaka, Japan. She majored in physics at Kyoto University and graduated in March 1998. She came to Cornell University in the summer of 1998 to pursue a Ph.D. in theoretical astrophysics.

To my husband Takuya

ACKNOWLEDGEMENTS

First and foremost, I would like to thank my advisor Dong Lai for his tremendous educational support throughout my graduate study. He has been an excellent advisor who is truly committed to students' development. Without his guidance, none of this work would have been possible.

I am fortunate to have had other helpful faculty members around me. David Chernoff, Éanna Flanagan, and Ira Wasserman have always been willing to offer me help when I needed it. Éanna, Ira, and Jim Alexander have been on my Special Committee. I am thankful to them all. I would also like to thank Frank Timmes for generously providing me with some of his numerical codes and answering my numerous questions.

The sixth floor of the Space Sciences Building has been a wonderful place to work filled with many interesting people. I thank my fellow graduate students: Ali, Andy, Bjoern, Dave, Étienne, Harald, Jeandrew, John, Katrin, Marc, Mark, Marko, Matt, Min, Paul, Phil, Steve, Taner, Wolfgang, Wynn, and Zach, and our great postdocs: Deirdre, Larry, and Tom.

I would like to thank the friends I have made during the time of my graduate study: Nozomi Ando, Rie Kubota Ando, Oleg Evnin, Xiaoli Guo, Richard Hill, Lauren Hsu, Sachiko Hyakutake, Hee Jung, Michiko Kudoh, Dae-Sik Moon, Jun Ohashi, Yoko Ohashi, and Richard Yeh.

I give my heartfelt thanks to my family and friends in Japan. I am lucky to have such great parents who have cared so much about me and have supported some of my adventurous decisions (e.g., going to the United States to study theoretical astrophysics). I will be forever grateful to them. I also would like to thank my sister Tomoko for being such a good friend. I cannot help but mention and thank

my grandmother Sumiko and my late-grandparents.

Last but not the least, I would like to thank my husband and best friend Takuya. He has put up with a lot. Somehow he has always believed in me. Without his faith in me, this thesis would not have been possible.

TABLE OF CONTENTS

LIST OF TABLES

LIST OF FIGURES

Chapter 1

Magnetically Driven Precession of Warped Disks and Low-Frequency QPOs in Low-Mass X-Ray Binaries

1.1 Introduction

Accreting neutron stars (NSs) in low-mass X-ray binaries (LMXBs) exhibit rapid, quasi-periodic oscillations (QPOs) in their X-ray fluxes. The so-called horizontal-branch oscillations (HBOs), discovered in a subclass of LMXBs called Z sources, are low-frequency QPOs (LFQPOs) with centroid frequencies in the range of 15-60 Hz, Q-values of order a few, and rms amplitudes $\lesssim 10$ % (see van der Klis 1995 for a review). One interpretation of the HBOs is the magnetospheric beat-frequency model (Alpar & Shaham 1985; Lamb et al. 1985) in which the HBO frequency is identified with the difference frequency between the Keplerian frequency at the magnetospheric boundary and the spin frequency of the NS. However, over the last few years, the discovery of kilohertz (300–1300 Hz) QPOs in ~ 20 LMXBs by the *Rossi X-Ray Timing Explorer* (*RXTE*) has called into question this interpretation of the HBOs (see van der Klis 2000 for a review). In particular, observations indicate that in most Z sources, kHz QPOs (which often come in pairs) occur simultaneously with the HBOs. In several atoll sources (which are thought to have weaker magnetic fields and smaller accretion rates than the Z sources), similar LFQPOs have also been found at the same time when kHz QPOs occur. While the origin of the kHz QPOs is still being debated, it is convenient (as in all current

theoretical models; see van der Klis 2000 and references therein) to associate one of the kHz peaks with the orbital motion in the inner edge of the accretion disk. On the other hand, the discovery of nearly coherent oscillations during X-ray bursts in several LMXBs establishes the spin frequency of the NS to be $\sim$ 300–600 Hz (see Strohmayer 2000). Obviously, the beating between the kHz orbital frequency and the spin frequency cannot produce the 10–60 Hz LFQPOs.

Stella & Vietri (1998) suggested that the LFQPOs are associated with the Lense-Thirring precession of the inner accretion disk around the rotating NS. If the LFQPO and the kHz QPOs are generated at the same special radius in the disk, this implies a quadratic relation between the LFQPO frequency and the kHz QPO frequency, in rough agreement with observations (usually for certain range of X-ray fluxes; but see §4.4). For reasonable values of NS moment of inertia, the data require that the observed LFQPO peaks correspond to 2 or 4 times the Lense-Thirring frequency (Stella & Vietri 1998; Ford & van der Klis 1998; Psaltis et al. 1999); this may be possible since a precessing disk may induce X-ray flux variation mainly at the harmonics of its fundamental precession frequency and there may be "sub-harmonic" feature buried in the X-ray power spectra (see Jonker et al. 2000).

There are several theoretical and observational puzzles associated with the Lense-Thirring interpretation of LFQPOs. First, it is well-known that the combined effects of differential precession and viscosity tend to keep the inner region of the disk [within $\sim (100-1000)GM/c^2$] perpendicular to the NS spin axis (Bardeen & Petterson 1975). A mechanism to drive the disk tilt is then needed for the precession to make sense. Second, because different "rings" in the disk have different precession rates and are strongly coupled to each other, a global mode analysis is needed to determine the true precession rate of the inner disk. Marković & Lamb

(1998) carried out such an analysis but found that all the modes are damped even when the radiation driven warping torque (Pringle 1996) is included. Third, pure Lense-Thirring precession has difficulty in explaining the observed behavior of the LFQPO frequency as a function of the accretion rate of the system (Wijnands et al. 1996; Psaltis et al. 1999; see §4.4).

In this chapter, we show that the magnetically driven warping instability (Lai 1999), resulting from interactions between the weakly magnetized ($\sim 10^8$ G) NS and the inner accretion disk (see §2), can naturally overcome the Bardeen-Petterson viscous damping and therefore induces a tilt in the inner disk. By carrying out a global analysis of disk precession/warping modes, including magnetic torques in addition to the Lense-Thirring and classical precession torques, we obtain, for the first time, growing warping/precession modes of the disk (see §3 and §4). Moreover, we show that the magnetically driven precession torque (Lai 1999; see §2) significantly affects the actual disk precession frequency as the accretion rate increases; this can potentially explain the observed $\dot{M}$-dependent behaviors of the LFQPOs (§4).

This chapter is based on the published paper by Shirakawa & Lai 2002 [Shirakawa, A. & Lai D. 2002, The Astrophysical Journal, 564, 361;] It is reprinted here with minor changes, based on rights retained by the author.

1.2 Magnetically Driven Warping and Precession

It is known that if the accretion disk is slightly tilted from the equatorial plane of a rotating neutron star, it precesses due to general relativistic frame-dragging effect (Lense-Thirring precession) and also due to oblateness of the rotating star

(classical precession). For a magnetized neutron star, there is an additional magnetically driven precession and warping of the disk; these arise from interactions between the stellar magnetic field and the disk before the latter is truncated at the magnetospheric boundary (Lai 1999). The magnetic torques appear under the generic condition that the stellar magnetic field (treated as a dipole here) is not aligned with the stellar spin axis. Depending on how the disk responds to the stellar field, two different kinds of torque arise: (i) If the vertical stellar magnetic field B_z penetrates the disk, it gets twisted by the disk rotation to produce an azimuthal field $\Delta B_\phi = \mp\zeta B_z$ that has different signs above and below the disk (ζ is the azimuthal pitch of the field line and depends on the dissipation in the disk), and a radial surface current K_r results. The interaction between K_r and the stellar B_ϕ gives rise to a vertical force. While the mean force (averaging over the azimuthal direction) is zero, the uneven distribution of the force induces a net *warping torque* which tends to misalign the angular momentum of the disk with the stellar spin axis. (ii) If the disk does not allow the vertical stellar field (e.g., the rapidly varying component of B_z due to stellar rotation) to penetrate, an azimuthal screening current K_ϕ will be induced on the disk. This K_ϕ interacts with the radial magnetic field B_r and produces a vertical force. The resulting *precessional torque* tends to drive the disk into retrograde precession around the stellar spin axis.

In general, both the magnetic warping torque and the precessional torque are present. For small disk tilt angle β (the angle between the disk normal and the spin axis), the warping rate and precession angular frequency at radius r are given by (see Lai 1999)

$$\Gamma_m(r) = \frac{\zeta\mu^2}{4\pi r^7 \Omega(r)\Sigma(r)} \cos^2\theta, \tag{1.1}$$

and

$$\Omega_m(r) = -\frac{\mu^2}{\pi^2 r^7 \Omega(r)\Sigma(r)D(r)}\sin^2\theta, \tag{1.2}$$

where μ is the stellar magnetic dipole moment, θ is the angle between the magnetic dipole axis and the spin axis, $\Omega(r)$ is the orbital angular frequency, and $\Sigma(r)$ is the surface density of the disk. The dimensionless function $D(r)$ is given by

$$D(r) = \max\,(\sqrt{r^2/r_{\rm in}^2 - 1}, \sqrt{2H(r)/r_{\rm in}}), \tag{1.3}$$

where $H(r)$ is the half-thickness and $r_{\rm in}$ is the inner radius of the disk.

Here we apply these magnetic torques to LMXBs containing weakly magnetized ($B \sim 10^8$ G) NSs. We parametrize the properties of the inner disk using the "inner region" (radiation- and-scattering dominated) solution of α-disk (Shakura & Sunyaev 1973)[1], with

$$\Sigma(r) = (1050\ {\rm g\ cm^{-2}})\alpha_{-1}^{-1}M_{1.4}^{-1/2}\dot{M}_{17}^{-1}r_6^{3/2}\mathcal{J}(r)^{-1}, \tag{1.4}$$

$$H(r) = (1.1\ {\rm km})\dot{M}_{17}\mathcal{J}(r), \tag{1.5}$$

where $\alpha = (0.1)\alpha_{-1}$ is the α-viscosity, $M = (1.4M_\odot)M_{1.4}$ is neutron star's mass, $\dot{M} = (10^{17}\,{\rm g\,s^{-1}})\dot{M}_{17}$ is the mass accretion rate and $r_6 = r/(10^6\,{\rm cm})$. The dimensionless function $\mathcal{J}(r)$ is given by [2]

$$\mathcal{J}(r) = 1 - \xi\sqrt{\frac{r_{\rm in}}{r}}, \tag{1.6}$$

[1]Such a disk is unstable against thermal-viscous perturbations (see Frank et al. 1992), although the situation is not clear when there are magnetic fields threading the disk. Note that our main results related to the dimensionless mode frequencies (see §4.1 and §4.2) are not very sensitive to disk models (see Shirakawa & Lai 2001, where general power-law disks are studied).

[2]Magnetic fields threading the disk can modify $\mathcal{J}(r)$ in a model-dependent way (see Lai 1999 for an example). However, the basic feature can still be approximated by eq. (1.6).

where ξ is a dimensionless parameter with $0 < \xi < 1$. Substituting equations (1.4) and (1.5) into equations (1.1) and (1.2), and assuming the Keplerian flow for $\Omega(r)$, we get

$$\Gamma_m(r) = (55.3\ \mathrm{s}^{-1})\,\zeta\cos^2\theta\alpha_{-1}\mu_{26}^2\dot{M}_{17}\mathcal{J}(r)\,r_6^{-7}, \tag{1.7}$$

$$\Omega_m(r) = (-70.4\ \mathrm{s}^{-1})\sin^2\theta\alpha_{-1}\mu_{26}^2\dot{M}_{17}D(r)^{-1}\mathcal{J}(r)\,r_6^{-7}, \tag{1.8}$$

where $\mu_{26} = \mu/(10^{26}\,\mathrm{G\,cm}^3)$.

The Lense-Thirring precession angular frequency is given by [3]

$$\Omega_{LT}(r) = \frac{2GI_3\Omega_s}{c^2r^3} = (280\ s^{-1})I_{45}\left(\frac{\nu_s}{300\ \mathrm{Hz}}\right)r_6^{-3}, \tag{1.9}$$

where $I_3 = (10^{45}\ \mathrm{g\,cm}^2)I_{45}$ is the moment of inertia around the spin axis and $\Omega_s = 2\pi\nu_s$ is the spin angular frequency. The classical precession angular frequency is given by

$$\Omega_{\mathrm{cl}}(r) = -\frac{3G(I_3 - I_1)}{2r^3}\frac{\cos\beta}{\sqrt{GMr}}, \tag{1.10}$$

where I_1 is the moment of inertia around the axis perpendicular to the spin. If we approximate the rotating NS as a compressible Maclaurin spheroid (Lai et al. 1993), we have $I_3 = (1/5)\kappa_n M(a_1^2 + a_2^2)$ and $I_1 = (1/5)\kappa_n M(a_2^2 + a_3^2)$, where a_i is the semi-major axis of the spheroid, and κ_n is a dimensionless parameter which depends on the polytropic index (e.g., κ_n=1, 0.81482, 0.65345 for n=0, 0.5, 1, respectively). For slow rotation, with $\hat{\Omega}_s \equiv \Omega_s/(GM/R^3)^{1/2} \ll 1$ (where R is the radius of a nonrotating star of the same mass), the semi-major axis is given by

[3] In the strong gravitational field and/or rapid stellar rotation regime, the Lense-Thirring precession (angular) frequency is replaced by the nordal precession frequency $\Omega_{\mathrm{nod}} \equiv \Omega - \Omega_\theta$ with Ω the orbital frequency and Ω_θ the vertical frequency. The fractional deviation of Ω_{nod} from Ω_{LT} is of order $\hat{a}(M/r)^{1/2}$ (where $\hat{a} = I\Omega_s/M^2$) and will be neglected in our discussions.

$a_i = R(1+\epsilon_i)$, with (Lai et al. 1994; Appendix A)

$$\epsilon_1 = \epsilon_2 = \frac{1}{4}\kappa_n\left(1-\frac{n}{5}\right)\left(\frac{5+n}{3-n}\right)\hat{\Omega}_s^2, \tag{1.11}$$

$$\epsilon_3 = -\frac{1}{2}\kappa_n\left(1-\frac{n}{5}\right)\left(\frac{5-3n}{3-n}\right)\hat{\Omega}_s^2. \tag{1.12}$$

Equations (1.9) and (1.10) then become (with $\cos\beta \simeq 1$)

$$\Omega_{LT}(r) = (313\ \mathrm{s}^{-1})\kappa_n\left[1+\frac{1}{2}\kappa_n\left(1-\frac{n}{5}\right)\left(\frac{5+n}{3-n}\right)\hat{\Omega}_s^2\right]\left(\frac{\nu_s}{300\ \mathrm{Hz}}\right)M_{1.4}R_6^2 r_6^{-3}, \tag{1.13}$$

$$\Omega_{\rm cl}(r) = (-195\ \mathrm{s}^{-1})\kappa_n^2\left(1-\frac{n}{5}\right)\left(\frac{\nu_s}{300\ \mathrm{Hz}}\right)^2 M_{1.4}^{-1/2}R_6^5 r_6^{-7/2}, \tag{1.14}$$

where $R_6 = R/(10^6\,\mathrm{cm})$. Morsink & Stella (1999) have given exact numerical solutions of Ω_{LT} and $\Omega_{\rm cl}$ for a variety of nuclear equations of state. But analytic expressions (1.13) and (1.14) provide the dominant contributions, and are adequate for the purpose of our work.

1.3 Global Precession/Warping Modes: Equations

Since the precession rates $\Omega_{LT}, \Omega_{\rm cl}, \Omega_m$ depend strongly on r, coupling between different rings is needed to produce a global coherent precession. Such coupling can be achieved through either viscous stress or bending waves (e.g., Papaloizou & Pringle 1983; Terquem 1998 and references therein). In the viscosity dominated regime, the formalism of Papaloizou & Pringle (1983) can be used (see also Pringle 1992; Ogilvie 2000; Ogilvie & Dubus 2001; note that in the linear regime, the different formalisms of disk warping dynamics are equivalent). We specify a warped precessing disk by the disk normal vector $\hat{\mathbf{l}}(r,t)$. In the Cartesian coordinate, with the z-axis along the NS spin, we write $\hat{\mathbf{l}} = (\sin\beta\cos\gamma, \sin\beta\sin\gamma, \cos\beta)$, with $\beta(r,t)$ the tilt angle and $\gamma(r,t)$ the twist angle. For $\beta \ll 1$, the dynamical warp equation

for $\hat{\mathbf{l}}$ (see Lai 1999) reduces to an equation for $W(r,t) \equiv \beta(r,t)e^{i\gamma(r,t)}$:

$$\frac{\partial W}{\partial t} - \left[\frac{3\nu_2}{4r}\left(1 + \frac{2r\mathcal{J}'}{3\mathcal{J}}\right) + \frac{3\nu_1}{2r}(\mathcal{J}^{-1} - 1)\right]\frac{\partial W}{\partial r} = \frac{1}{2}\nu_2\frac{\partial^2 W}{\partial r^2} + i\left(\Omega_{LT} + \Omega_{\rm cl} + \Omega_m\right)W + \Gamma_m W, \tag{1.15}$$

where ν_2 is the viscosity which tends to reduce the disk tilt. We assume that the ratio of ν_2 to the usual viscosity ν_1 is constant. For α disk, $\nu_1 = \alpha H^2\Omega$, the viscosity rate is

$$\tau_{\rm visc}^{-1}(r) \equiv \frac{\nu_2(r)}{r^2} = (16.7\ {\rm s}^{-1})\left(\frac{\nu_2}{\nu_1}\right)\alpha_{-1}M_{1.4}^{1/2}\dot{M}_{17}^2\mathcal{J}(r)^2\, r_6^{-7/2}. \tag{1.16}$$

To look for global modes we consider solutions of the form $W(r,t) = e^{i\sigma t}W(r)$ with the complex mode frequency σ $(= \sigma_r + i\sigma_i)$. It is convenient to define a dimensionless mode frequency $\hat{\sigma} = \sigma\tau_{\rm visc}(r_{\rm in})$, where $\tau_{\rm visc}(r_{\rm in})$ is given by eq. (1.16) evaluated at $r_{\rm in}$, the inner disk radius. Similarly, we define dimensionless quantities:

$$\begin{aligned}
\hat{\Omega}_{LT} &\equiv \Omega_{LT}(r_{\rm in})\tau_{\rm visc}(r_{\rm in}) \\
&= 16.8\, I_{45}\left(\frac{\nu_s}{300\ {\rm Hz}}\right)\left(\frac{\nu_1}{\nu_2}\right)\alpha_{-1}^{-1}M_{1.4}^{-1/2}\dot{M}_{17}^{-2}\mathcal{J}_{\rm in}^{-2}\left(\frac{r_{\rm in}}{10{\rm km}}\right)^{1/2}, \qquad (1.17)\\
\hat{\Omega}_{\rm cl} &\equiv \Omega_{\rm cl}(r_{\rm in})\tau_{\rm visc}(r_{\rm in}) \\
&= -11.7\,\kappa_n^2\left(1 - \frac{n}{5}\right)\left(\frac{\nu_s}{300\ {\rm Hz}}\right)^2\left(\frac{\nu_1}{\nu_2}\right)\alpha_{-1}^{-1}M_{1.4}^{-1}\dot{M}_{17}^{-2}R_6^5\mathcal{J}_{\rm in}^{-2}, \qquad (1.18)\\
\hat{\Omega}_m &\equiv \Omega_m(r_{\rm in})\tau_{\rm visc}(r_{\rm in}) \\
&= -4.2\,\sin^2\theta\left(\frac{\nu_1}{\nu_2}\right)\mu_{26}^2M_{1.4}^{-1/2}\dot{M}_{17}^{-1}D_{\rm in}^{-1}\mathcal{J}_{\rm in}^{-1}\left(\frac{r_{\rm in}}{10{\rm km}}\right)^{-7/2}, \qquad (1.19)\\
\hat{\Gamma}_m &\equiv \Gamma_m(r_{\rm in})\tau_{\rm visc}(r_{\rm in}) \\
&= 3.3\,\zeta\cos^2\theta\left(\frac{\nu_1}{\nu_2}\right)\mu_{26}^2M_{1.4}^{-1/2}\dot{M}_{17}^{-1}\mathcal{J}_{\rm in}^{-1}\left(\frac{r_{\rm in}}{10{\rm km}}\right)^{-7/2}, \qquad (1.20)
\end{aligned}$$

where $D_{\rm in} \equiv D(r_{\rm in})$ and $\mathcal{J}_{\rm in} \equiv \mathcal{J}(r_{\rm in})$. Note that we can use eq. (1.13) to obtain more explicit expression of $\hat{\Omega}_{LT}$. Equation (1.15) can now be reduced to the

dimensionless form:

$$i\hat{\sigma}W - \left[\frac{3}{4x^{5/2}}\left(1+\frac{2x\mathcal{J}'}{3\mathcal{J}}\right)+\frac{3}{2x^{5/2}}\left(\frac{\nu_1}{\nu_2}\right)(\frac{1}{\mathcal{J}}-1)\right]\frac{\mathcal{J}^2}{\mathcal{J}_{\rm in}^2}\frac{dW}{dx}$$
$$= \frac{1}{2x^{3/2}}\frac{\mathcal{J}^2}{\mathcal{J}_{\rm in}^2}\frac{d^2W}{dx^2}+i\left[\frac{\hat{\Omega}_{LT}}{x^3}+\frac{\hat{\Omega}_{\rm cl}}{x^{7/2}}+\frac{\hat{\Omega}_m}{x^7}\frac{D_{\rm in}}{D}\frac{\mathcal{J}}{\mathcal{J}_{\rm in}}\right]W+\frac{\hat{\Gamma}_m}{x^7}\frac{\mathcal{J}}{\mathcal{J}_{\rm in}}W, \quad (1.21)$$

where $x \equiv r/r_{\rm in}$ and $\mathcal{J}' = d\mathcal{J}/dx$.

It is clear from eq. (1.21) that $\hat{\sigma}$ depends only on five dimensionless parameters $\hat{\Omega}_{LT}$, $\hat{\Omega}_{\rm cl}$, $\hat{\Omega}_m$, $\hat{\Gamma}_m$, and ν_1/ν_2 as well as two dimensionless functions $D(x)$ and $\mathcal{J}(x)$. To obtain σ in physical units we need to know $r_{\rm in}$. We adopt the simple ansatz:

$$r_{\rm in} = \max(r_m, r_{\rm ISCO}), \quad (1.22)$$

where the magnetosphere radius r_m is given by

$$r_m = 18\,\eta\,\mu_{26}^{4/7}M_{1.4}^{-1/7}\dot{M}_{17}^{-2/7}\ {\rm km}, \quad (1.23)$$

(with $\eta \sim 0.5$), and the inner-most stable circular orbit [4] $r_{\rm ISCO}$ is given by

$$r_{\rm ISCO} = 6GM/c^2 = 12.4\,M_{1.4}\ {\rm km}. \quad (1.24)$$

The critical mass accretion rate $\dot{M}_{17,\,\rm c}$ below which $r_{\rm in} = r_m$ and above which $r_{\rm in} = r_{\rm ISCO}$ is obtained by equating eqs. (1.23) and (1.24) as:

$$\dot{M}_{17,\,\rm c} = 3.7\,\eta^{7/2}\mu_{26}^2M_{1.4}^{-4}. \quad (1.25)$$

A more elaborate prescription for the inner disk radius when both general relativity and the magnetic field are important is discussed in Lai (1998).

To solve eq. (1.21) for the complex eigenfunction $W(x)$ and eigenvalue $\hat{\sigma}$, six real boundary conditions are needed. In our calculation, the disk extends from

[4] The correction to $r_{\rm ISCO}$ due to stellar rotation is negligible since $\hat{a} \sim 0.1$ for NSs in LMXBs.

$x_{\rm in} = 1$ to $x_{\rm out} = 50$. For large x and large $|\hat{\sigma}|$, equation (1.21) can be solved analytically, giving

$$W(x) \propto \exp\left[\frac{4\sqrt{2}}{7}\,(i\hat{\sigma})^{1/2}\mathcal{J}_{\rm in}x^{7/4}\right], \tag{1.26}$$

where we should choose the sign of $(i\hat{\sigma})^{1/2}$ so that $W(x) \to 0$ as $x \to \infty$. This approximate analytical solution, evaluated at $x_{\rm out}$, together with its derivative, gives four (real) outer boundary conditions. The inner boundary condition generally takes the form $W'(x_{\rm in}) = aW(x_{\rm in})$, with a being a constant. Most of our results in §4 will be based on $a = 0$ (corresponding to zero torque at the inner edge of the disk), although we have experimented with different a's (see Figs. 1-2) and found that for $|a| \lesssim 1$ our results are unchanged to the extent that there are other parameters in the problem which have greater uncertainties. In numerically searching a mode, we make a guess for the eigenvalue $\hat{\sigma}$ and integrate eq. (1.21) from $x_{\rm out}$ to $x_{\rm in}$ using the Kaps-Rentrop scheme (Press et al. 1992). We use the globally convergent Newton method to find the correct value of $\hat{\sigma}$ that satisfies the boundary conditions.

1.4 Numerical Results and Discussion

In this section, we first study numerical properties of equation (1.21) and then discuss specific cases relevant to accreting NSs in LMXBs.

1.4.1 Mode Eigenfunction and Eigenvalue

For a given set of parameters $(\hat{\Omega}_{LT}, \hat{\Omega}_{\rm cl}, \hat{\Omega}_m, \hat{\Gamma}_m)$, equation (1.21) allows for many eigenmodes. Here we shall focus on the "fundamental" mode which is more concentrated near the inner edge of the disk and has larger $\hat{\sigma}_r$ (global precession

frequency) and smaller $\hat{\sigma}_i$ (damping rate) than any other "higher-order" modes (see Fig. 1).

If a mode were infinitely concentrated at the inner radius of the disk, one expects that the mode frequency $\hat{\sigma}_r$ is just the sum of the frequencies evaluated at the inner disk radius, i.e., $\hat{\sigma}_r = \hat{\Omega}_{LT} + \hat{\Omega}_{\rm cl} + \hat{\Omega}_m$. However, the calculated $\hat{\sigma}_r$ is always smaller than $\hat{\Omega}_{LT}+\hat{\Omega}_{\rm cl}+\hat{\Omega}_m$ because the mode is not infinitely concentrated but has a finite width.

Fig. 1 shows the tilt angle $\beta(x, t = 0) = |W(x)|$ associated with the modes for different sets of ($\hat{\Omega}_{LT}$,$\hat{\Gamma}_m$). We have set $\hat{\Omega}_{\rm cl} = \hat{\Omega}_m = 0$ (since they play a similar role as $\hat{\Omega}_{LT}$), $\mathcal{J}(x) = 1$, and $\nu_1/\nu_2 = 1$ in eq. (1.21) for simplicity[5]. We see that as $\hat{\Omega}_{LT}$ and $\hat{\Gamma}_m$ increase, the fundamental modes (solid lines) become more concentrated near the inner radius of the disk. This behavior can be understood heuristically: for a given $\Omega_{LT}(r)$, a larger $\hat{\Omega}_{LT}$ implies smaller viscosity, and thus the coupling between different disk radii is reduced.

Fig. 2 shows the mode frequency σ in units of $\Omega_{LT}(r_{\rm in})$, or $\sigma/\Omega_{LT}(r_{\rm in}) = \hat{\sigma}/\hat{\Omega}_{LT}$, as a function of $\hat{\Omega}_{LT}$ for different values of $\hat{\Gamma}_m$ [We again set $\hat{\Omega}_{\rm cl} = \hat{\Omega}_m = 0$, $\mathcal{J}(x) = 1$, and $\nu_1/\nu_2 = 1$]. We see that $\hat{\sigma}_r/\hat{\Omega}_{LT}$ always lies between 0.4 to 0.95 for the relevant ranges of $\hat{\Omega}_{LT}$ (10 to 10^4). The ratio $\hat{\sigma}_r/\hat{\Omega}_{LT}$ increases and approaches unity as $\hat{\Omega}_{LT}$ and $\hat{\Gamma}_m$ increase. This is consistent with the behavior of the mode eigenfunction (see Fig. 1) that a larger $\hat{\Omega}_{LT}$ or $\hat{\Gamma}_m$ makes the mode more concentrated near the inner disk edge.

[5]Note the results shown in Figs. 1-2 are not sensitive to $\mathcal{J}$ since $\mathcal{J}_{\rm in}$ has been absorbed in the definitions of dimensionless frequencies, eqs. (1.17)-(1.20). See also §4.3.

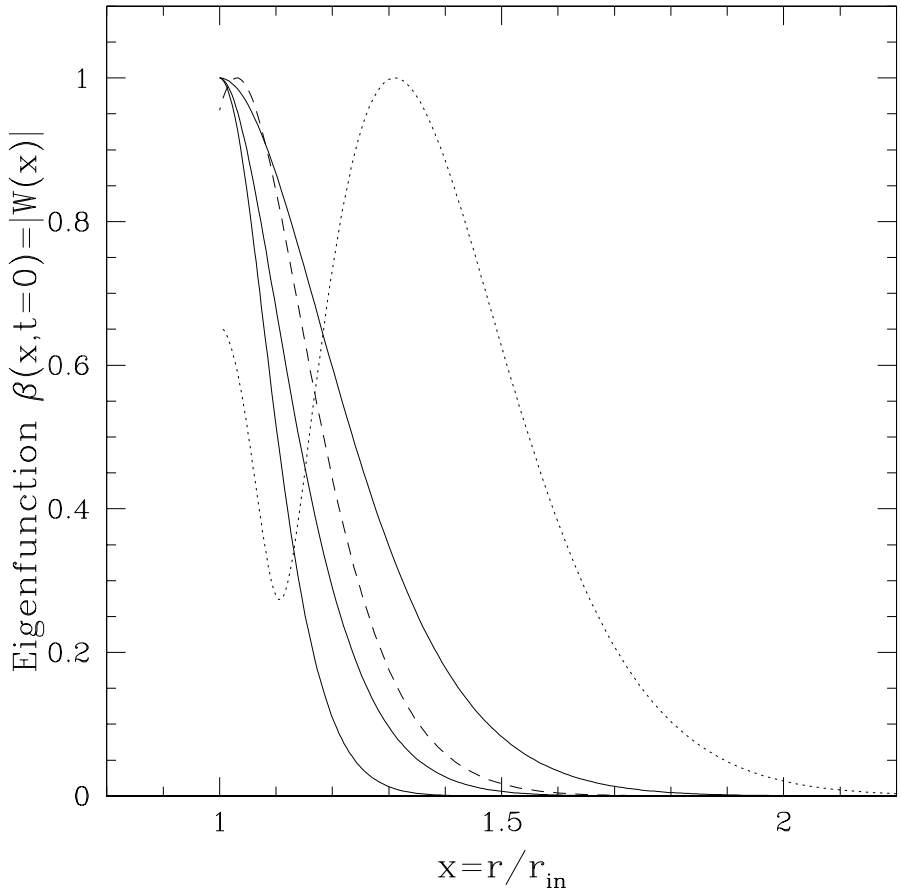

Figure 1.1: The disk tilt angle of the warping/precession modes for various parameter sets. The solid curves represent the fundamental modes for ($\hat{\Omega}_{LT}$, $\hat{\Gamma}_m$) =(1000, 0), (100, 100), and (100, 0) (with $\hat{\Omega}_{\rm cl} = \hat{\Omega}_m = 0$) from left to right, with the corresponding mode frequency $\hat{\sigma} = (\hat{\sigma}_r, \hat{\sigma}_i) = (860, 78)$, $(80, -46)$, and $(70, 15)$; the dotted curve represents a higher order mode for ($\hat{\Omega}_{LT}$, $\hat{\Gamma}_m$)=(100, 100), with $\hat{\sigma} = (\hat{\sigma}_r, \hat{\sigma}_i) = (41, 6.0)$; all these are calculated using the inner boundary condition (B.C.) $W' = 0$. The dashed curve shows the case for ($\hat{\Omega}_{LT}$, $\hat{\Gamma}_m$) =(100, 100), with the mode frequency $\hat{\sigma} = (65, -37)$, calculated using the inner B.C. $W' = W$. The eigenfunctions are normalized such that the maximum tilt angle is 1.

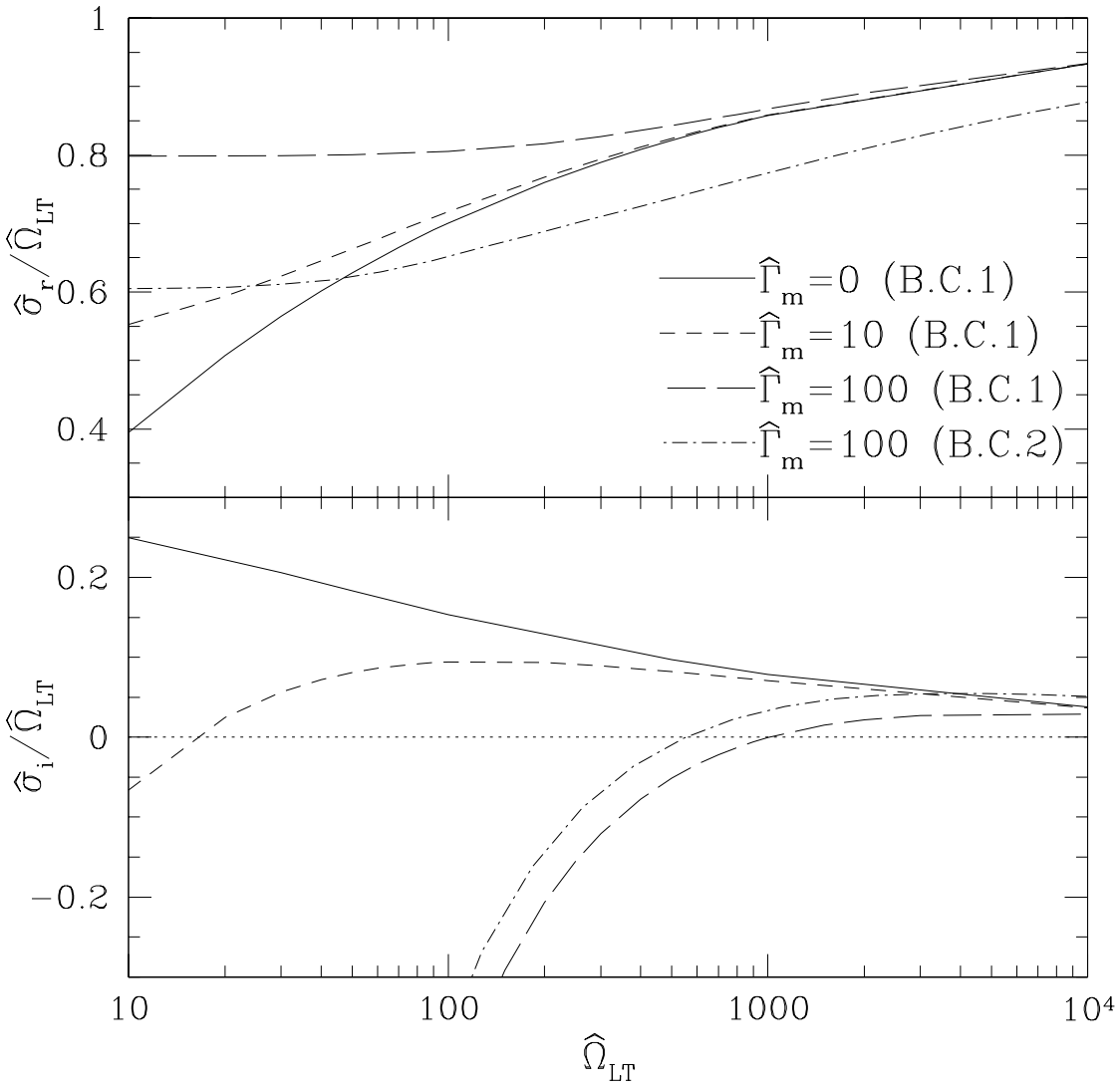

Figure 1.2: The upper panel shows the mode frequency $\hat{\sigma}_r$ in units of $\hat{\Omega}_{LT}$ as a function of $\hat{\Omega}_{LT}$ for different values of $\hat{\Gamma}_m$ (with $\hat{\Omega}_{\rm cl} = \hat{\Omega}_m = 0$). The lower panel shows the corresponding mode damping rate $\hat{\sigma}_i$ (in units of $\hat{\Omega}_{LT}$). Note that negative $\hat{\sigma}_i$ implies growing mode. The dot-dashed curves are obtained using the inner boundary condition $W' = W$, while all other curves are based on B.C. $W' = 0$.

1.4.2 Global Warping Instability Criterion

As discussed in §1, differential precession tends to be damped by the ν_2 viscosity. Fig. 2(b) shows that $\hat{\sigma}_i/\hat{\Omega}_{LT} = \sigma_i/\Omega_{LT}(r_{\rm in})$ is always positive (which implies damping) for $\hat{\Gamma}_m = 0$ and lies between 0.25 (for $\hat{\Omega}_{LT} = 10$) and 0.04 (for $\hat{\Omega}_{LT} = 10^4$), corresponding to Q value ($Q \approx \sigma_r/\sigma_i$) between 2 and 20 (the high-Q regime was also explored by Markovic & Lamb 1999 where a different disk model was adopted). We see that $\hat{\sigma}_i$ decreases as $\hat{\Gamma}_m$ increases, and becomes negative (implying mode growth) when the ratio $\hat{\Gamma}_m/\hat{\Omega}_{LT}$ is sufficiently large. The numerical values for $\hat{\sigma}_i$ can be approximated by

$$\hat{\sigma}_i = -a\hat{\Gamma}_m + b\hat{\Omega}_{LT}^{0.7}, \tag{1.27}$$

with $a \sim (0.5 - 1.0)$ and $b \sim 0.5$. For the mode to grow ($\hat{\sigma}_i < 0$) we require

$$\hat{\Gamma}_m \gtrsim \hat{\Omega}_{LT}^{0.7} \iff \text{Global Warping Instability.} \tag{1.28}$$

For $\dot{M}_{17} < \dot{M}_{17,\rm c}$ [see eq. (1.25)], so that $r_{\rm in} = r_m$, this condition becomes

$$0.7\,\zeta\,\mu_{26}^{-0.2}\cos^2\theta\,\alpha_{-1}^{0.7} I_{45}^{-0.7} M_{1.4}^{0.4}\dot{M}_{17}^{1.5}\left(\frac{\nu_s}{300\ {\rm Hz}}\right)^{-0.7}\left(\frac{\nu_1}{\nu_2}\right)^{0.3}\left(\frac{\eta}{0.5}\right)^{-3.85} \gtrsim 1. \tag{1.29}$$

For $\dot{M}_{17} > \dot{M}_{17,\rm c}$, so that $r_{\rm in} = r_{\rm ISCO}$, we require

$$0.2\,\zeta\,\mu_{26}^{2}\cos^2\theta\, I_{45}^{-0.7} M_{1.4}^{-4}\dot{M}_{17}^{0.4}\left(\frac{\nu_s}{300\ {\rm Hz}}\right)^{-0.7}\left(\frac{\nu_1}{\nu_2}\right)^{0.3} \gtrsim 1. \tag{1.30}$$

We see that for parameters that characterize accreting NSs in LMXBs the mode growth condition can be satisfied (see §4.3 for specific examples), although not always. In general, high (but not unreasonable) ζ (> a few) and $\dot{M}_{17}$ are preferred to obtain growing modes.

1.4.3 Dependence of Mode Frequency on $\dot{M}$

In §4.1 and §4.2, we have seen how $\hat{\Omega}_{LT}$ and $\hat{\Gamma}_m$ affect the dimensionless mode frequency $\hat{\sigma}$ $(= \hat{\sigma}_r + i\hat{\sigma}_i)$ while setting $\hat{\Omega}_{\rm cl} = \hat{\Omega}_m = 0$. We have found that $\hat{\sigma}_r$ is smaller than the naively expected value $\hat{\Omega}_{LT}$ for small $\hat{\Omega}_{LT}$ and $\hat{\Gamma}_m$, but becomes closer to $\hat{\Omega}_{LT}$ as $\hat{\Omega}_{LT}$ and $\hat{\Gamma}_m$ increase. We have also found that a sufficiently large $\hat{\Gamma}_m$ tends to make the mode unstable. In this subsection, we consider some specific examples to illustrate the dependence of the mode frequency σ on $\dot{M}$ and other parameters for NSs in LMXBs.

Fig. 3 shows the global precession frequency (i.e., $\sigma_r/2\pi$; the real part of the mode frequency in physical units) [6] as a function of the mass accretion rate for a fixed parameter set [Parameter Set A: $M_{1.4} = 1$, $R_6 = 1$, $n = 1$, $\nu_s = 300\,{\rm Hz}$, $\alpha_{-1} = 1$, $\zeta = 5$, $\sin^2\theta = 0.1$, $\nu_2/\nu_1 = 1$, $\mu_{26} = 2$, $\eta = 0.5$, $\xi = 0$, and $D(x)$ as given in eq. (1.3)], for three different cases: (i) only the Lense-Thirring precession is included, (ii) both the Lense-Thirring and classical precessions are included, and (iii) the magnetic precession and warping are included in addition to the Lense-Thirring and classical precessions. It also shows the fiducial precession frequency, $\nu_{\rm fid}$, which is the sum of the considered frequencies evaluated at the inner radius of the disk, i.e., $\nu_{\rm fid} \equiv (\Omega_{LT}(r_{\rm in}) + \Omega_{\rm cl}(r_{\rm in}) + \Omega_m(r_{\rm in}))/2\pi$.

The dependence of $\nu_{\rm fid}$ on $\dot{M}$ is understood in the following manner. From eqs. (1.13), (1.14), and (1.2), together with eqs. (1.22)–(1.24), we find $\Omega_{LT}(r_{\rm in}) \propto \dot{M}^{6/7}$, $\Omega_{\rm cl}(r_{\rm in}) \propto \dot{M}$, and $\Omega_m(r_{\rm in}) \propto \dot{M}^3$ when $r_{\rm in} = r_m$, and $\Omega_{LT}(r_{\rm in}) \propto \dot{M}^0$, $\Omega_{\rm cl}(r_{\rm in}) \propto \dot{M}^0$, and $\Omega_m(r_{\rm in}) \propto \dot{M}$ when $r_{\rm in} = r_{\rm ISCO}$. Thus we obtain, for the above

[6] In Figs. 3-6, we multiply the mode frequency by 4 to facilitate comparison with observations, since the QPOs appear to manifest as harmonics of the fundamental frequency (Stella & Vietri 1998; Psaltis et al. 1999; see also §5).

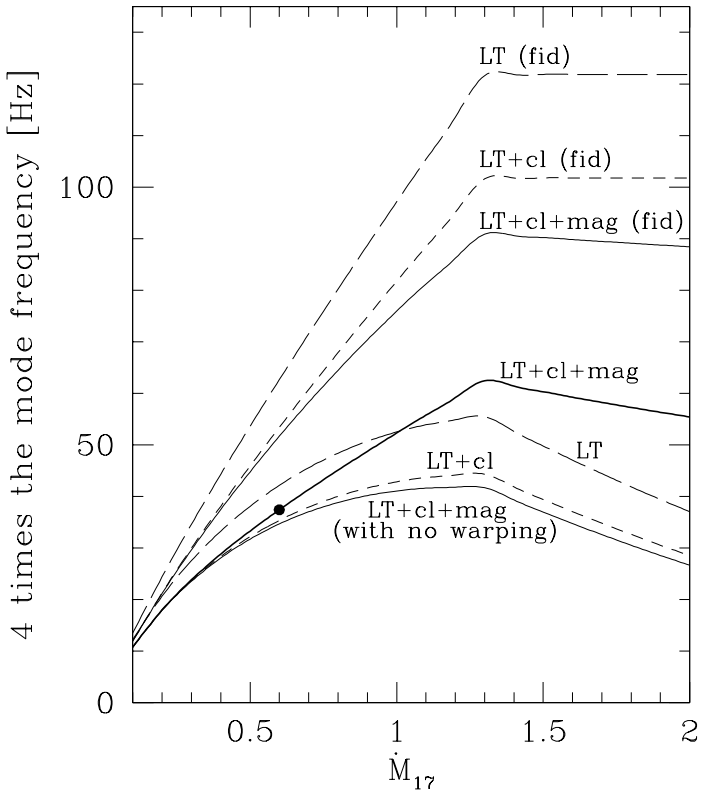

Figure 1.3: The global precession mode frequency $\sigma_r/2\pi$ as a function of the accretion rate $\dot{M}_{17}$. The frequencies are multiplied by 4 to facilitate comparison with observations (see the text for discussion). The upper three curves represent the fiducial frequency $\nu_{\rm fid}$ for three different cases described in the text: (i) only the Lense-Thirring precession is included (long dashed curve), (ii) both the Lense-Thirring and classical precessions are included (short dashed curve), and (iii) the magnetic precession and warping are included as well as the Lense-Thirring and classical precessions (solid curve). The thick solid curve is the corresponding global precession frequency $\sigma_r/2\pi$ for case (iii) (Note that the modes grow above $\dot{M}_{17} \simeq 0.6$; marked by a dot in the figure). The lower two dashed curves are the corresponding global precession frequency $\sigma_r/2\pi$ for case (i) and (ii). The lower light solid curve shows $\sigma_r/2\pi$ for case (iii) obtained with the magnetic warping torque artificially turned off.

three different cases:

$$\text{(i) } \nu_{\rm fid} \propto \mathcal{O}(\dot{M}^{6/7}) \ \ (\dot{M}_{17} < \dot{M}_{17,\rm c}), \tag{1.31}$$

$$\nu_{\rm fid} \propto \mathcal{O}(\dot{M}^{0}) \ \ (\dot{M}_{17} > \dot{M}_{17,\rm c}). \tag{1.32}$$

$$\text{(ii) } \nu_{\rm fid} \propto \mathcal{O}(\dot{M}^{6/7}) - \mathcal{O}(\dot{M}) \ \ (\dot{M}_{17} < \dot{M}_{17,\rm c}), \tag{1.33}$$

$$\nu_{\rm fid} \propto \mathcal{O}(\dot{M}^{0}) \ \ (\dot{M}_{17} > \dot{M}_{17,\rm c}). \tag{1.34}$$

$$\text{(iii) } \nu_{\rm fid} \propto \mathcal{O}(\dot{M}^{6/7}) - \mathcal{O}(\dot{M}) - \mathcal{O}(\dot{M}^{3}) \ \ (\dot{M}_{17} < \dot{M}_{17,\rm c}), \tag{1.35}$$

$$\nu_{\rm fid} \propto \mathcal{O}(\dot{M}^{0}) - \mathcal{O}(\dot{M}) \ \ (\dot{M}_{17} > \dot{M}_{17,\rm c}). \tag{1.36}$$

For Parameter Set A adopted in Fig. 3, the transition from $r_{\rm in} = r_m$ to $r_{\rm in} = r_{\rm ISCO}$ occurs at $\dot{M}_{17,\rm c} = 1.3$ [see eq. (1.25)].

We see from Fig. 3 that the behavior of the mode frequency $\sigma_r/2\pi$ as a function of $\dot{M}$ is different from that of $\nu_{\rm fid}$ for all three cases (i)-(iii). For case (i) and (ii), $\sigma_r/2\pi$ is as small as $\sim 30\%$ of $\nu_{\rm fid}$ for high $\dot{M}$ ($\dot{M}_{17} \sim 1.5 - 2.0$) and the dependence of $\sigma_r/2\pi$ on $\dot{M}$ is very different from that of $\nu_{\rm fid}$. This is understood from our discussion in §4.1: The viscosity rate increases (and $\hat{\Omega}_{LT} + \hat{\Omega}_{\rm cl}$ decreases) as $\dot{M}$ increases [see eq. (1.16)]; this tends to spread the mode by coupling (through viscous stress) disk rings at different radii, thereby reducing $\sigma_r/2\pi$ relative to $\nu_{\rm fid}$. The increasing importance of viscosity for high mass accretion rate is also expected for case (iii), where additional magnetic effects are included. However, we see from Fig. 3 that $\sigma_r/2\pi$ becomes closer to $\nu_{\rm fid}$ when the magnetic warping torque (Γ_m) is included. This is understood from our finding in §4.1 (see Figs. 1–2) that the presence of Γ_m makes the mode more concentrated near the disk inner radius.

Fig. 4 shows the mode frequency $\sigma_r/2\pi$ as a function of $\dot{M}$ for three sets of parameters, Set A, B, and C, where (μ_{26}, $\sin^2\theta$) = (2, 0.1), (2, 0.5) and (4, 0.1), respectively, while the other parameters are fixed to the standard values: $M_{1.4} = 1$,

$R_6 = 1$, $n = 1$, $\nu_s = 300\,\mathrm{Hz}$, $\alpha_{-1} = 1$, $\zeta = 5$, $\nu_2/\nu_1 = 1$, $\eta = 0.5$, $\xi = 0$. All of the Lense-Thirring, classical precessions and magnetic precession and warping are included [case (iii)]. For Parameter Set A and B, the inner radius of the disk reaches $r_{\rm ISCO}$ at the same $\dot{M}_{17,\,\rm c} = 1.3$ [see eq. (1.25)]. For Parameter Set A, $|\Omega_m(r_{\rm in})|$ is much smaller than $\Omega_{LT}(r_{\rm in}) + \Omega_{\rm cl}(r_{\rm in})$ for small $\dot{M}_{17}$ although it becomes more important for large $\dot{M}_{17}$; thus at $\dot{M}_{17} = \dot{M}_{17,\,\rm c}$, $\sigma_r/2\pi$ suddenly changes from an increasing function of $\dot{M}$ as given by eq. (1.35) (with small second and third terms) to a linearly decreasing function of $\dot{M}$ as given by eq. (1.36). For Parameter Set B, $|\Omega_m(r_{\rm in})| \propto \sin^2\theta$ is 5 times larger than that in Parameter Set A and is important even for small $\dot{M}_{17} < \dot{M}_{17,\,\rm c}$; thus $\sigma_r/2\pi$ shows a gradual turnover feature according to eq. (1.35) and becomes a linearly decreasing function of $\dot{M}$ [see eq. (1.36)] above $\dot{M}_{17,\,\rm c}$. For Parameter Set C, the inner radius of the disk is always given by r_m for the relevant $\dot{M}$ (since $\dot{M}_{17,\,\rm c} = 5.2$). As $|\Omega_{\rm cl}(r_{\rm in})|$ and $|\Omega_m(r_{\rm in})|$ are much smaller than $\Omega_{LT}(r_{\rm in})$, $\sigma_r/2\pi$ is a monotonically increasing function as given by eq. (1.35) (with small second and third terms).

Fig. 5 illustrates the dependence of the mode frequency $\sigma_r/2\pi$ on the polytropic index n and the dimensionless parameter ξ [defined in eq. (1.6)] (other parameters are the same as in Parameter Set A adopted in Fig. 4). Most nuclear equations of state have effective polytropic index between 0.5 and 1. We see that $\sigma_r/2\pi$ is larger for a stiffer equation of state (smaller n) and a larger ξ, although the dependences are not as strong as on other parameters (cf, Fig. 4).

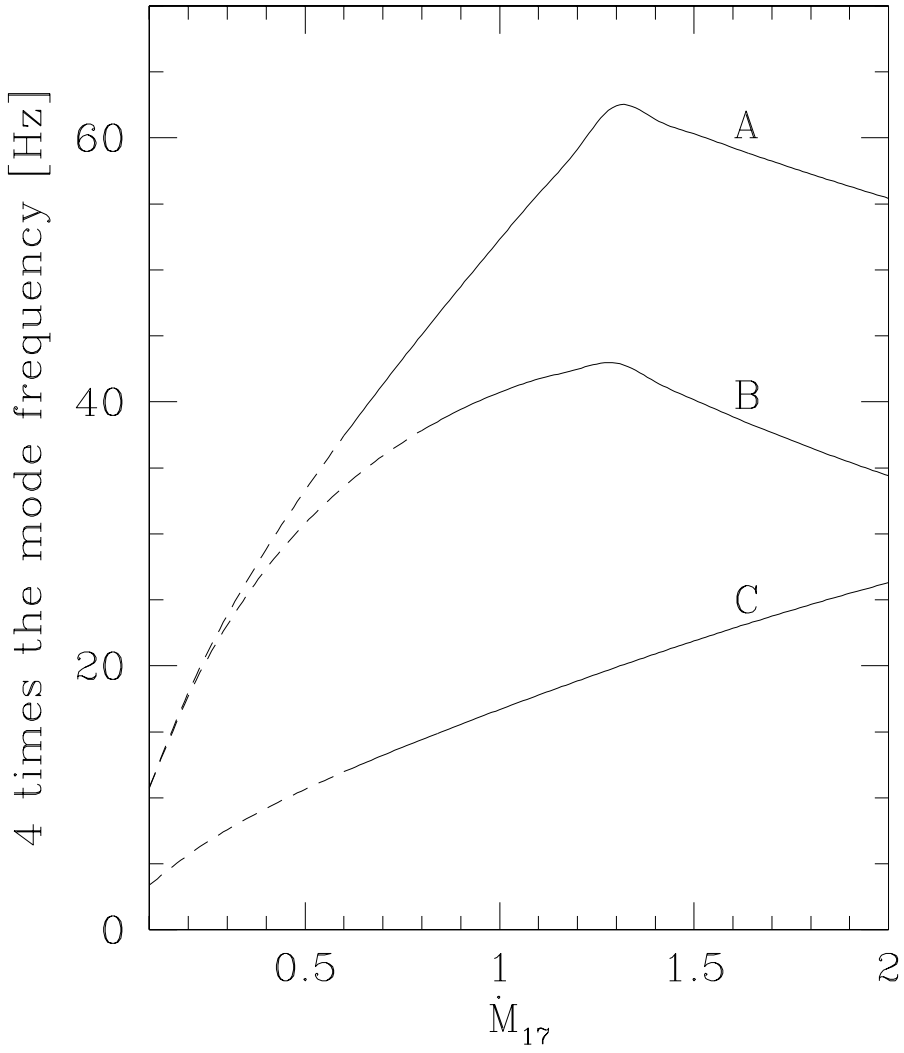

Figure 1.4: Correlation between the mode frequency $\sigma_r/2\pi$ and the accretion rate $\dot{M}_{17}$ for Parameter Sets A, B, and C: (μ_{26}, $\sin^2\theta$) = (2, 0.1), (2, 0.5), & (4, 0.1), respectively (see the text for the values of other fixed parameters) when all of the Lense Thirring, classical, and magnetic precessions and magnetic warping are taken into account. The solid portion of the curve corresponds to growing mode and the dashed portion corresponds to damping mode. To compare with LFQPOs observed in LMXBs, we multiply $\sigma_r/2\pi$ by 4.

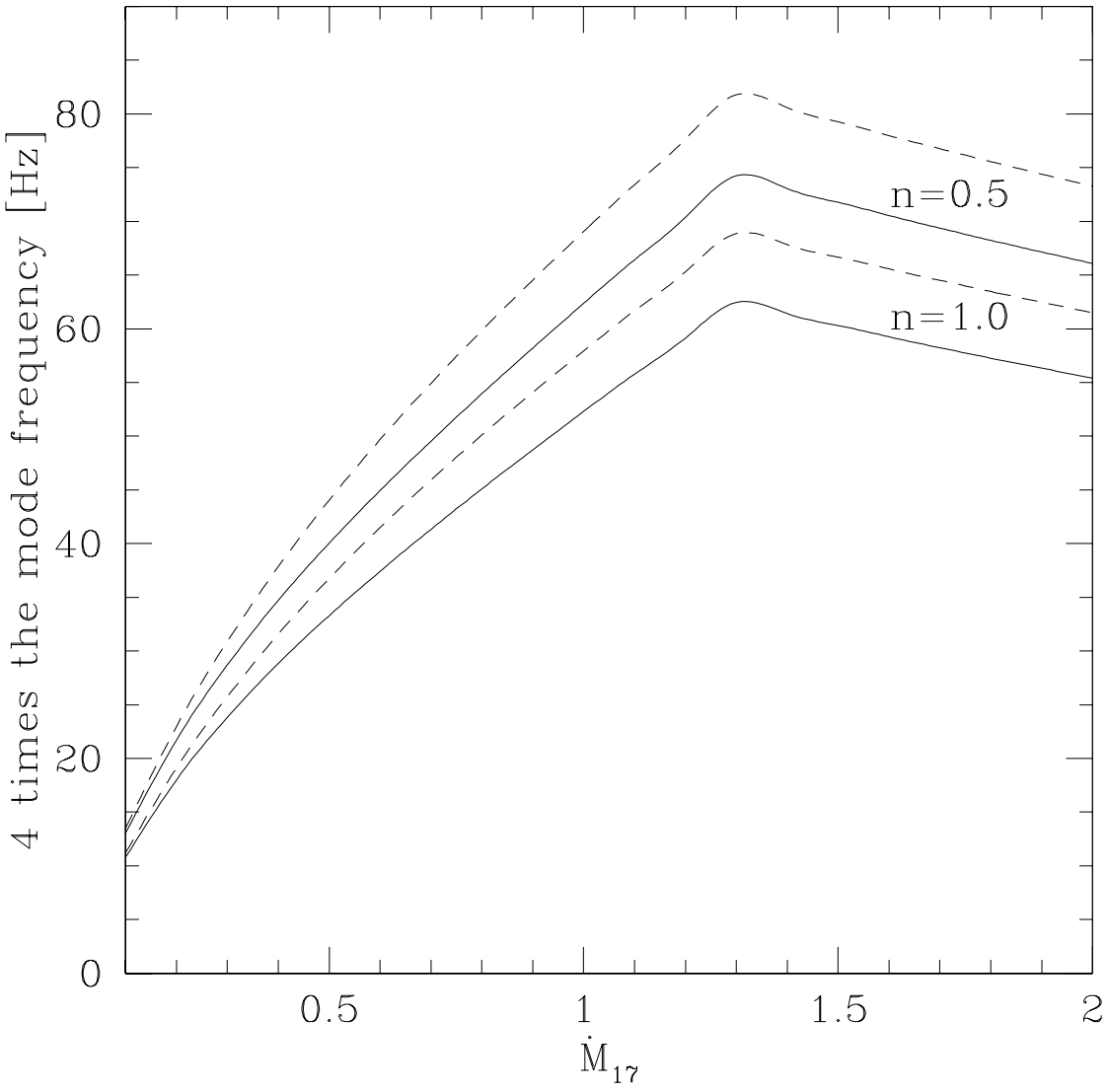

Figure 1.5: The mode frequency $\sigma_r/2\pi$ (multiplied by 4) as a function of $\dot{M}_{17}$ for polytrope index $n = 0.5$ (upper two curves) and 1 (lower two curves), and for $\xi = 0$ (solid curves) and $\xi = 0.5$ (dashed curves) [see eq. (1.6)]. Other parameters are the same as in Parameter Set A adopted in Fig. 4.

1.4.4 Comparison with the Observed Behaviors of LFQPOs

The behavior of σ_r as a function of $\dot{M}$ (see Figs. 3–5) is similar to the features observed for the LFQPOs in LMXBs (see van der Klis 1995, 2000). While for some systems, the LFQPO frequencies increase as the X-ray flux increases, for other systems, a non-monotonic (even opposite) correlation between the QPO frequency and $\dot{M}$ has been observed. As an example, for the Z source GX 17+2, using the position of the source on the X-ray color-color diagram as an indicator of $\dot{M}$, Wijnands et al. (1996) found that the HBO frequency increases with $\dot{M}$ for small $\dot{M}$ but decreases with further increase of $\dot{M}$. In the simple model where the LFQPO is identified with the precession frequency at the disk inner radius $r_{\rm in}$ (Stella & Vietri 1998; see §1), the non-monotonic behavior is difficult to explain, even when the classical (retrograde) precession is included [7] (see Psaltis et al. 1999; Morsink & Stella 1999). However, we see from Fig. 4 that when we consider global disk modes and include the magnetic effects, a variety of $\sigma_r - \dot{M}$ behaviors are possible. In our model the turnover of the $\sigma_r - \dot{M}$ correlation occurs for two reasons: (1) the magnetically driven retrograde precession $\Omega_m \propto -1/r^7$ becomes more important with increasing $\dot{M}$ [see eqs. (1.35) & (1.36)]; (2) the viscous stress becomes more important as $\dot{M}$ increases, and makes the mode less concentrated around $r_{\rm in}$; thus σ_r is more reduced from $\nu_{\rm fid}$ with increasing $\dot{M}$. We note that even when magnetic effects are not included [case (i) & (ii)], the "turnover" feature is obtained due to mechanism (2) as explained above (see Fig. 3). However, these modes are highly damped by viscosity. Only the magnetic warping torque can make the mode grow

[7] This is because $\Omega_{LT} \propto r^{-3}$ and $\Omega_{\rm cl} \propto -r^{-7/2}$ have a similar r-dependence; see eqs. (1.13) and (1.14).

(see Fig. 4).

A related puzzle concerns the correlation between the LFQPO frequency and the higher kilohertz QPO frequency (e.g., Stella & Vietri 1998; Ford & van der Klis 1998; Psaltis et al. 1999; see §1). It was found that for several sources the positive correlation flattens (and even turns over) for large kHz QPO frequencies (and large $\dot{M}$) (see Homan et al. 2001 for a clear case of such turnover in GX 17+2). Again, this feature is difficult to explain with the simple picture of Lense-Thirring and classical precessions at $r_{\rm in}$, but can be accounted for qualitatively by our global disk oscillation model with magnetic effects (see Fig. 6; note that we have not tried to vary the model parameters to "fit" the observations). More quantitative comparison between our models and the data require a better understanding of the origin of kHz QPOs (e.g., it is not certain whether the kHz QPO frequency is the Keplerian frequency at $r_{\rm in}$; see §5 for other uncertainties expected in real systems).

1.5 Concluding Remarks

We have shown in this chapter that the inner region of the disk around a weakly magnetized ($\sim 10^8$ G) NS is warped due to magnetic field – disk interactions (see Lai 1999) and therefore must precess under the combined effects of relativistic frame dragging, classical precession (due to the oblateness of the NS) and magnetic torques. We have found growing warping/precession modes of the inner disk and shown that these modes have properties that resemble the 10–60 Hz low-frequency QPOs observed in LMXBs (see §4).

Although our treatments of disk warping/precession go beyond many previous models of QPOs (these models typically identify a QPO frequency as the charac-

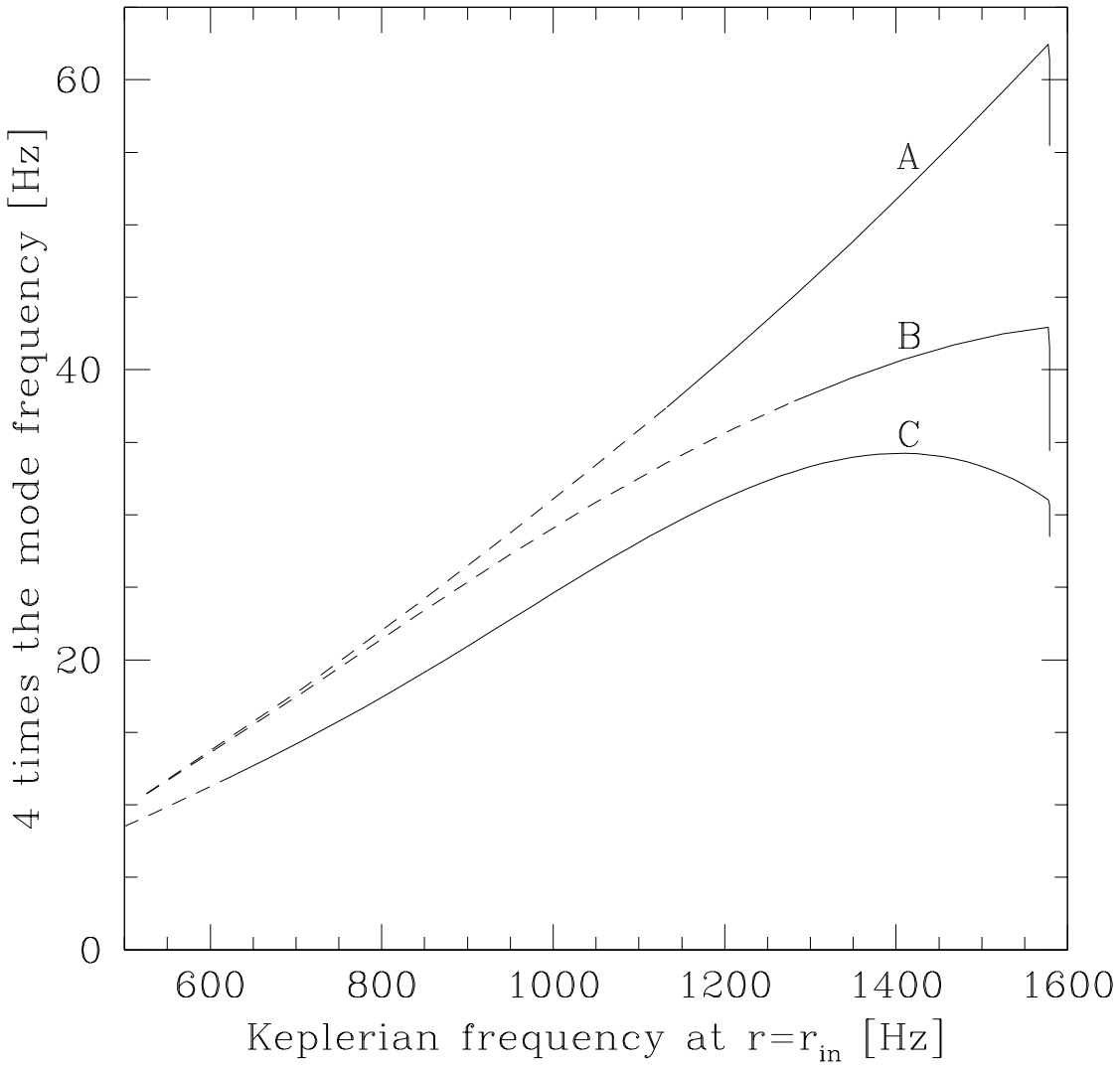

Figure 1.6: Correlation between the mode frequency $\sigma_r/2\pi$ (multiplied by 4) and the Keplerian frequency at the inner radius of the disk for Parameter Sets A, B, and C as in Fig. 4. The solid portion of the curve corresponds to growing mode and the dashed portion corresponds to damping mode.

teristic frequency of a test mass at certain special radius in the disk; see van der Klis 2000 for a review), they still contain important idealizations. For example, we have assumed the stellar field to be dipolar when considering the magnetic field – disk interactions. This is unlikely to be correct for LMXBs since the disk (with $r_{\rm in}$ only a few stellar radii) can produce significant change in the global field topology even when the intrinsic stellar field is dipolar (see Lai, Lovelace & Wasserman 1999). Observationally, the absence of persistent millisecond pulsation in all known LMXBs but SAX J1808.4–3658 (Wijnands & van der Klis 1998) and the frequency drift of burst oscillations (e.g., Strohmayer 2000; see also Cumming et al. 2001) may imply that the NS does not possess a well-defined dipole field, although a more complex field is possible. Also, we have only studied the linear behavior of the warping/precession modes in our study. Because of these idealizations and the uncertainties in observations (e.g., it is difficult to determine $\dot{M}$ precisely from observations), more quantitative comparison between the observational data and our theory is premature at present. Nevertheless, the results presented here demonstrate that magnetically driven warping and precession can give rise to a variety of new possibilities for the dynamical behaviors of inner accretion disks around magnetic NSs.

Concerning the observed properties of QPOs, many issues remain unanswered in our work (and in other related QPO studies): e.g, How does the mode manifest itself as a variation in the X-ray flux? How is the observed QPO amplitude (as large as 15%) produced? One possibility is that the LFQPO is caused by occultation of the central NS by the warped, precessing inner disk. Another issue is that for the observed NS spin rates (based on observations of burst oscillations) and reasonable moment of inertia of the neutron star, the data require that the observed LFQPO

corresponds to 2 or 4 times the precession mode frequency (see §1; the fact that the global mode frequency is smaller than the precession frequency at $r_{\rm in}$ exacerbates the problem); while this may be possible, more theoretical study on this issue is needed. Finally, there is an indication (but by no means proven) that some black hole systems display low-frequency QPOs which resemble their counterparts in NS systems (Psaltis, Belloni & van der Klis 1999). Clearly, the magnetic warping and precession torques discussed in this chapter are irrelevant to black hole systems[8]. We note that the phenomenology of black hole QPOs is much less developed, and that many of the $\dot{M}$-dependent behaviors of LFQPOs observed in NS systems are absent in the black hole systems (see Remillard 2001).

[8]Note that even without the magnetic torques and the classical precession, the mode frequency is reduced relative to the Lense-Thirring frequency at $r_{\rm in}$ as $\dot{M}$ increases (see Fig. 3); this result applies equally to the black hole systems except that the mode is damped in the absence of other excitation mechanisms.

Chapter 2

Magnetically Driven Precession of Warped Disks and Milli-Hertz QPOs in Accreting X-Ray Pulsars

2.1 Introduction

Disk accretion onto a magnetic star occurs in a variety of astrophysical contexts, including accreting neutron stars, white dwarfs and pre-main-sequence stars (e.g., Frank et al. 1992). The basic picture of disk–magnetosphere interaction is well-known: at large radii the disk is unaffected by the stellar magnetic field; a somewhat sudden transition occurs when the stellar field disrupts the disk at the magnetospheric boundary (where the magnetic and plasma stresses balance), and channels the plasma onto the polar caps of the star. A large number of theoretical papers have been written on the subject of the interaction between accretion disks and magnetized stars (e.g., Pringle & Rees 1972; Ghosh & Lamb 1979, 1992; Aly 1980; Anzer & Börner 1980, 1983; Lipunov et al. 1981; Wang 1987, 1995; Aly & Kuijpers 1990; Spruit & Taam 1993; Shu et al. 1994; van Ballegooijen 1994; Lovelace et al. 1995,1998; Li, Wickramasinge & Rüdiger 1996; Campbell 1997; Lai 1998; Terquem & Papaloizou 2000), but numerical study of this problem is still in its infancy (e.g., Hayashi et al. 1996; Miller & Stone 1997; Goodson et al. 1997; Fendt & Elstner 2000). Outstanding issues remain, including the efficiency of field dissipation in/outside the disk, whether the disk excludes the stellar field by diamagnetic currents or the field can penetrate a large fraction of the disk, whether the

threaded field remains closed (connecting the star and the disk) or becomes open by differential shearing, and whether/how magnetically driven wind is launched from the disk or the magnetosphere/corotation boundary.

Many previous theoretical papers have, for simplicity, adopted the idealized geometry in which the magnetic axis, the spin axis and the disk angular momentum are aligned. However, in Lai (1999), it was shown that under quite general conditions, the stellar magnetic field can induce warping in the inner disk and make the disk precess around the spin axis (see §2). Such magnetically driven warping and precession open up new possibilities for the dynamical behaviors of disk accretion onto magnetic stars. In Shirakawa & Lai (2001) we have studied these effects in weakly magnetized accreting neutron stars and showed that the magnetic warping/precession effects may explain several observed features of low-frequency quasi-periodic oscillations in low-mass X-ray binaries.

In this chapter we study global, magnetically driven warping/precession modes of inner disks of highly magnetized ($B \sim 10^{12}$ G) neutron stars (NSs), as in accreting X-ray pulsars (§2 and §3). Such study is the first step toward understanding the observational manifestations of the magnetic warping/precession effects. We are motivated by the observations of the milli-Hertz quasi-periodic oscillations (QPOs) in a number of X-ray pulsars (see Table 1 in §4 and references therein). Of particular interest is the recent detection of the 1 mHz optical/UV oscillations in 4U 1626-67 (Chakrabarty et al. 2001). In §4, we use the results of §3 and suggest that magnetically driven disk warping and precession naturally explain this and some other mHz variabilities observed in X-ray pulsars.

This chapter is based on the published paper by Shirakawa & Lai 2002 [Shirakawa, A. & Lai D. 2002, The Astrophysical Journal, 565, 1134; ©2002. The

 It is reprinted here with minor changes, based on rights retained by the author.

2.2 Magnetically Driven Warping/Precession and its Global Modes

The inner region of the accretion disk onto a rotating magnetized central star is subjected to magnetic torques that induce warping and precession of the disk (Lai 1999). These magnetic torques result from the interactions between the accretion disk and the stellar magnetic field. Depending on how the disk responds to the stellar field, two different kinds of torque arise: (i) If the vertical stellar magnetic field B_z penetrates the disk, it gets twisted by the disk rotation to produce an azimuthal field $\Delta B_\phi = \mp\zeta B_z$ that has different signs above and below the disk (ζ is the azimuthal pitch of the field line and depends on the dissipation in the disk), and a radial surface current K_r results. The interaction between K_r and the stellar B_ϕ gives rise to a vertical force. While the mean force (averaging over the azimuthal direction) is zero, the uneven distribution of the force induces a net *warping torque* which tends to misalign the angular momentum of the disk with the stellar spin axis. (ii) If the disk does not allow the vertical stellar field (e.g., the rapidly varying component of B_z due to stellar rotation) to penetrate, an azimuthal screening current K_ϕ will be induced on the disk. This K_ϕ interacts with the radial magnetic field B_r and produces a vertical force. The resulting *precessional torque* tends to drive the disk into retrograde precession around the stellar spin axis.

In general, both the magnetic warping torque and the precessional torque are present. For small disk tilt angle β (the angle between the disk normal and the

spin axis), the precession angular frequency and warping rate at radius r are given by (see Lai 1999)[1]

$$\Omega_p(r) = \frac{\mu^2}{\pi^2 r^7 \Omega(r)\Sigma(r)D(r)} F(\theta), \tag{2.1}$$

$$\Gamma_w(r) = \frac{\zeta\mu^2}{4\pi r^7 \Omega(r)\Sigma(r)} \cos^2\theta, \tag{2.2}$$

where μ is the stellar magnetic dipole moment, θ is the angle between the magnetic dipole axis and the spin axis, $\Omega(r)$ is the orbital angular frequency, and $\Sigma(r)$ is the surface density of the disk. The dimensionless function $D(r)$ is given by

$$D(r) = \max\left(\sqrt{r^2/r_{\rm in}^2 - 1}, \sqrt{2H(r)/r_{\rm in}}\right), \tag{2.3}$$

where $H(r)$ is the half-thickness and $r_{\rm in}$ is the inner radius of the disk. The function $F(\theta)$ depends on the dielectric property of the disk. We can write

$$F(\theta) = 2f\cos^2\theta - \sin^2\theta, \tag{2.4}$$

so that $F(\theta) = -\sin^2\theta$ if only the spin-variable vertical field is screened out by the disk ($f = 0$), and $F(\theta) = 3\cos^2\theta - 1$ if all vertical field is screened out ($f = 1$). In reality, f lies between 0 and 1. For concreteness, we shall set $F(\theta) = -\sin^2\theta$ in the following.

For accretion-powered X-ray pulsars, the inner disk radius $r_{\rm in}$ is given by the magnetosphere radius r_m:

$$r_{\rm in} \equiv \eta\left(\frac{\mu^4}{GM\dot{M}^2}\right)^{1/7} = (3.4\times10^8\ {\rm cm})\,\eta\,\mu_{30}^{4/7} M_{1.4}^{-1/7}\dot{M}_{17}^{-2/7}, \tag{2.5}$$

where $M = (1.4M_\odot)M_{1.4}$ is the neutron star mass, $\dot{M} = (10^{17}\,{\rm g\,s^{-1}})\dot{M}_{17}$ is the mass accretion rate, $\mu_{30} = \mu/(10^{30}\ {\rm G\,cm^3})$, and $\eta \sim 0.5 - 1$. For typical parameters, the

[1]Note that the stellar spin frequency Ω_s does not appear in eqs. (1) & (2) since the variation of the field geometry due to the spin has been averaged out; this is justified because $\Omega_s \gg |\Omega_p|,\ |\Gamma_w|$.

precession frequency is

$$\frac{\Omega_p(r)}{2\pi} = -(11.8\ \mathrm{mHz})\,\mu_{30}^2 M_{1.4}^{-1/2} r_8^{-11/2} \times \left[\frac{\Sigma(r)}{10^4\ \mathrm{g\,cm^{-2}}}\right]^{-1} \left[\frac{D(r)}{0.1}\right]^{-1} \sin^2\theta, \quad (2.6)$$

where we have used $\Omega(r) = (GM/r^3)^{1/2}$, and $r_8 = r/(10^8\ \mathrm{cm})$. The warping rate $\Gamma_w(r)$ is of the same order of magnitude as $\Omega_p(r)$.

Since the precession rate $\Omega_p(r)$ depends strongly on r, coupling between different rings is needed to produce a global coherent precession. The coupling can be achieved either by viscous stress or through bending waves (e.g., Papaloizou& Pringle 1983; Papaloizou & Terquem 1995; Larwood et al. 1996; Terquem 1998). In the viscosity dominated regime (i.e., the dimensionless viscosity parameter α greater than H/r), the dynamics of the warps can be studied using the formalism of Papaloizou & Pringle (1983) (see also Pringle 1992; Ogilvie 1999; Ogilvie & Dubus 2001). We model the disk as a collection of rings which interact with each other via viscous stresses. Each ring at radius r has the unit normal vector $\hat{\mathbf{l}}(r,t)$. In the Cartesian coordinates, with the z-axis along the neutron star spin, we write $\hat{\mathbf{l}} = (\sin\beta\cos\gamma, \sin\beta\sin\gamma, \cos\beta)$, with $\beta(r,t)$ the tilt angle and $\gamma(r,t)$ the twist angle. For $\beta \ll 1$, the dynamical warp equation for $\hat{\mathbf{l}}$ (Lai 1999; see Papaloizou & Pringle 1983; Pringle 1992) reduces to an equation for $W(r,t) \equiv \beta(r,t)e^{i\gamma(r,t)}$:

$$\frac{\partial W}{\partial t} - \left[\frac{3\nu_2}{4r}\left(1 + \frac{2r\mathcal{J}'}{3\mathcal{J}}\right) + \frac{3\nu_1}{2r}(\mathcal{J}^{-1} - 1)\right]\frac{\partial W}{\partial r} = \frac{1}{2}\nu_2\frac{\partial^2 W}{\partial r^2} + i\Omega_p W + \Gamma_w W, \quad (2.7)$$

where $\mathcal{J}' = d\mathcal{J}/dr$, ν_1 is the usual viscosity , and ν_2 is the viscosity which tends to reduce the disk tilt. We assume that the ratio of ν_2 to ν_1 is constant. In deriving eq. (2.7), we have used the relations for the radial velocity and surface density:

$v_r = -3\nu_1\mathcal{J}^{-1}/2r$ and $\Sigma = \dot{M}\mathcal{J}/3\pi\nu_1$. The values and functional forms of ν_1, ν_2, Ω_p, Γ_w [see eqs. (2.1) & (2.2)], and the dimensionless function $\mathcal{J}(r)$ [see eq. (2.16) below] depend on disk models.

2.2.1 Power-law Disk Models

To gain insight on the properties of the global warping-precessional modes, we consider power-law disk models, with $\Sigma(r) \propto r^\mu$. We also assume that $D(r)$= constant, $\mathcal{J}(r) = 1$, $\nu_2/\nu_1 = 1$, and $\Omega(r) \propto r^{-3/2}$ as in the Keplerian flow. Then, from eqs. (2.1) & (2.2), we have

$$\Omega_p(r) = \Omega_p(r_{\rm in}) \left(\frac{r}{r_{\rm in}}\right)^{-\mu-11/2}, \tag{2.8}$$

$$\Gamma_w(r) = \Gamma_w(r_{\rm in}) \left(\frac{r}{r_{\rm in}}\right)^{-\mu-11/2}. \tag{2.9}$$

Using the relation $\Sigma = \dot{M}\mathcal{J}/3\pi\nu_1$, the viscosity rate $\tau_{\rm visc}^{-1}$ can be written as

$$\tau_{\rm visc}^{-1}(r) \equiv \frac{\nu_2(r)}{r^2} = \tau_{\rm visc}^{-1}(r_{\rm in}) \left(\frac{r}{r_{\rm in}}\right)^{-\mu-2}. \tag{2.10}$$

We look for a solution of the form $W(r,t) = e^{i\sigma t}W(r)$ with the complex mode frequency σ $(= \sigma_r + i\sigma_i)$. It is convenient to define dimensionless quantities by

$$\hat{\sigma} \equiv \sigma(r_{\rm in})\tau_{\rm visc}(r_{\rm in}), \quad \hat{\Omega}_p \equiv \Omega_p(r_{\rm in})\tau_{\rm visc}(r_{\rm in}),$$
$$\hat{\Gamma}_w \equiv \Gamma_w(r_{\rm in})\tau_{\rm visc}(r_{\rm in}). \tag{2.11}$$

Equation (2.7) then reduces to the dimentionless form:

$$i\hat{\sigma}W - \frac{3}{4x^{\mu+1}}\frac{dW}{dx} = \frac{1}{2x^\mu}\frac{d^2W}{dx^2} + i\frac{\hat{\Omega}_p}{x^{\mu+11/2}}W + \frac{\hat{\Gamma}_w}{x^{\mu+11/2}}W, \tag{2.12}$$

where $x \equiv r/r_{\rm in}$.

It is clear from eq. (2.12) that, for a given μ, the mode frequency $\hat{\sigma}$ depends only on two dimensionless parameters $\hat{\Omega}_p$ and $\hat{\Gamma}_w$. To solve eq. (2.12) for the complex

eigenfunction $W(x)$ and eigenvalue $\hat{\sigma}$, six real boundary conditions are needed. In our calculation, the disk extends from $x_{\rm in} = 1$ to $x_{\rm out} = 50$. For large x and large $|\hat{\sigma}|$, equation (2.12) can be solved analytically, giving

$$W(x) \propto \exp\left[\frac{2\sqrt{2}}{\mu+2}\,(i\hat{\sigma})^{1/2}x^{\mu/2+1}\right], \tag{2.13}$$

where the sign of $(i\hat{\sigma})^{1/2}$ should be chosen so that $W(x) \to 0$ as $x \to \infty$. This approximate analytical solution, evaluated at $x_{\rm out}$, together with its derivative, gives four (real) outer boundary conditions. The inner boundary condition generally takes the form $W'(x_{\rm in}) = aW(x_{\rm in})$, with a being a constant. Most of our results in §3 are based on $a = 0$ (corresponding to zero torque at the inner edge of the disk), although we have experimented with different a's and found that for $|a| \lesssim 1$ similar results are obtained (see Shirakawa & Lai 2001). In numerically searching a mode, we make a guess for the eigenvalue $\hat{\sigma}$ and integrate eq. (2.12) from $x_{\rm out}$ to $x_{\rm in}$. Since $W(x)$ changes very rapidly from $x_{\rm out}$ to $x_{\rm in}$, we rewrite eq. (2.12) in terms of a new function w defined as $W = e^w$ and use that equation for integration. We find the correct value of $\hat{\sigma}$ that satisfies the boundary conditions using the globally convergent Newton method (Press et al. 1992).

2.2.2 Middle-Region Solution of the α-Disk

Here we consider the "middle-region" (gas-pressure -and scattering-dominated) solution of the α-disk (Shakra & Sunyaev 1973; Novikov & Thorne 1973) which is relevant to the inner part of the disk in accretion-powered X-ray pulsars. In this model,

$$\Sigma = (7.5\times10^3\,{\rm g\,cm^{-2}})\alpha_{-1}^{-4/5}M_{1.4}^{1/5}\dot{M}_{17}^{3/5}r_8^{-3/5}\mathcal{J}^{3/5}, \tag{2.14}$$

$$H = (1.0\times10^6\,{\rm cm})\alpha_{-1}^{-1/10}M_{1.4}^{-7/20}\dot{M}_{17}^{1/5}r_8^{21/20}\mathcal{J}^{1/5}, \tag{2.15}$$

where $\alpha = (0.1)\alpha_{-1}$ is the α-viscosity parameter. The dimensionless function $\mathcal{J}(r)$ is given by [2]

$$\mathcal{J}(r) = 1 - \xi\sqrt{\frac{r_{\rm in}}{r}}, \tag{2.16}$$

where ξ is a dimensionless parameter with $0 \leq \xi < 1$ ($\xi = 0$ corresponds to to zero net angular momentum transfer across the inner disk, i.e., when the star is in spin equilibrium). Substituting equation (2.14) into equations (2.1) and (2.2), and using $\Omega(r) = (GM/r^3)^{1/2}$, we get

$$\begin{aligned}\Omega_p(r) &= (-9.8\times10^{-3}\ {\rm s}^{-1})\sin^2\theta\mu_{30}^2\alpha_{-1}^{4/5}M_{1.4}^{-7/10} \\ &\quad\times\dot{M}_{17}^{-3/5}r_8^{-49/10}\mathcal{J}(r)^{-3/5}D(r)^{-1}, \qquad (2.17)\\ \Gamma_w(r) &= (7.7\times10^{-3}\ {\rm s}^{-1})\,\zeta\cos^2\theta\mu_{30}^2\alpha_{-1}^{4/5}M_{1.4}^{-7/10} \\ &\quad\times\dot{M}_{17}^{-3/5}r_8^{-49/10}\mathcal{J}(r)^{-3/5}. \qquad (2.18)\end{aligned}$$

Using $\nu_1 = \alpha H^2\Omega$, the viscosity rate is calculated as

$$\begin{aligned}\tau_{\rm visc}^{-1}(r) \equiv \frac{\nu_2(r)}{r^2} &= (1.4\times10^{-4}\ {\rm s}^{-1})\left(\frac{\nu_2}{\nu_1}\right)\alpha_{-1}^{4/5}M_{1.4}^{-1/5} \\ &\quad\times\dot{M}_{17}^{2/5}r_8^{-7/5}\mathcal{J}(r)^{2/5}. \qquad (2.19)\end{aligned}$$

With $W(r,t) = e^{i\sigma t}W(r)$, and using the dimensionless quantities $\hat{\sigma}$, $\hat{\Omega}_p$, and $\hat{\Gamma}_w$ as defined in eq. (2.11), we can write equation (2.7) in the dimensionless form:

$$\begin{aligned}&i\hat{\sigma}W - \left[\frac{3}{4}\left(1+\frac{2x\mathcal{J}'}{3\mathcal{J}}\right)+\frac{3\nu_1}{2\nu_2}\left(\frac{1}{\mathcal{J}}-1\right)\right]\left(\frac{\mathcal{J}}{x\mathcal{J}_{\rm in}}\right)^{2/5}\frac{dW}{dx} \\ &= \frac{x^{3/5}}{2}\frac{\mathcal{J}^{2/5}}{\mathcal{J}_{\rm in}^{2/5}}\frac{d^2W}{dx^2} + i\frac{\hat{\Omega}_p}{x^{4.9}}\frac{D_{\rm in}\mathcal{J}_{\rm in}^{3/5}}{D\mathcal{J}^{3/5}}W + \frac{\hat{\Gamma}_w}{x^{4.9}}\frac{\mathcal{J}_{\rm in}^{3/5}}{\mathcal{J}^{3/5}}W, \qquad (2.20)\end{aligned}$$

where $D_{\rm in} \equiv D(r_{\rm in})$, $\mathcal{J}_{\rm in} \equiv \mathcal{J}(r_{\rm in})$, and $\mathcal{J}' = d\mathcal{J}/dx$. Using eqs. (2.3), (2.5), and (2.15), we can calculate $D_{\rm in}$ as

$$D_{\rm in} = 0.14\left(\frac{\eta}{0.5}\right)^{1/40}\mu_{30}^{1/70}\alpha_{-1}^{-1/20}M_{1.4}^{-5/28}\dot{M}_{17}^{13/140}\mathcal{J}_{\rm in}^{1/10}. \tag{2.21}$$

[2]Magnetic fields threading the disk can modify $\mathcal{J}(r)$ in a model-dependent way (see Lai 1999 for an example). However, the basic feature can still be approximated by eq. (2.16).

Using eqs. (2.5) & (2.21) in eqs. (2.17), (2.18), & (2.19), we can calculate $\hat{\Omega}_p$ and $\hat{\Gamma}_w$ as

$$\hat{\Omega}_p = -38.0 \left(\frac{\nu_1}{\nu_2}\right)\left(\frac{\eta}{0.5}\right)^{-141/40}\left(\frac{\sin^2\theta}{0.5}\right)\mu_{30}^{-1/70}\alpha_{-1}^{1/20} \times M_{1.4}^{5/28}\dot{M}_{17}^{-13/140}\mathcal{J}_{\rm in}^{-11/10}, \quad (2.22)$$

$$\hat{\Gamma}_w = 21.4 \left(\frac{\nu_1}{\nu_2}\right)\left(\frac{\eta}{0.5}\right)^{-7/2}\left(\frac{\zeta}{5}\right)\left(\frac{\cos^2\theta}{0.5}\right)\mathcal{J}_{\rm in}^{-1}. \quad (2.23)$$

Note that under the assumptions of $\mathcal{J}(x) = 1$ and $D(x) = D_{\rm in}$, eq. (2.20) reduces to eq. (2.12) with $\mu = -0.6$.

2.3 Numerical Results

2.3.1 Mode Eigenfunction and Eigenvalue

We first consider the power-law disk models of §2.1. For a given set of parameters (μ, $\hat{\Omega}_p$, $\hat{\Gamma}_w$), equation (2.12) allows for many eigenmodes. We shall focus on the "fundamental" mode which is more concentrated near the inner edge of the disk and has larger $\hat{\sigma}_r$ (global precession frequency) and smaller $\hat{\sigma}_i$ (damping rate) than any other "higher-order" modes.

Fig. 1 shows the tilt angle $\beta(x, t = 0) = |W(x)|$ associated with the modes for different sets of ($\hat{\Omega}_p$, $\hat{\Gamma}_w$), all with $\mu = -0.6$ (corresponding to the "middle-region" α-disk with $\mathcal{J}(x) = 1$ and $D(x) = D_{\rm in}$). We see that as $|\hat{\Omega}_p|$ (note $\hat{\Omega}_p < 0$ due to retrograde precession) and $\hat{\Gamma}_w$ increase, the modes become more concentrated near the inner radius of the disk. This behavior can be understood heuristically: for a given $|\Omega_p(r_{\rm in})|$, a larger $|\hat{\Omega}_p|$ implies smaller viscosity [see eq. (2.11)], and thus the coupling between different disk radii is reduced, and the mode is less spread.

Fig. 2(a) shows the magnitude of the mode frequency ($\hat{\sigma}_r < 0$ due to retrograde precession) $|\hat{\sigma}_r|$ in units of $|\hat{\Omega}_p|$ as a function of $|\hat{\Omega}_p|$ for different values of $\hat{\Gamma}_w$. The

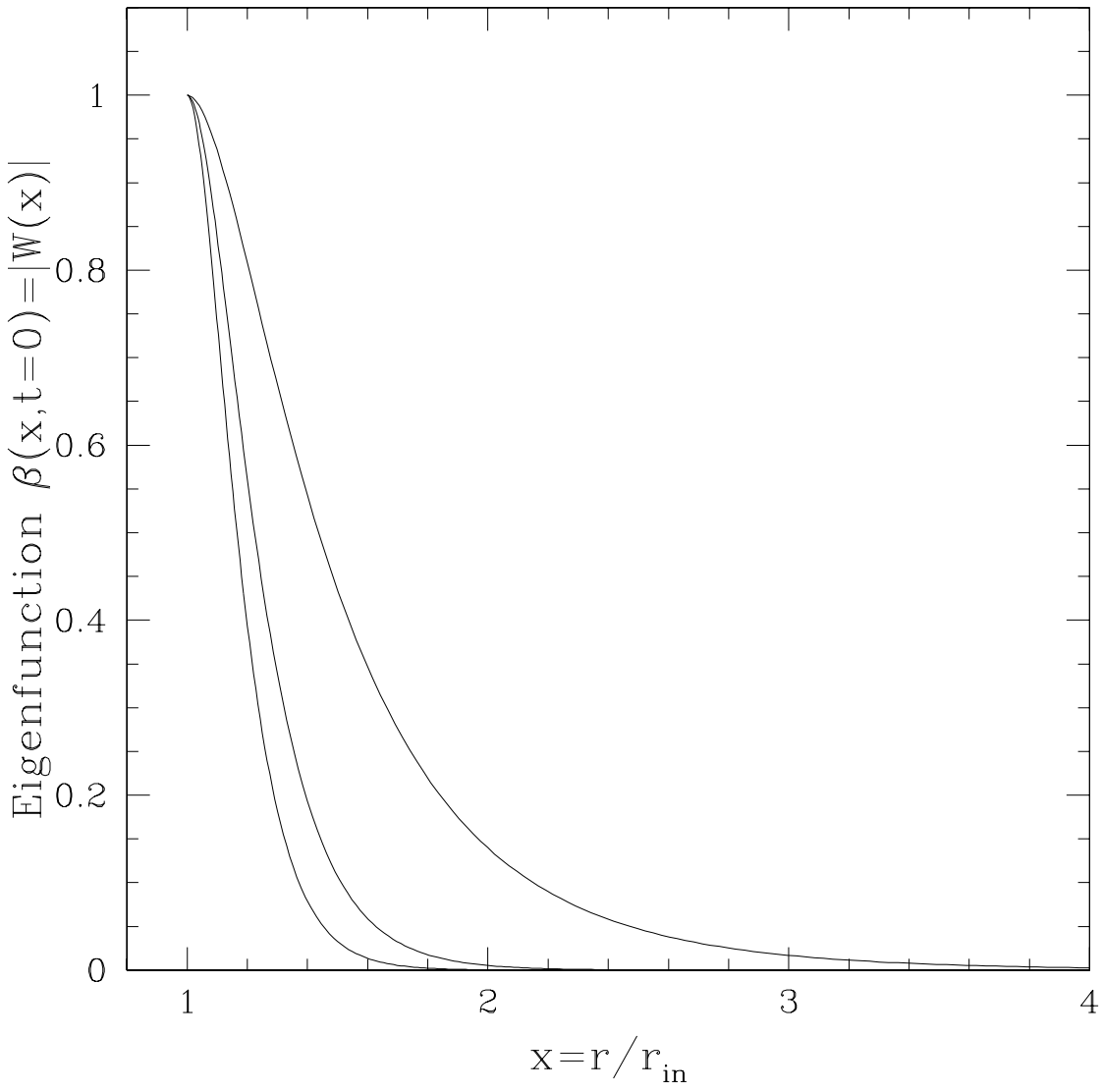

Figure 2.1: The disk tilt angle of the warping/precession modes as determined from eq. (2.12) with $\mu = -0.6$. The curves represent the fundamental modes for $(\hat{\Omega}_p, \hat{\Gamma}_m)$ $=(-10, 100)$, $(-100, 10)$, and $(-10, 10)$ from left to right, with the corresponding mode frequency $\hat{\sigma} = (\hat{\sigma}_r, \hat{\sigma}_i) = (-6.9, -57)$, $(-62, 12)$, and $(-4.2, -1.7)$. The eigenfunction is normalized such that the maximum tilt angle is 1.

ranges of $|\hat{\Omega}_p|$ and $\hat{\Gamma}_w$ are chosen to be from 10 to 1000 to cover possible values of parameters for accretion-powered X-ray pulsars [see eqs. (2.22) & (2.23) with $\mathcal{J}_{\rm in} = 1$]. We include the $\mu = -1.0$ and $\mu = 1.0$ results as well as the "middle region" $\mu = -0.6$ result to show how our results vary with the change of the surface density power-law. We see that $|\hat{\sigma}_r/\hat{\Omega}_p| = |\sigma_r/\Omega_p(r_{\rm in})|$ always lies between 0.3 to 0.85. The ratio $|\hat{\sigma}_r/\hat{\Omega}_p|$ increases as $|\hat{\Omega}_p|$ and $\hat{\Gamma}_w$ increase. This is consistent with the behavior of the mode eigenfunction (see Fig. 1) that a larger $|\hat{\Omega}_p|$ and $\hat{\Gamma}_w$ make the mode more concentrated near the inner disk edge.

2.3.2 Global Warping Instability Criterion

In the absence of magnetic warping torque ($\Gamma_w = 0$), we expect the disk warp to be damped by the viscous stress acting on the differential precession (Ω_p). This "magnetic Bardeen-Petterson effect" (Lai 1999) is analogous to the usual Bardeen-Petterson effect (Bardeen & Petterson 1975), where the combined effects of viscosity and differential Lense-Thirring precession align the rotation axis of the inner disk with the spin axis of the rotating black hole (or rotating, non-magnetic NS). The competition between the magnetically driven warping (Γ_w) and the magnetic Bardeen-Petterson damping can be determined by our global analysis.

Fig. 2(b) shows the damping rate $\hat{\sigma}_i$ as a function of $|\hat{\Omega}_p|$ for different values of $\hat{\Gamma}_w$. We see that $\hat{\sigma}_i$ decreases as $\hat{\Gamma}_w$ increases, and becomes negative (implying mode growth) when the ratio $\hat{\Gamma}_w/|\hat{\Omega}_p|$ is sufficiently large. By solving eq. (2.12) with $\mu = -0.6$, we find that the numerical value of $\hat{\sigma}_i$ can be approximated by

$$\hat{\sigma}_i = -a\hat{\Gamma}_w + b|\hat{\Omega}_p|^{0.6}, \tag{2.24}$$

with $a \sim (0.5 - 1.0)$ and $b \sim (0.5 - 1.0)$; this result is insensitive to modest change

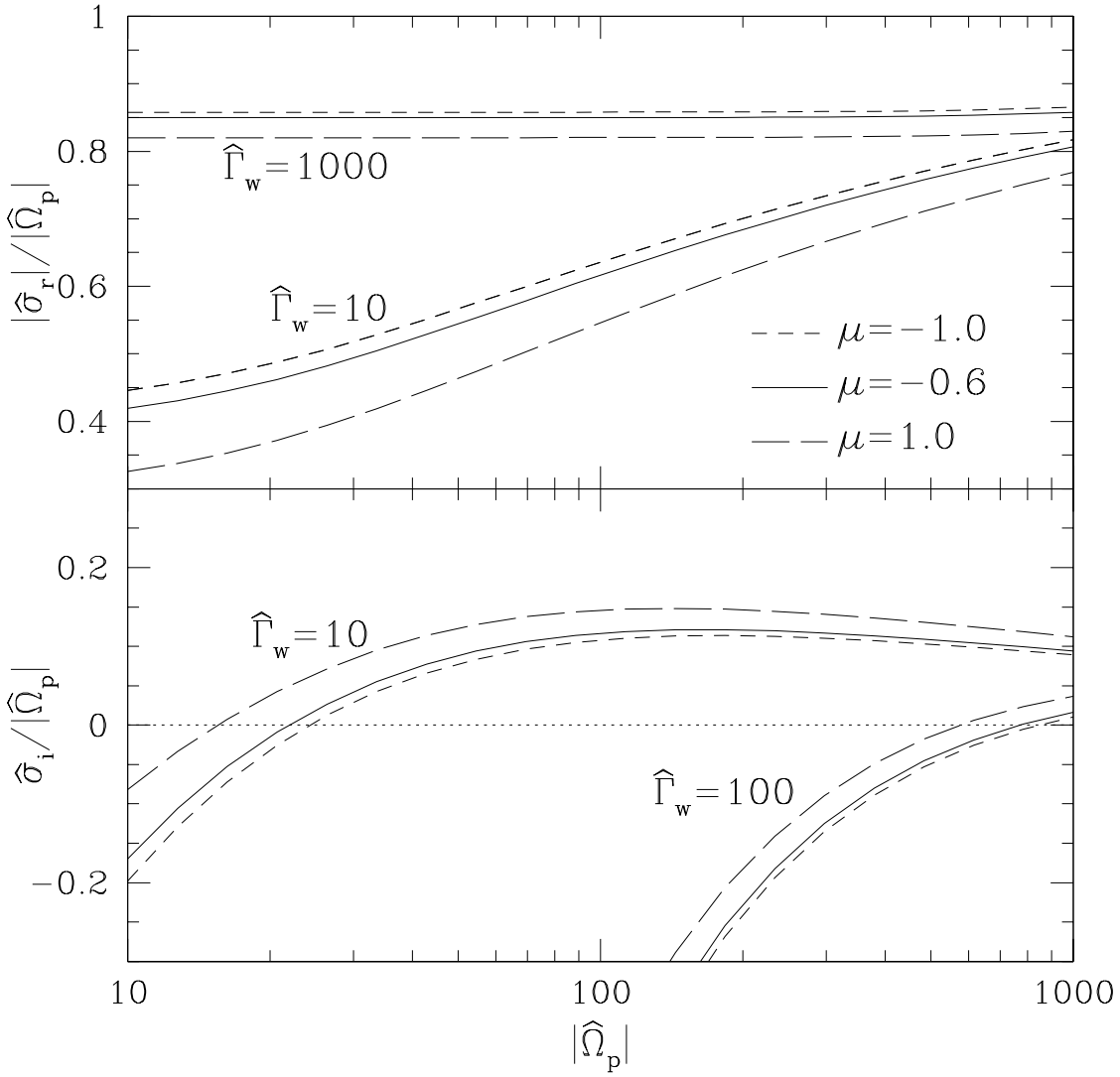

Figure 2.2: The upper panel shows the magnitude of the mode frequency $|\hat{\sigma}_r|$ in units of $|\hat{\Omega}_p|$ as a function of $|\hat{\Omega}_p|$ for different values of $\hat{\Gamma}_w$. Different surface density power-laws, $\Sigma \propto r^\mu$ with $\mu = -1$, -0.6 and 1, are adopted [see eq. (2.12)]. The lower panel shows the corresponding mode damping rate $\hat{\sigma}_i$ (in units of $|\hat{\Omega}_p|$). Note that negative $\hat{\sigma}_i$ implies growing mode.

of the surface density power-law ($\mu = -1$ to 1). For the mode to grow ($\hat{\sigma}_i < 0$) we require

$$\hat{\Gamma}_w \gtrsim 2|\hat{\Omega}_p|^{0.6} \iff \text{Global Warping Instability.} \tag{2.25}$$

Using eqs. (2.22) and (2.23), this condition becomes

$$1.6\left(\frac{\nu_1}{\nu_2}\right)^{0.4}\left(\frac{\eta}{0.5}\right)^{-1.39}\left(\frac{\zeta}{5}\right)\cos^2\theta\,(\sin^2\theta)^{-0.6}\mu_{30}^{0.0086} \times\alpha_{-1}^{-0.03}M_{1.4}^{-0.11}\dot{M}_{17}^{0.056}\mathcal{J}_{\rm in}^{-0.34} \gtrsim 1 \tag{2.26}$$

We see that for parameters which characterize X-ray pulsars the mode growth condition can be satisfied, although not always. In general, high (but not unreasonable) ζ (> a few) and small $\mathcal{J}_{\rm in}$ (see §3.3) are preferred to obtain growing modes.

2.3.3 Effect of $\mathcal{J}(r)$

The results of §3.1–3.2 are based on eq. (2.12), corresponding to eq. (2.20) with $D(x) = D_{\rm in}$ and $\mathcal{J}(x) = 1$. Here we consider the solutions of eq. (2.20) with the function $\mathcal{J}(x)$ given by eq. (2.16).

Fig. 3 shows the mode frequency $\hat{\sigma}$ as a function of $\mathcal{J}_{\rm in} = 1 - \xi$ [see eq. (2.16)] for three different sets of ($\hat{\Omega}_p$, $\hat{\Gamma}_w$): ($-38\mathcal{J}_{\rm in}^{-1.1}$, $21\mathcal{J}_{\rm in}^{-1}$), ($-7.6\mathcal{J}_{\rm in}^{-1.1}$, $38\mathcal{J}_{\rm in}^{-1}$), and ($-38\mathcal{J}_{\rm in}^{-1.1}$, $43\mathcal{J}_{\rm in}^{-1}$); these are obtained from eqs. (2.22) & (2.23) with ($\sin^2\theta$, ζ)=(0.5, 5), (0.1, 5), and (0.5, 10), respectively, while other parameters being fixed to the standard values [$\eta = 0.5$, $\nu_2/\nu_1 = 1$, $\mu_{30} = 1$, $\alpha_{-1} = 1$, $M_{1.4} = 1$, $\dot{M}_{17} = 1$]. In the calculations, we set $D(x) = D_{\rm in}$ for simplicity; using the more accurate function $D(x)$ given in eq. (2.3) only slightly changes the numerical results. We see from Fig. 3 that $|\hat{\sigma}_r/\hat{\Omega}_p|$ is insensitive to the choice of ξ since the most of the dependence on $\mathcal{J}_{\rm in}$ is already absorbed into the definition of $\hat{\Omega}_p$ [see eq. (2.22)].

We also see that a small $\mathcal{J}_{\rm in}$ tends to increase $\hat{\sigma}_i/|\hat{\Omega}_p|$, although growing warping modes still exist for a wide range of parameters. We find that the simple global warping instability criteria given in eqs. (2.25) and (2.26) can be used for $\mathcal{J}_{\rm in} > 0.1$. For smaller $\mathcal{J}_{\rm in}$ ($\lesssim 0.1$), $\hat{\sigma}_i$ should be obtained numerically to determine whether the mode grows or gets damped.

2.4 Applications to Milli-Hertz QPO's in Accreting X-ray Pulsars

QPOs with frequencies $1 - 100$ mHz have been detected in at least 11 accreting X-ray pulsars (Table 1; see also Boroson et al. 2000). These mHz QPOs are often interpreted in terms of the beat frequency model (BFM; Alpar & Shaham 1985; Lamb et al. 1985) or the Keplerian frequency model (KFM; van der Klis et al. 1987). In the BFM, the observed QPO frequency represents the beat between the Keplerian frequency ν_K at the inner disk radius $r_{\rm in}$ and the NS spin frequency ν_s [i.e., $\nu_{\rm QPO} = \nu_K(r_{\rm in}) - \nu_s$]. In the KFM, the QPOs arise from the modulation of the X-rays by some inhomogeneities in the inner disk at the Keplerian frequency [i.e., $\nu_{\rm QPO} = \nu_K(r_{\rm in})$]. However, we see from Table 1 that for several sources, more than one QPOs have been detected and the difference in the QPO frequencies is not equal to the spin frequency. Thus it is evident that the KFM and/or the BFM cannot be the whole story. We also note that in both the KFM and the BFM, it is always postulated that the inner disk contain some blobs or inhomogeneities, whose physical origin is unclear.

Here we suggest a "Magnetic Disk Precession Model" (MDPM) for the mHz variabilities and QPOs of accreting X-ray pulsars. The magnetically driven preces-

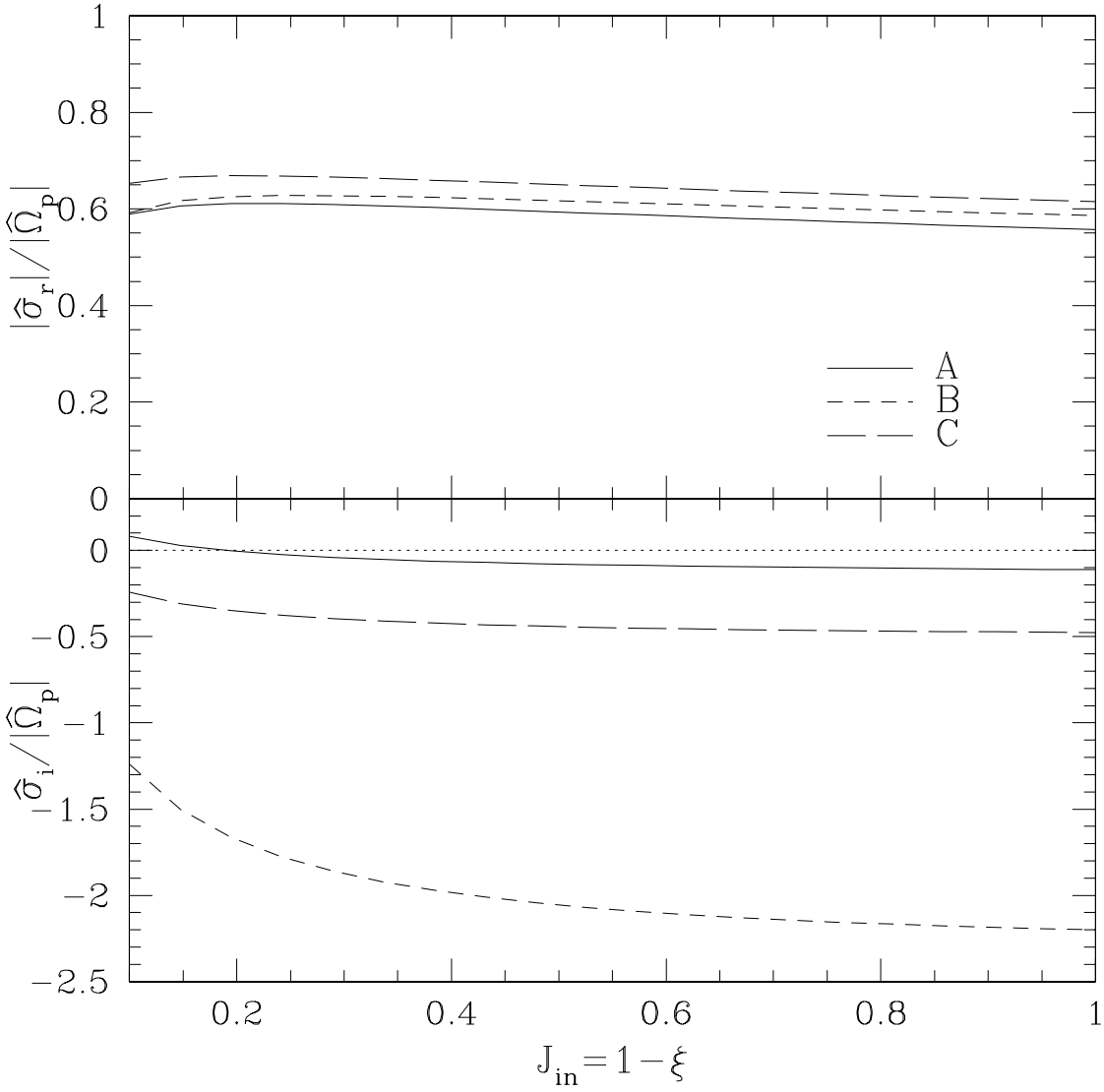

Figure 2.3: The upper panel shows the magnitude of the mode frequency $|\hat{\sigma}_r|$ in units of $|\hat{\Omega}_p|$ as a function of $\mathcal{J}_{\rm in} = 1 - \xi$ for differet parameter sets A, B, and C: $(\hat{\Omega}_p,\, \hat{\Gamma}_w) = (-38\mathcal{J}_{\rm in}^{-1.1},\, 21\mathcal{J}_{\rm in}^{-1})$, $(-7.6\mathcal{J}_{\rm in}^{-1.1},\, 38\mathcal{J}_{\rm in}^{-1})$, and $(-38\mathcal{J}_{\rm in}^{-1.1},\, 43\mathcal{J}_{\rm in}^{-1})$, respectively (see the text). The lower panel shows the corresponding mode damping rate $\hat{\sigma}_i$ (in units of $|\hat{\Omega}_p|$). Note that negative $\hat{\sigma}_i$ implies growing mode.

Table 2.1: Accretion-powered X-ray pulsars with mHz QPOs. [a]References: [1] Shinoda et al. 1990; [2] Chakrabarty 1998; [3] Chakrabarty et al. 2001; [4]† Orlandini et al. 1998; [5] Boroson et al. 2000; [6] Moon & Eikenberry 2001b; [7]† Makishima et al. 1999; [8] Wojdowski et al. 1998; [9] Takeshima et al. 1991; [10] Moon & Eikenberry 2001a; [11]† La Barbera et al. 2001; [12] in't Zand et al. 1998; [13] Makishima & Mihara 1992; [14] Angelini et al. 1989; [15] Soong & Swank 1989; [16] Heindl et al. 1999; [17] Paul & Rao 1998; [18] Takeshima et al. 1994; [19]† Makishima et al. 1990; [20] Finger et al. 1996; [21]† Grove et al. 1995. These references include QPO discovery (no mark) and magnetic field strength B estimated from cyclotron features (with †). [b]The magnetic moment is calculated by $\mu = BR^3$, or $\mu_{30} = B_{12}R_6^3$. We assume $R = 10$ km, or $R_6 = 1$ here. [c] marginal detection.

System	Spin frequency ν_s [mHz]	QPO frequency $\nu_{\rm QPO}$ [mHz]	Magnetic moment μ_{30} [b]	References[a]
4U 1626–67	130	1, 48	3.3	1, 2, 3, 4†
Her X–1	807.9	8, 12, 43	3	5, 6, 7†
SMC X-1	1410	(60)[c]	...	8
Cen X-3	207	35	...	9
LMC X-4	74	0.65–1.35, 2–20	11	10, 11†
4U 1907+09	2.27	55	2.5	12, 13†
EXO 2030+375	24	187–213	...	14
4U 0115+63	277	2, 62	1.5	15, 16
XTE J1858+034	4.5	111	...	17
V 0332+53	229	51	2.5	18, 19†
A 0535+262	9.71	27–72	9.5	20, 21†

sion of the warped inner disk (outside but close to the magnetosphere boundary) can modulate X-ray/UV/optical flux in several ways: (i) The observed radiation (in UV and optical, depending on $r_{\rm in}$) from the inner disk due to intrinsic viscous dissipation varies as the angle between the local disk normal vector and the line-of-sight changes during the precession; (ii) The flux of reprocessed UV/optical disk emission visible along our sight also varies as the reprocessing geometry evolves; (iii) Modulation of the X-ray flux arises from regular occulation/obscuration of the radiation from the central NS and magnetosphere by the precessing inner disk. In the MDPM, we identify $\nu_{\rm QPO}$ with the global precession frequency driven by the magnetic torques. Our calculations in §3 show that under a wide range of conditions, the warping/precession mode is concentrated near the disk inner edge, and the global mode frequency is equal to $A = 0.3 - 0.85$ (depending on details of the disk structure) times the magnetically driven precession frequency at $r_{\rm in} = r_m$. Thus we write $\nu_{\rm QPO} = A|\Omega_p(r_{\rm in})|/2\pi$. Using eq. (2.17) together with eqs. (2.5), (2.14), and (2.21), we have (for the α-disk model),

$$\begin{aligned}
\nu_{\rm QPO} &= (15.7\ {\rm mHz}) A \sin^2\theta\, \mu_{30}^2 \alpha_{-1}^{4/5} M_{1.4}^{-7/10} \dot{M}_{17}^{-3/5} \\
&\quad \times \left(\frac{r_{\rm in}}{10^8\ {\rm cm}}\right)^{-49/10} \left(\frac{D_{\rm in}}{0.1}\right)^{-1} \mathcal{J}_{\rm in}^{-3/5} \\
&= (0.83\ {\rm mHz})\, A \left(\frac{\eta}{0.5}\right)^{-4.93} \sin^2\theta\, \mu_{30}^{-0.81} \\
&\quad \times \alpha_{-1}^{0.85} M_{1.4}^{0.18} \dot{M}_{17}^{0.71} \mathcal{J}_{\rm in}^{-0.7}. \qquad (2.27)
\end{aligned}$$

We also note that the Keplerian frequency at $r = r_{\rm in} = r_m$ is

$$\nu_K(r_{\rm in}) = (985\ {\rm mHz}) \left(\frac{\eta}{0.5}\right)^{-3/2} \mu_{30}^{-6/7} M_{1.4}^{5/7} \dot{M}_{17}^{3/7}. \qquad (2.28)$$

We see from eq. (2.27) that the MDPM can produce QPOs with frequencies of order 1 mHz; larger values of $\nu_{\rm QPO}$ would require $\mathcal{J}_{\rm in} \ll 1$ (corresponding to low

surface density at $r_{\rm in}$). The value of $\mathcal{J}_{\rm in}$ depends on details of the physics at the inner edge of the disk, therefore is uncertain. Let $V_r(r_{\rm in}) = \chi c_s(r_{\rm in})$, where $V_r = \dot{M}/(2\pi r\Sigma)$ is the radial velocity and $c_s = H\Omega$ is the sound speed of the disk, we find

$$\mathcal{J}_{\rm in} \simeq 3.1\times 10^{-4}\chi^{-5/4}\alpha_{-1}^{9/8}M_{1.4}^{-7/16}\dot{M}_{17}^{1/4}\left(\frac{r_{\rm in}}{10^8\ {\rm cm}}\right)^{1/16}. \tag{2.29}$$

Setting $\chi = 1$ would give the minimum value of $\mathcal{J}_{\rm in}$.

We now discuss several individual sources.

2.4.1 4U 1626+67

The LMXB 4U 1626+67 consists of a $\nu_s = 130$ mHz X-ray pulsar in a 42 min orbit with very low-mass ($\lesssim 0.1\,M_\odot$) companion (see Chakrabarty 1998). QPOs at 48 mHz (and oscillations at 130 mHz) have been detected simultaneously in X-rays and in the optical/UV band (Shinoda et al. 1990; Chakrabarty 1998; Chakrabarty et al. 2001). Thus it is natural to attribute the optical/UV variability to the reprocessing of the variable X-ray emission in the accretion disk. Since $\nu_s > 48$ mHz, the KFM is problematic because the propeller effect would inhibit accretion when $\nu_s > \nu_K(r_m)$. (It is still possible to ascribe the QPO to Keplerian motion at some radius farther out in the disk, but this is rather ad hoc.) The BFM is a viable alternative for the 48 mHz QPO.

Recent HST observations by Chakrabarty et al. (2001) revealed a strong QPO around 1 mHz (centroid frequency in the range of 0.3–1.2 mHz, and $Q = \nu/\Delta\nu$ of order 10) in the optical/UV band. This QPO is absent in simultaneous X-ray data, and is stronger in UV and weaker in the optical band. These features can be naturally explained as due to warping of the inner accretion disk (see Chakrabarty et al. 2001). Indeed, using $B \simeq 3\times 10^{12}$ G (from BeppoSAX observations of

a cyclotron feature; Orlandini et al. 1998) and $\dot{M}_{17} \simeq 1$ (corresponding to X-ray luminosity $L_X \simeq 10^{37}$ erg/s; Chakrabarty 1998), eq. (2.27) yields $\nu_{\rm QPO} \simeq 0.34\, A\, (\eta/0.5)^{-4.9} \sin^2\theta\, \alpha_{-1}^{0.85} \mathcal{J}_{\rm in}^{-0.7}$ mHz, which can easily give the observed $\nu_{\rm QPO} =$ 1 mHz provided we allow for $\mathcal{J}_{\rm in} < 1$ [see eq. (2.29)]. If we interpret the 48 mHz QPO with the BFM, we have $\nu_K(r_{\rm in}) = 178$ mHz and $\eta \simeq 0.83$, we therefore require $\mathcal{J}_{\rm in} \lesssim 0.01$ (depending on α and $\sin^2\theta$).

2.4.2 Other Sources

For the other sources listed in Table 1, no "smoking-gun" signature of warped disk has been observed. However, the numerical values of QPO frequencies indicate that the MDPM may be at work.

Her X–1: This well-studied binary X-ray pulsar ($\nu_s = 808$ mHz) shows QPOs in the UV and optical bands at frequencies of 8 ± 2 and 43 ± 2 mHz; these QPOs most likely arise from the reprocessing of the disk oscillations by the companion star (Boroson et al. 2000). A QPO at 12 mHz in X-rays is also present, but its connection with the 8 mHz QPO is not clear (Moon & Eikenberry 2001b). Since $\nu_s > \nu_{\rm QPO}$, the KFM is not applicable. The BFM predicts $\nu_K(r_{\rm in}) = 816$ mHZ and 851 mHZ for $\nu_{\rm QPO} = 8$ mHz and 43 mHz respectively. For $\mu_{30} \simeq 3$ (see Table 1) , $\dot{M}_{17} \simeq 1$ (corresponding to $L_X \simeq 10^{37}$ ergs; Choi et al. 1994), and $M_{1.4} \simeq 1$, we have $\nu_K(r_{\rm in}) \simeq 400\, (\eta/0.5)^{-3/2}$ mHz. Thus to explain the 8 mHz or 43 mHz QPO with the BFM requires $\eta < 0.5$. The phenomenology of the 12 mHz X-ray QPO is consistent with disk precession (see Moon & Eikenberry 2001b); this may be explained by the MDPM.

LMC X–4: This persistent X-ray pulsar ($\nu_s = 74$ mHz) exhibits large X-ray flares. QPOs at frequencies of 0.65-1.35 mHz and 2-20 mHz have been found

during such flares (Moon & Eikenberry 2001a). Since $\nu_s > \nu_{\rm QPO}$, the KFM is not applicable. The BFM predicts $\nu_K(r_m) \simeq 75$ mHz and $\simeq 76-94$ mHz for $\nu_{\rm QPO} = 0.65-1.35$ mHz and $2-20$ mHz, respectively. Equation (2.28) with the measured $\mu_{30} \simeq 11$ (see Table 1) and $\dot{M}_{17} \simeq 25$ (corresponding to $L_X \simeq 5\times10^{38}$ ergs; Moon & Eikenberry 2001a) gives $\nu_K(r_{\rm in}) = 502\,(\eta/0.5)^{-3/2}$ mHz, which is much larger than the values of $\nu_K(r_{\rm in})$ required by the BFM (even for $\eta = 1$). Hence, it is difficult, if not impossible, to identify the observed QPO frequencies (especially for $\nu_{\rm QPO} = 0.65-1.35$ mHz) with the beat frequency. On the other hand, eq. (2.27) gives $\nu_{\rm QPO} \simeq 1.2\,A\,(\eta/0.5)^{-4.9}\sin^2\theta\,\alpha_{-1}^{0.85}\mathcal{J}_{\rm in}^{-0.7}$ mHz, which is close to the observed $\nu_{\rm QPO} = 0.65-1.35$ mHz.

4U 0115+63: This transient source shows a broad 62 mHz QPO during a flaring state (Soong & Swank 1989). Recent XTE observation also reveals a prominent QPO in the X-ray flux at 2 mHz (Heindl et al. 1999). Heindl et al. (1999) noted that this 2 mHz QPO may be explained by occultation of the radiation beam by the accretion disk. Analogous to the 1 mHz QPO of 4U 1626+67 (see §4.1), we suggest that magnetically driven disk warping/precession may be responsible for such occultation. With the well-measured magnetic field ($B \simeq 1.3\times10^{12}$ G) of the NS from the cyclotron lines, similar constraints on the system parameters can be obtained.

For other sources listed in Table 1, either only single QPO is known, or there is no independent measurement/constraint on μ_{30} and $\dot{M}$, thus the theoretical interpretation is currently ambiguous.

2.5 Conclusions

We have shown in this chapter that the inner region of the disk around a strongly magnetized ($\sim 10^{12}$ G) neutron star can be warped and will precess around the stellar spin (see Lai 1999). These effects arise from the interactions between the stellar field and the induced currents in the disk (before it is disrupted at the magnetosphere boundary). We have carried out a global analysis of the warping/precession modes and found that growing modes exist for a wide range of parameters typical of accreting X-ray pulsars. We therefore expect that the magnetically driven warping/precession effect will give rise to variabilities/QPOs in the X-ray/UV/optical fluxes. We have suggested that some mHz QPOs observed in several systems (e.g., 4U 1626-67) are the results of these new magnetic effects. Although there are significant uncertainties in the physical conditions of the magnetosphere-disk boundary [and these uncertainties prohibit accurate calculation of the QPO frequency; see eq. (2.27)], we emphasize that the existence of these effects is robust. Continued study of the variabilities of X-ray pulsar systems would provide useful constraints on the magnetosphere–disk interactions.

Chapter 3

Oscillations of Presupernova Stars

3.1 Introduction

It has long been recognized that neutron stars may have received large kick velocities at birth. The observed neutron star velocities are much larger than their progenitors' velocities. Measurements of pulsar proper motions indicate typical velocities of $100 - 500\,\mathrm{km\,s^{-1}}$, with a significant population having velocities greater than $1000\,\mathrm{km\,s^{-1}}$ (Lyne & Lorimer 1994; Lorimer, Bailes, & Harrison 1997; Hansen & Phinney 1997; Cordes & Chernoff 1998; Arzoumanian, Chernoff, & Cordes 2002; Hobbs et al. 2005). A statistical study by Arzoumanian, Chernoff, & Cordes (2002) gives a bimodal pulsar velocity distribution with peaks at $100\,\mathrm{km\,s^{-1}}$ and $500\,\mathrm{km\,s^{-1}}$. A parallax study of the velocities of 14 pulsars is consistent with this result (Chatterjee et al. 2005). On the other hand, a recent study by Hobbs et al. (2005) favors a single Gaussian distribution with a mean three-dimensional pulsar velocity of 400 $\mathrm{km\,s^{-1}}$. There are other observational evidences for large neutron star velocities. Observations of a bow shock from the Guitar Nebula Pulsar (B2224+65) implies a pulsar velocity greater than $1000\,\mathrm{km\,s^{-1}}$ (Chatterjee & Cordes 2002). Some of the association studies of neutron stars and supernova remnants also imply large neutron star velocities (e.g., neutron star in Cas A SNR has a traverse velocity of $\sim 330\,\mathrm{km\,s^{-1}}$; Thorstensen, Fesen, & van den Bergh 2001).

While large neutron star velocities can in principle be explained by binary breakup (Iben & Tutukov 1996) many observed characteristics of neutron star binaries can be explained only if there is a kick at birth. The spin-orbit misalignment in PSR J0045-7319/B star binary implied by the orbital plane precession

(Lai, Bildsten, & Kaspi 1995; Kaspi et al. 1996) and the fast orbital decay (Lai 1996; Kumar & Quataert 1997) requires a neutron star kick. Similar orbital plane precession has been observed in PSR J1740-3052 (Stairs et al. 2003). The geodesic precession in binary pulsar PSR B1913+16 also implies a spin-orbit misalignment and requires a neutron star kick (Kramer 1998; Wex, Kalogera, & Kramer 2000). A study of the system radial velocity ($430\,\mathrm{km\,s^{-1}}$) of X-ray binary Circinus X-1 requires a kick velocity greater than $430\,\mathrm{km\,s^{-1}}$ (Tauris et al. 1999). High eccentricities of some Be/X-ray binaries cannot be explained without kicks (van den Heuvel & van Paradijs 1997). Evolutionary scenarios of double neutron star systems also indicate the existence of kicks (Fryer, Burrows, & Benz 1998). In addition, asymmetric supernova explosions have been found by direct observations of many nearby supernova explosions (Wang, Johnston, & Manchester 2004) and supernova remnants (Hwang et al. 2004). By momentum conservation, asymmetric supernova explosions indicate that neutron stars get a kick at birth.

Many neutron star kick mechanisms have been proposed so far. They roughly fall into the following three categories (see Wang, Lai, & Han 2006): magnetic-neutrino driven kick mechanism, electromagnetically driven kick mechanism, and hydrodynamically driven kick mechanism. The viabilities of the first two types of kick mechanism depend on important parameters of a nascent neutron star (i.e., protoneutron star) such as the magnetic field strength and the spin period. For example, the magnetic-neutrino driven kick mechanism that relies on asymmetric neutrino emission due to the strong magnetic field requires the magnetic field strength greater than $10^{15}\,\mathrm{G}$. On the other hand, the electromagnetically driven kick mechanism that relies on electromagnetic emission from an off-centered magnetic dipole in a neutron star requires the initial spin period $\lesssim 2$ ms (Harrison

& Tademaru 1975). Among the proposed kick mechanisms, versions of the hydrodynamically driven kick mechanism are considered to be the most compelling. There are two proposals of hydrodynamically driven kick mechanism. The first proposal relies on the hydrodynamic instabilities that develop after the core collapse. Recent two- and three-dimensional simulations have produced successful supernova explosions and have demonstrated that hydrodynamic instabilities can lead to global asymmetries of the fluid flow in the neutrino-heated layer behind the supernova shock, resulting in neutron star velocities greater than several hundred $\mathrm{km\,s^{-1}}$ (Schenk et al. 2004; Janka et al. 2004). The second proposal relies on the growth of asymmetric perturbations already present in the presupernova star. It has been recognized that if there are sufficiently large global asymmetric perturbations in a persupernova core, they are amplified during the core collapse. Then the shock wave produced at the core bounce sees the non-uniform densities in the outer core and propagates non-spherically. This leads to an asymmetric mass ejection. Goldreich, Lai, & Sharling (1997) has proposed that the gravity modes (g-modes), oscillation modes of a star whose restoring force is gravity, trapped in the presupernova core may be amplified by the nuclear energy generation (i.e., the ε-mechanism) in the Si burning shell and give rise to such global asymmetric perturbations. We explore this idea by performing a linear analysis of oscillation modes of the presupernova cores to determine whether the core g-modes would grow large enough before the onset of the core collapse.

The rest of the chapter is organized as follows. In § 3.2, we discuss presupernova stars and their oscillation modes. In § 3.3, we present the linear perturbation equations, boundary conditions, and mode growth/damping rate. The numerical results are summarized in § 3.4. § 3.5 is devoted to discussion and conclusions.

We note that similar results as ours presented in § 3.4 were obtained by Murphy, Burrows, & Heger (2004) while our work was being completed.

3.2 Presupernova Stars and Their Oscillation Modes

The last stage of nuclear burning in the core of a massive star is the fusion of silicon. This involves photodissociation of silicon and other nuclei present that produces neutrons, protons, and most importantly α particles. These particles then add on successively to the remaining nuclei, producing iron-peak elements. The temperature required for these processes is $\gtrsim 3\times10^9$ K. As the silicon fuel runs out in the core, the core consisting mostly of iron contracts, and the temperature just outside the core increases to make the silicon around the core burn. The core contraction is enhanced by neutrino cooling due to electron captures, and at the central density of order a few times $10^9\,\mathrm{g\,cm^{-3}}$, the core starts to collapse. The core Si burning phase lasts for days and the subsequent shell Si burning phase lasts for about a day before the core collapse.

We are interested in the oscillation modes of presupernova stars. We assume that mode growth/damping is much faster than the evolution of a presupernova star. We use two presupernova models provided by Heger (Heger 2004; private communication). The initial mass of the presupernova star is $15M_\odot$ in the first model, and is $25M_\odot$ in the second model. These two models represent the following two families of core structures before the core collapse: (i) low-entropy, compact, low-mass Fe cores surrounded by mantles with steep density profiles, and (ii) high-entropy, non-compact, high-mass Fe cores surrounded by mantles with slowly-varying density profiles. We consider these two models at three different time epochs: 200, 20, and 2 seconds before the onset of core collapse ($t = -200$, -20,

and -2 s). For the $15_{\odot}$ model, the density ρ, temperature T, and electron fraction Y_e are shown in Fig. 3.1, and the total energy generation rate, including the nuclear energy generation and the neutrino energy loss, is shown in Fig. 3.2. From these figures, we can identify three important structural boundaries:

(a) At $1.05M_{\odot}$: This is the top of the "old" Fe core formed by the core Si burning and the base of the "new" Fe mantle formed by the more recent shell Si burning. The temperature T takes a local maximum due to the hot "new" Fe mantle. The electron fraction Y_e decreases (i.e., becomes more neutron rich) toward the center and it also decreases with time. In the "old" Fe core, the neutrino energy loss rate increases toward the center. In the "new" Fe mantle, the neutrino energy loss rate is very large due to its hot temperature.

(b) At $1.32M_{\odot}$: This is the top of the Fe core, including the "old" Fe core and the "new" Fe mantle, and the base of the Si burning shell. There is a major discontinuity in Y_e due to the change in nuclear elements.

(c) At $1.84M_{\odot}$: This is the top of the Si shell and the base of the O burning shell. There is a discontinuity in the temperature, therefore in the density too, while keeping the pressure continuous across the boundary.

For the $25M_{\odot}$ model, similar figures are given in Figs. 3.3 and 3.4. The three structural boundaries are located at (a) $1.03M_{\odot}$, (b) $1.62M_{\odot}$, and (c) $1.97M_{\odot}$.

The WKB analysis gives the dispersion relation

$$k_r^2 = \frac{(\sigma^2 - L_\ell^2)(\sigma^2 - N^2)}{\sigma^2 c_{\rm s}^2}, \tag{3.1}$$

where we have assumed that the perturbations are of the form $\propto e^{ik_r r - i\sigma t}$ (k_r: radial wave number, σ: mode frequency). Here L_ℓ is the Lamb frequency, the characteristic frequency for the pressure-mode (p-mode; sound wave), and N is the Brunt-Väisälä frequency, the characteristic frequency for the g-mode. They

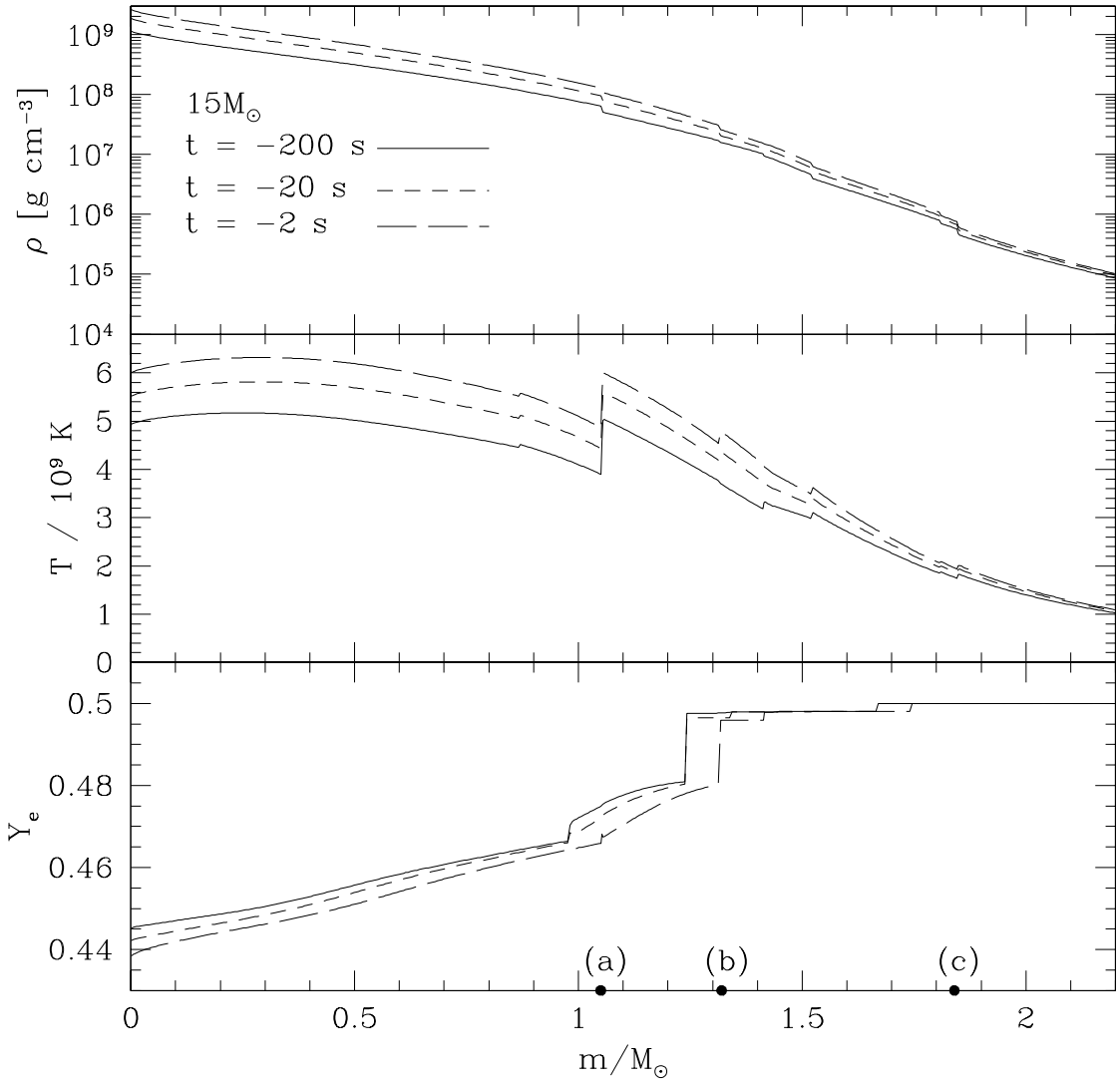

Figure 3.1: Profiles of various physical quantities for the $15M_\odot$ model. Density ρ, temperature T, and electron fraction Y_e are plotted as functions of mass m (in units of $M_\odot$) from top to bottom for the $15M_\odot$ model at $t = -200$ s (solid lines), $t = -20$ s (short dashed lines), and $t = -2$ s (long dashed lines). The three structural boundaries discussed in the text are indicated on the mass axis: (a) top of the "old" Fe core and the base of the "new" Fe mantle, (b) top of the "new" Fe mantle and the base of the Si burning shell, and (c) top of the Si shell and the base of the O burning shell.

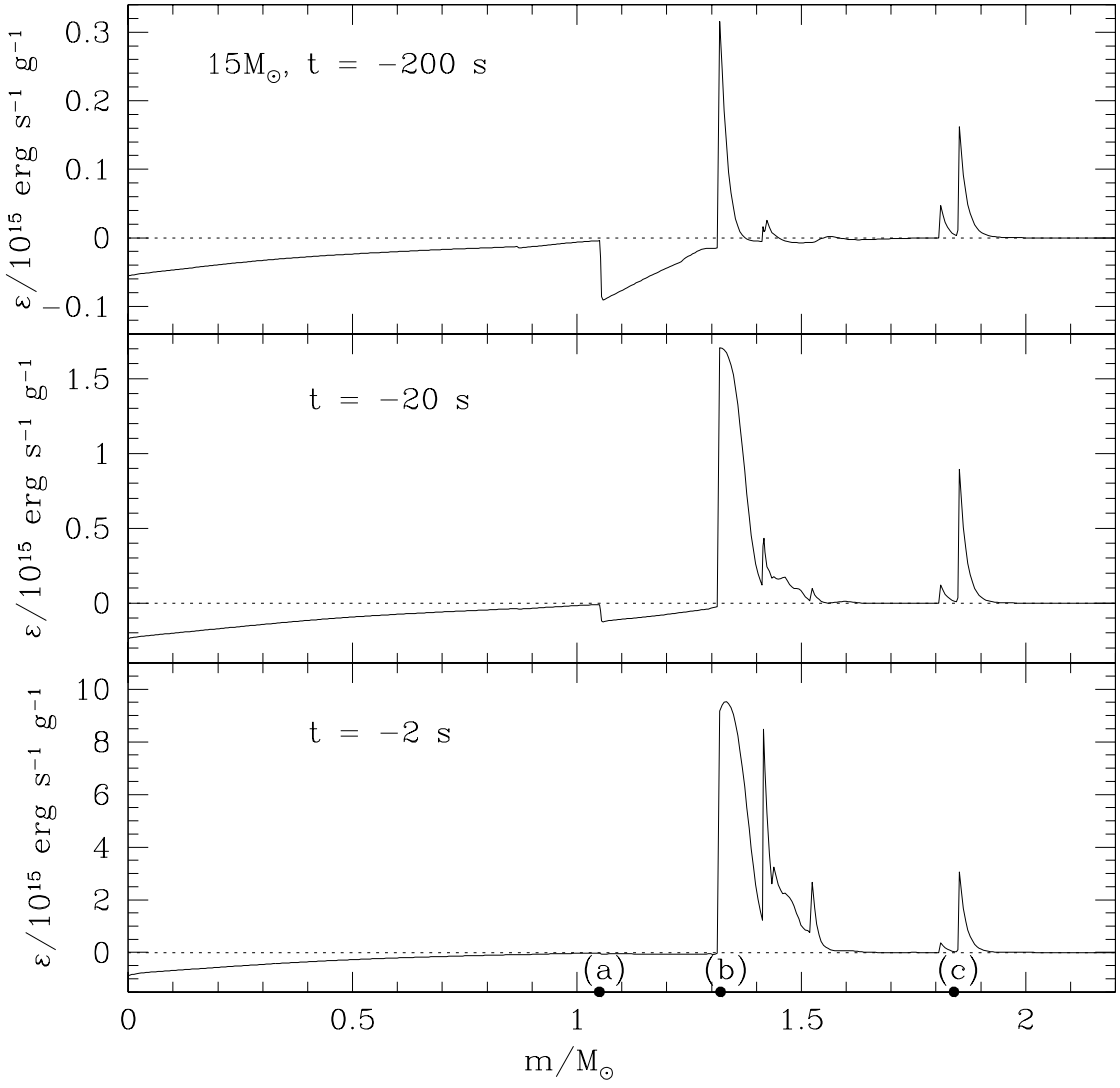

Figure 3.2: Total energy generation rate $\varepsilon = \varepsilon_{\rm nuc} + \varepsilon_\nu$ for the $15M_\odot$ model at $t = -200$, -20, and -2 s (from top to bottom). ε is given in units of 10^{15} erg s^{-1} g^{-1}. The three structural boundaries (a), (b), and (c) are indicated on the mass axis.

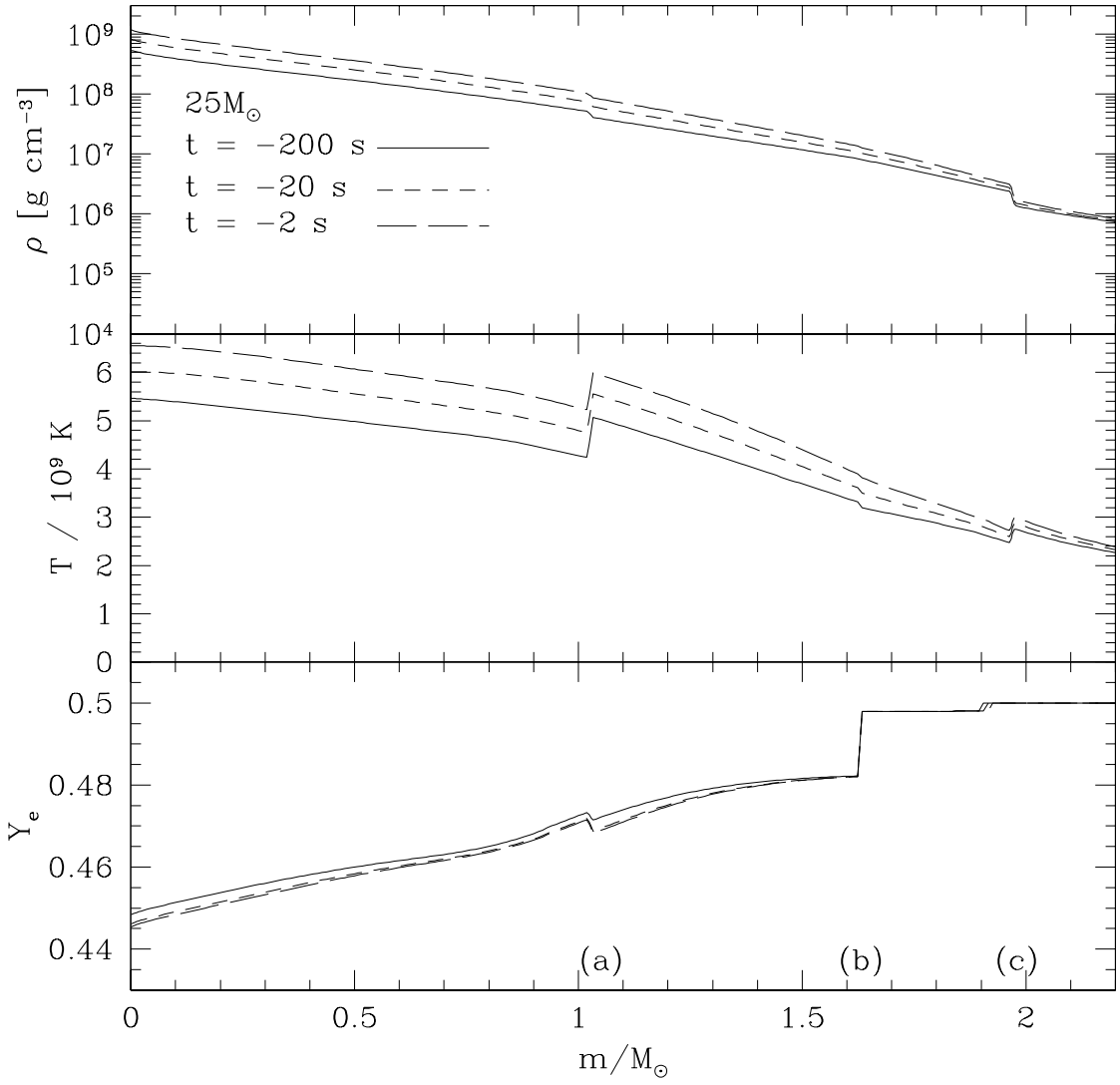

Figure 3.3: Similar to Fig. 3.1 but for the $25M_{\odot}$ model.

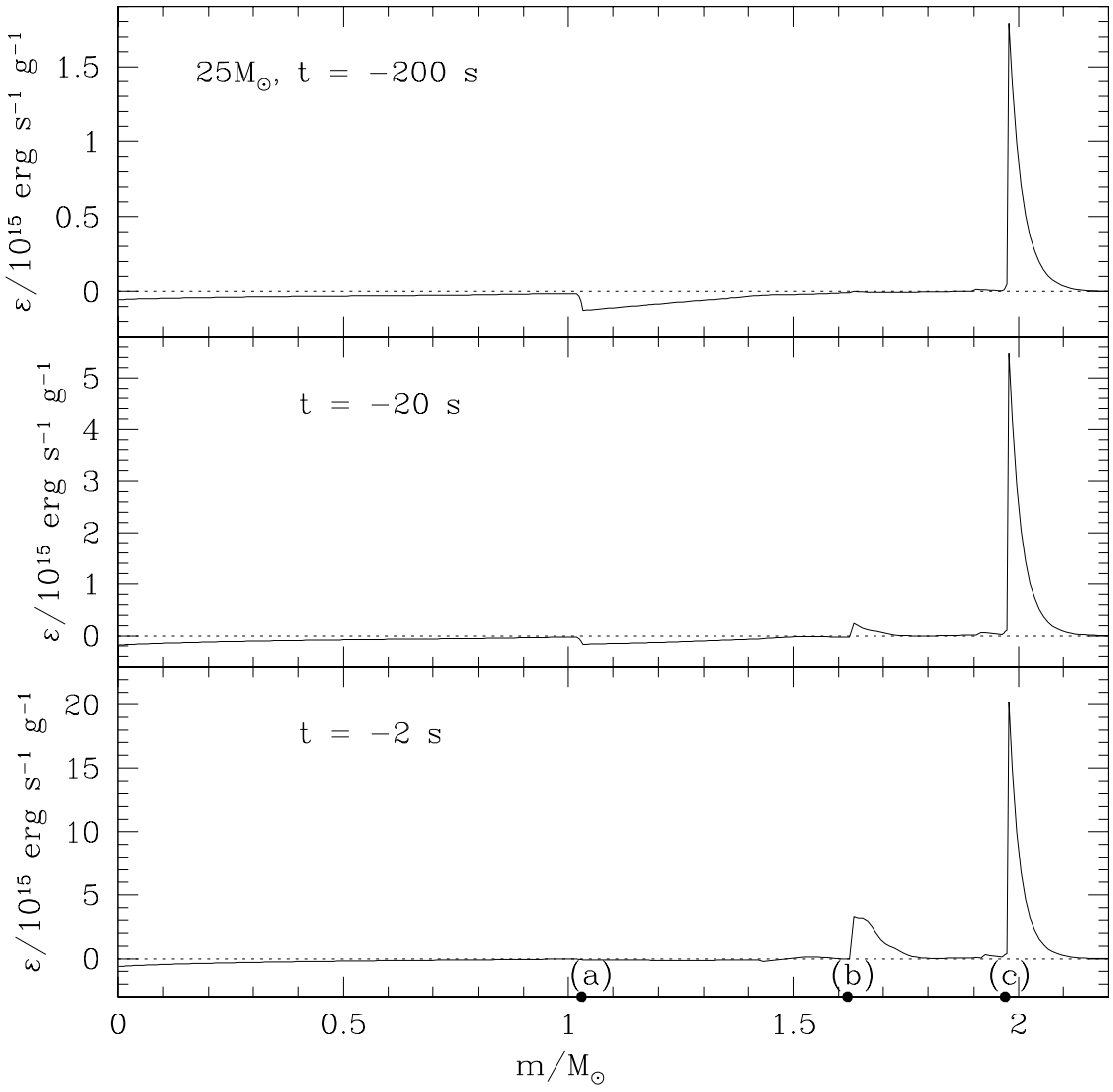

Figure 3.4: Similar to Fig. 3.2 but for the $25M_{\odot}$ model.

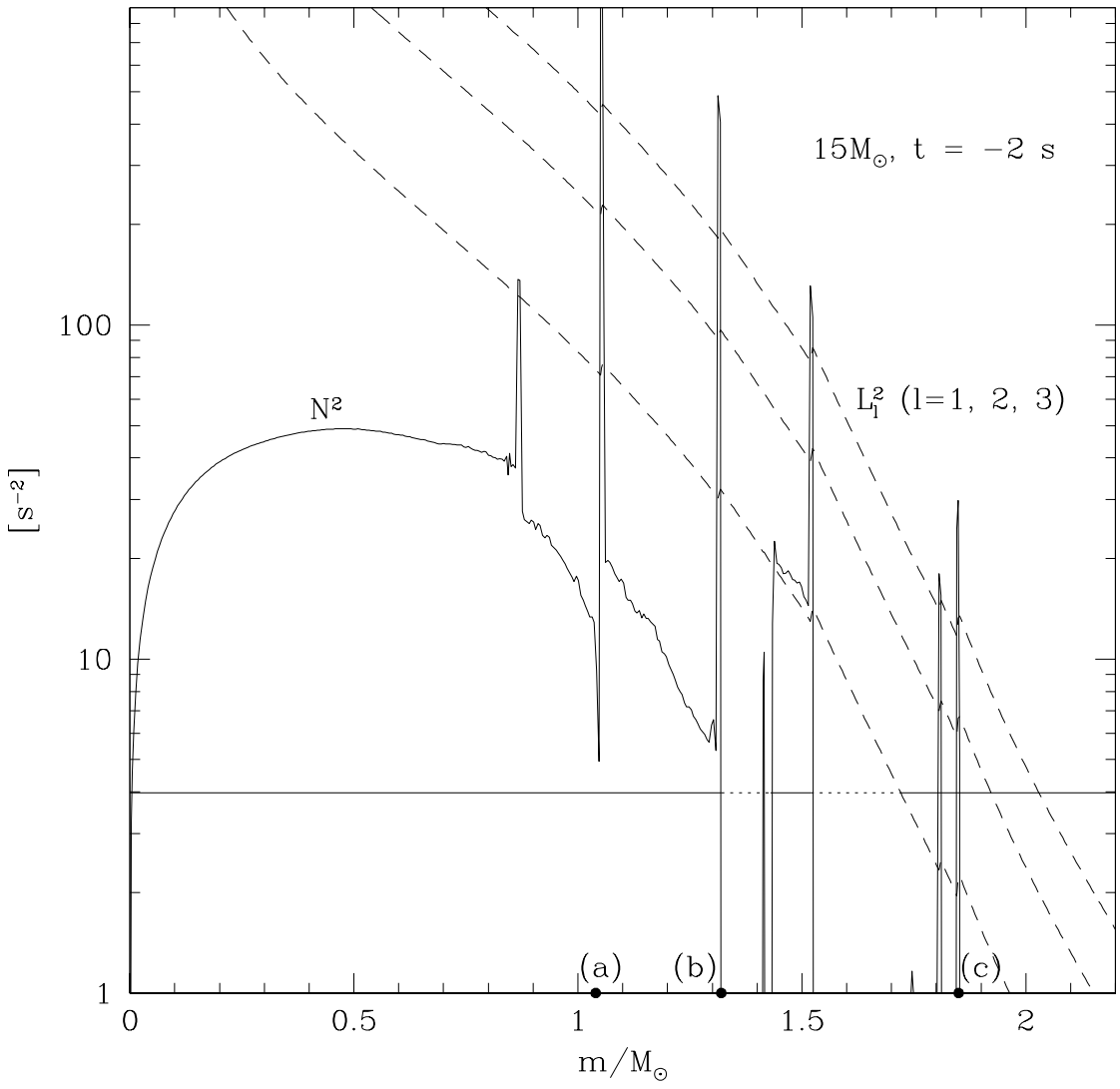

Figure 3.5: Propagation diagram for the $15M_\odot$ model at $t = -2$ s. The solid line is N^2 and the dashed lines are L_ℓ^2 with $\ell = 1$, 2, and 3. The three structural boundaries (a), (b), and (c) are indicated on the mass axis.

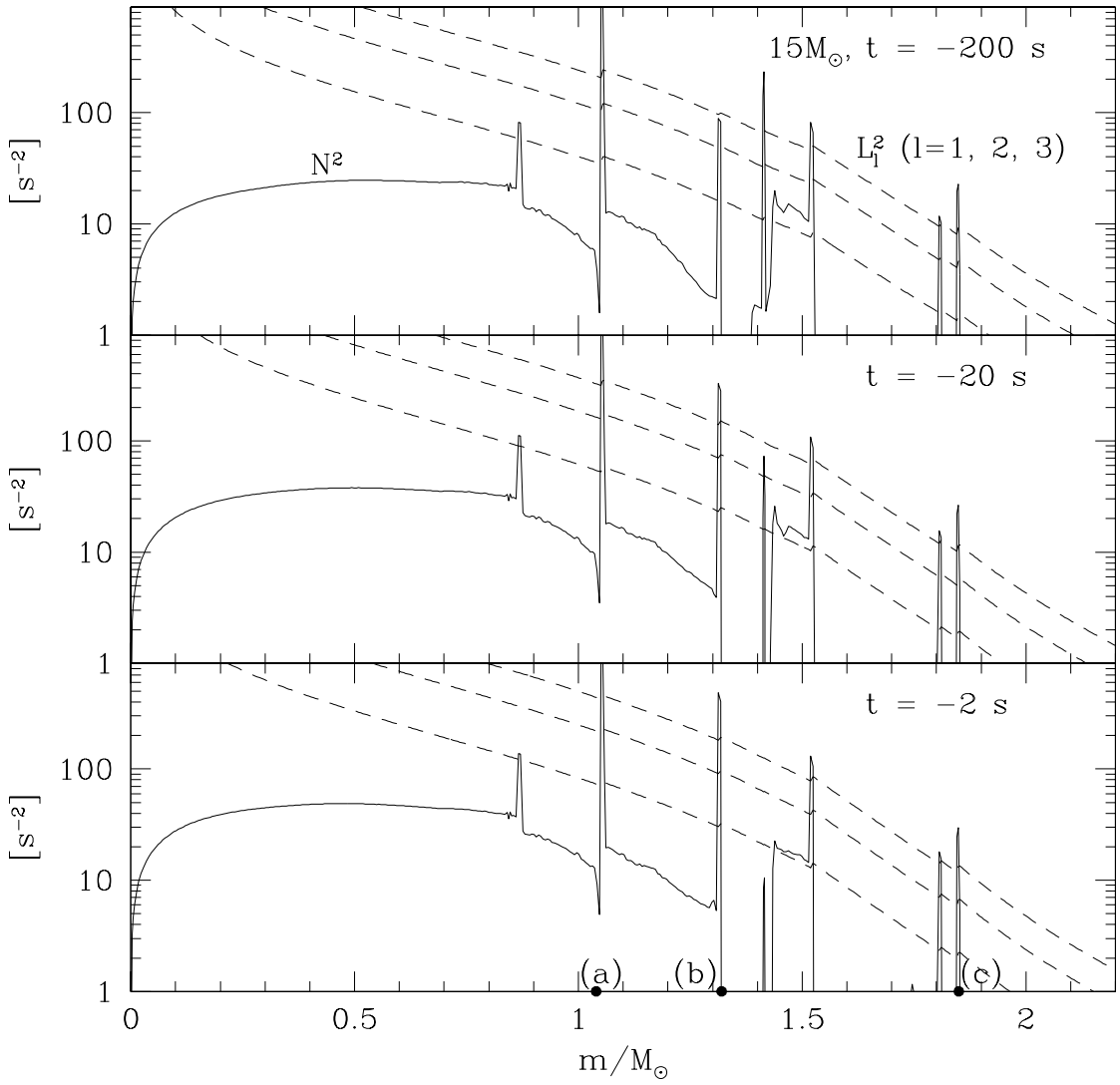

Figure 3.6: Propagation diagrams for the $15M_\odot$ model at $t = -200,\ -20,$ and 2 s (from top to bottom). The solid line is N^2 and the dashed lines are L_ℓ^2 with $\ell = 1$, 2, and 3. The three structural boundaries (a), (b), and (c) are indicated on the mass axis.

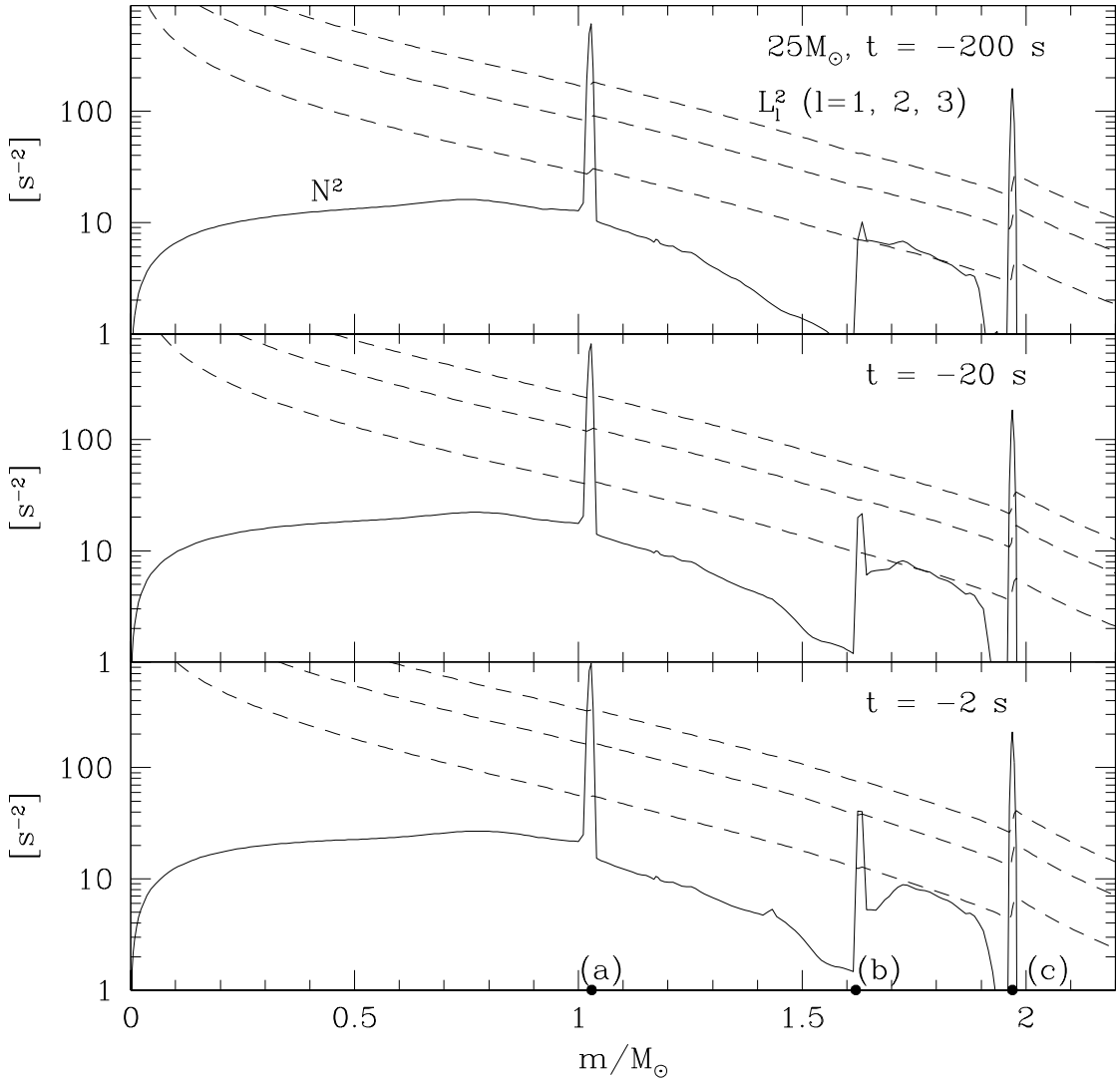

Figure 3.7: Similar to Fig. 3.6 but for the $25M_\odot$ model.

are defined by

$$L_\ell^2 = \frac{\ell(\ell+1)c_{\rm s}^2}{r^2}, \tag{3.2}$$

$$N^2 = g^2\left(\frac{1}{c_{\rm eq}^2} - \frac{1}{c_{\rm s}^2}\right), \tag{3.3}$$

where r is the radius, $g(r) = Gm(r)/r^2$ is the gravitational acceleration, ℓ is a label of the spherical harmonics $Y_{\ell m}$, $c_{\rm eq}^2 \equiv dP/d\rho$, and $c_{\rm s}$ is the sound speed defined by $c_{\rm s}^2 \equiv (\partial P/\partial\rho)_{\rm ad}$. The dispersion relation implies that p-modes can propagate in the regions where $\sigma > L_\ell$ and $\sigma > N$, whereas g-modes can propagate in the regions where $\sigma < L_\ell$ and $\sigma < N$. No waves can propagate in other regions. Heger's presupernova star models give tabulated numerical values of the density ρ, temperature T, electron fraction Y_e, and other thermodynamical quantities. We evaluate the adiabatic index $\Gamma_1 = (\partial \ln P/\partial \ln \rho)_{\rm ad}$ using standard thermodynamical relations and obtain the sound speed through $c_{\rm s}^2 = \Gamma_1 P/\rho$. We calculate $c_{\rm eq}^2 = dP/d\rho$ by directly finite-differentiating the tabulated quantities.

We can get considerable insight into how a mode behaves in different regions of the star from the propagation diagram that plots the Lamb frequency and the Brunt-Väisälä frequency as functions of mass (Unno et al. 1989). Fig.3.5 shows the propagation diagram for the $15M_\odot$ model at $t = -2$ s. The three structural boundaries (a), (b), and (c) discussed above are indicated on the mass axis. We can see that there is a $N^2 > 0$ region corresponding to the Fe core that is surrounded by the $N^2 = 0$ region (except for the small mode trapping region in $1.42M_\odot - 1.53M_\odot$) corresponding to the convective Si and O burning shells. This indicates that the Fe core is a good cavity for g-modes. Consider, for example, a mode with $\sigma = 2$ s^{-1} represented by the horizontal solid line in Fig. 3.5. The mode behaves as a g-mode in the Fe core where $\sigma < L_\ell$ and $\sigma < N$ while it does not propagate just outside the core where $N < \sigma < L_\ell$. However, it behaves as a p-mode further outside the

core where $\sigma > L_\ell$ and $\sigma > N$. Therefore, the mode is not completely trapped as a g-mode in the core but leaks outside the core as a p-mode. This mode leakage acts as a mode damping effect and requires a proper treatment of the outer boundary conditions as we will discuss in § 3.3.2.

The propagation diagrams for the $15M_\odot$ model at three different time epochs ($t = -200$, -20, and -2 s) are given in Fig. 3.6. Similarly, the propagation diagrams for $25M_\odot$ model are given in Fig. 3.7. The three spikes in N^2 corresponding to the structural boundaries (a), (b), and (c) can be easily identified in Fig. 3.7.

3.3 Linear Perturbation Equations, Boundary Conditions, and Mode Growth/Damping Rate

3.3.1 Linear Perturbation Equations

We consider adiabatic perturbations of a non-rotating star. The fluid equations are

$$\frac{\partial \rho}{\partial t} + \nabla \cdot (\rho \mathbf{v}) = 0, \tag{3.4}$$

$$\rho \left(\frac{\partial}{\partial t} + \mathbf{v} \cdot \nabla \right) \mathbf{v} = \nabla P - \rho \nabla \Phi, \tag{3.5}$$

$$\nabla^2 \Phi = 4\pi G \rho, \tag{3.6}$$

where ρ is the density, $\mathbf{v}$ is the velocity, P is the pressure, and Φ is the gravitational potential.

For an unperturbed quantity $Q_0(\mathbf{x})$, the perturbed quantity $Q(\mathbf{x}, t)$ is given by

$$Q(\mathbf{x}, t) = Q_0(\mathbf{x}) + \delta Q(\mathbf{x}, t), \tag{3.7}$$

where δQ is the Eulerian perturbation and

$$\mathbf{x}(t) = \mathbf{x}_0 + \boldsymbol{\xi}(\mathbf{x}, t), \tag{3.8}$$

where $\boldsymbol{\xi}$ is the Lagrangian displacement. We write the time dependence of the perturbations in the following manner

$$\boldsymbol{\xi}(\mathbf{x},t) = e^{-i\sigma t}\boldsymbol{\xi}(\mathbf{x}), \tag{3.9}$$

$$\delta\rho(\mathbf{x},t) = e^{-i\sigma t}\delta\rho(\mathbf{x}), \tag{3.10}$$

$$\delta P(\mathbf{x},t) = e^{-i\sigma t}\delta P(\mathbf{x}), \tag{3.11}$$

$$\delta\Phi(\mathbf{x},t) = e^{-i\sigma t}\delta\Phi(\mathbf{x}), \tag{3.12}$$

where σ is the complex mode frequency $\sigma = \sigma_{\rm R} + i\sigma_{\rm I}$. The negative sign in the exponent $e^{-i\sigma t}$ is chosen so that a positive (negative) $\sigma_{\rm I}$ corresponds to mode growth (damping): $e^{-i\sigma t} = e^{-i\sigma_{\rm R} t}\cdot e^{\sigma_{\rm I} t}$.

Then the linear perturbations to Eqs. (3.4) – (3.6) yield

$$\delta\rho = -\nabla\cdot(\rho\xi), \tag{3.13}$$

$$-\sigma^2\boldsymbol{\xi} - \frac{\delta\rho}{\rho^2}\nabla P + \frac{1}{\rho}\nabla\delta P + \nabla\delta\Phi = 0, \tag{3.14}$$

$$\nabla^2\delta\Phi = 4\pi G\delta\rho. \tag{3.15}$$

We decompose $\boldsymbol{\xi}(\mathbf{x})$ and ∇ into radial and tangential components as

$$\boldsymbol{\xi}(\mathbf{x}) = \xi_r(\mathbf{x})\hat{r} + \boldsymbol{\xi}_\perp(\mathbf{x}), \tag{3.16}$$

$$\begin{aligned}\nabla &= \hat{r}\frac{\partial}{\partial r} + \hat{\theta}\frac{1}{r}\frac{\partial}{\partial\theta} + \hat{\varphi}\frac{1}{r\sin\theta}\frac{\partial}{\partial\varphi} \\ &\equiv \hat{r}\frac{\partial}{\partial r} + \nabla_\perp.\end{aligned} \tag{3.17}$$

We further write the angular dependence of ξ_r, $\delta\rho$, δP, and $\delta\Phi$ in the following

manner

$$\xi_r(\mathbf{x}) = \xi_r(r)Y_{\ell m}(\theta,\varphi), \tag{3.18}$$

$$\delta\rho(\mathbf{x}) = \delta\rho(r)Y_{\ell m}(\theta,\varphi), \tag{3.19}$$

$$\delta P(\mathbf{x}) = \delta P(r)Y_{\ell m}(\theta,\varphi), \tag{3.20}$$

$$\delta\Phi(\mathbf{x}) = \delta\Phi(r)Y_{\ell m}(\theta,\varphi), \tag{3.21}$$

where $Y_{\ell m}$ is the spherical harmonics given by

$$Y_{\ell m}(\theta,\phi) = (-1)^{(m+|m|)/2}\left[\frac{2\ell+1}{2\pi}\frac{(\ell-|m|)!}{(\ell+|m|)!}\right]^{1/2} P_\ell^{|m|}(\cos\theta)e^{im\varphi}. \tag{3.22}$$

Then Eqs. (3.13) – (3.15) yield

$$\frac{d}{dr}(r^2\xi_r) = \frac{g}{c_{\rm s}^2}(r^2\xi_r) + \frac{r^2}{c_{\rm s}^2}\left(\frac{L_\ell^2}{\sigma^2}-1\right)\left(\frac{\delta P}{\rho}\right) + \frac{\ell(\ell+1)}{\sigma^2}\delta\Phi, \tag{3.23}$$

$$\frac{d}{dr}\left(\frac{\delta P}{\rho}\right) = \frac{\sigma^2-N^2}{r^2}(r^2\xi_r) + \frac{N^2}{g}\left(\frac{\delta P}{\rho}\right) - \frac{d}{dr}\delta\Phi, \tag{3.24}$$

$$\frac{1}{r^2}\frac{d}{dr}\left(r^2\frac{d}{dr}\delta\Phi\right) - \frac{\ell(\ell+1)}{r^2}\delta\Phi = 4\pi G\delta\rho. \tag{3.25}$$

We assume that the Eulerian perturbation of the gravitational potential is negligible (i.e., $\delta\Phi = 0$; the Cowling approximation) in the star. Then Eqs. (3.23) – (3.25) reduce to the following two equations.

$$\frac{d}{dr}(r^2\xi_r) = \frac{g}{c_{\rm s}^2}(r^2\xi_r) + \frac{r^2}{c_{\rm s}^2}\left(\frac{L_\ell^2}{\sigma^2}-1\right)\left(\frac{\delta P}{\rho}\right), \tag{3.26}$$

$$\frac{d}{dr}\left(\frac{\delta P}{\rho}\right) = \frac{\sigma^2-N^2}{r^2}(r^2\xi_r) + \frac{N^2}{g}\left(\frac{\delta P}{\rho}\right). \tag{3.27}$$

We solve these equations as an eigenvalue problem with complex eigenvalue σ^2 with appropriate boundary conditions (e.g., mode leakage). The real part $\sigma_{\rm R}$ of the mode frequency σ gives the oscillation frequency whereas the imaginary part $\sigma_{\rm I}$ gives the mode damping rate due to mode leakage.

3.3.2 Boundary Conditions

We discuss the boundary conditions for Eqs. (3.26) and (3.27). One of the inner boundary conditions comes from the regularity of the solution at the center of the star. It requires that (see Unno et al. 1989)

$$(r^2\xi_r) = \frac{\ell r}{\sigma^2}\left(\frac{\delta P}{\rho}\right). \tag{3.28}$$

Another condition imposed at the center of the star is the normalization condition

$$(r^2\xi_r) = 1. \tag{3.29}$$

As mentioned before, the g-modes are not completely trapped in the core. To take into account this mode leakage, we adopt the following outer boundary condition. We choose $r_{\rm out}$ to be sufficiently large so that a g-mode propagates as a p-mode at $r_{\rm out}$. The boundary condition is such that only an outgoing wave exists. Assuming that the mode functions are of the form $(r^2\xi_r,\, \delta P/\rho) \sim \exp(\int^r \kappa dr)$ with κ a complex wave number and substituting into Eqs. (3.26) and (3.27), we get

$$\left(\frac{g}{c_{\rm s}^2} - \kappa\right)(r^2\xi_r) + \frac{r^2}{c_{\rm s}^2}\left(\frac{L_\ell^2}{\sigma^2} - 1\right)\left(\frac{\delta P}{\rho}\right) = 0, \tag{3.30}$$

$$\frac{\sigma^2}{r^2}(r^2\xi_r) - \kappa\left(\frac{\delta P}{\rho}\right) = 0, \tag{3.31}$$

where we have used $N^2 = 0$ at $r = r_{\rm out}$. Thus we have

$$\kappa_\pm = \frac{g}{2c_{\rm s}^2} \pm i\frac{1}{c_{\rm s}}\left(\sigma_{\rm R}^2 - L_\ell^2 - \frac{g^2}{4c_{\rm s}^2}\right)^{1/2}, \tag{3.32}$$

where we have set $\sigma^2 \simeq \sigma_{\rm R}^2$ and have assumed that $\sigma_{\rm R}^2 > L_\ell^2 + g^2/(4c_{\rm s}^2)$. Since we choose the time dependence to be $e^{-i\sigma t} = e^{-i\sigma_{\rm R} t}\cdot e^{\sigma_{\rm I} t}$ we should keep only κ_+ for an outgoing wave. The boundary condition at $r_{\rm out}$ is then given by

$$\frac{\sigma^2}{r^2}(r^2\xi_r) = \kappa_+\left(\frac{\delta P}{\rho}\right). \tag{3.33}$$

Note that the existence of the real part $g/(2c_{\rm s}^2)$ in κ_+ gives $|\xi|^2 \sim \exp(\int dr\, g/c_{\rm s}^2) = \exp(-\int d\rho/\rho)$. However, this does not imply mode divergence since the energy density of the mode is $\sim r^2\rho|\xi|^2 =$ constant. Eqs. (3.26), (3.27), and the above boundary conditions [Eqs. (3.28), (3.29), (3.32), and (3.33)] completely determine the unknown complex eigenvalue σ^2 and eigenfunctions. In order to solve the eigenvalue problem numerically, we use the shooting method combined with the Newton-Raphson method (see Press et al. 1992).

3.3.3 Mode Growth/Damping Rate

We obtain the total mode growth/damping rate taking into account all the mode growth/damping effects. There are mode damping due to mode leakage and mode growth/damping due to the ε-mechanism (mode growth from nuclear energy generation and mode damping due to neutrino energy loss). The mode damping rate due to mode leakage is given by the imaginary part of the mode frequency: $\sigma_{\rm leak} = \sigma_{\rm I}$ (< 0). The mode growth/damping rate due to the ε-mechanism is estimated by the quasi-adiabatic approximation. In the quasi-adiabatic approximation, the mode energy E and the work integral W, which is defined as the increase of the mode energy per unit time, are calculated using the mode functions and the mode frequency obtained in the adiabatic calculation. From the equipartition theorem, the total energy of a mode is twice its kinetic energy. Taking the average over one period, it is calculated as

$$\begin{aligned} E &= \oint dt \int dm\, \mathbf{v}(\mathbf{x},t)^2 / \oint dt \\ &= \frac{1}{2}\sigma_{\rm R}^2 \int_0^M dm\, \boldsymbol{\xi}(\mathbf{x}) \cdot \boldsymbol{\xi}^*(\mathbf{x}) \\ &= \frac{1}{2}\sigma_{\rm R}^2 \int_0^R \rho[|\xi_r(r)|^2 + \ell(\ell+1)|\xi_\perp(r)|^2] r^2 dr. \end{aligned} \tag{3.34}$$

Similarly, taking the average over one period, the work integral is calculated as

$$\begin{aligned} W &= \oint dt \int_0^M dm\, \Delta T(\mathbf{x},t) \frac{d\Delta S(\mathbf{x},t)}{dt} / \oint dt \\ &= \oint dt \int_0^M dm \frac{\Delta T}{T}(\mathbf{x},t) \Delta\varepsilon(\mathbf{x},t) / \oint dt \\ &= \frac{1}{2} \int_0^M dm \frac{\Delta T^*}{T}(\mathbf{x}) \Delta\varepsilon(\mathbf{x}). \end{aligned} \tag{3.35}$$

Let us write $\varepsilon = \varepsilon_0 T^\alpha \rho^\beta$. Then we get

$$\frac{\Delta\varepsilon}{\varepsilon} = \left(\alpha + \frac{\beta}{\Gamma_3 - 1}\right) \frac{\Delta T}{T}, \tag{3.36}$$

where $\Gamma_3 - 1 = (\partial \ln T / \partial \ln \rho)_{\rm ad}$. Using this, we get

$$W = \frac{1}{2} \int_0^M dm \left| \frac{\Delta T}{T}(\mathbf{x}) \right|^2 \left(\alpha + \frac{\beta}{\Gamma_3 - 1}\right) \varepsilon. \tag{3.37}$$

We also have

$$\frac{\Delta T}{T} = \frac{\Delta P}{P} \nabla_{\rm ad} = \frac{1}{P} (\delta P - \rho g \xi_r) \nabla_{\rm ad}, \tag{3.38}$$

where $\nabla_{\rm ad} = (\partial \ln T / \partial \ln P)_{\rm ad}$. Using this, we finally get

$$W = \int_0^M dm \left| \frac{\delta P(\mathrm{x})}{P} - \frac{\rho g \xi_r(\mathrm{x})}{P} \right|^2 \left(\alpha + \frac{\beta}{\Gamma_3 - 1}\right) \nabla_{\rm ad}^2\, \varepsilon \tag{3.39}$$

Both the nuclear energy generation rate $\varepsilon_{\rm nuc}$ and neutrino energy loss rate ε_ν are included in ε:

$$\varepsilon = \varepsilon_{\rm nuc} + \varepsilon_\nu. \tag{3.40}$$

Using E and W, the mode growth/damping rate due to the ε-mechanism is calculated as

$$\sigma_\varepsilon = \frac{W}{2E}, \tag{3.41}$$

where the factor "2" in the denominator comes from the fact that the mode energy depends on the square of the mode amplitude. The total mode growth/damping rate is then given by

$$\sigma_{\rm tot} = \sigma_{\rm leak} + \sigma_{\varepsilon}. \tag{3.42}$$

The e-folding time for the total mode growth/damping is then given by

$$\tau = \frac{1}{\sigma_{\rm tot}}. \tag{3.43}$$

A positive (negative) e-folding time for mode growth/damping means a growing (damping) mode in our conventions.

3.4 Numerical Results

In this section we summarize the results of our numerical analysis. In Tables 3.1 and 3.2, the obtained mode frequencies and growth/damping rates are tabulated for the $15M_{\odot}$ and $25M_{\odot}$ models, respectively. For each model at each time epoch, we computed modes for different values of ℓ. We are most interested in the perturbations with small ℓ, especially $\ell = 1$, since they geometrically lead to asymmetric supernova explosions most effectively. The order of a mode was identified by counting the number of nodes in the mode function. Higher order modes have lower oscillation frequencies.

We have found that most of the modes are damping modes although there are some growing modes for $t = -2$ s for which mode growth due to the ε-mechanism in the Si burning shell is larger than that for the prior times $t = -20$ s and 200 s. The fact that most of the modes are damping modes can be understood by seeing where the ε-mechanisms (mode growth by nuclear energy generation and mode

damping by neutrino energy loss) are at work. We decompose the integrand of W given in Eq. (3.39) in the following manner.

$$W = \int dm\, f_{\rm mode}\, \hat{\varepsilon}, \tag{3.44}$$

$$f_{\rm mode} \equiv \left| \frac{\delta P({\rm x})}{P} - \frac{\rho g \xi_r({\rm x})}{P} \right|^2, \tag{3.45}$$

$$\hat{\varepsilon} \equiv \left(\alpha + \frac{\beta}{\gamma_3 - 1} \right) \nabla_{\rm ad}^2\, \varepsilon. \tag{3.46}$$

In Fig. 3.8, we plot ε, $\hat{\varepsilon}$, and $f_{\rm mode}$ of the three lowest order $\ell = 1$, 2 modes for the $15M_\odot$ model at $t = -2$ sec. We can see that the modes are mostly concentrated inside the core where $\hat{\varepsilon}$ is negative due to the neutrino energy loss and their amplitudes are small in the Si burning shell where $\hat{\varepsilon}$ takes large positive values. This indicates that the modes tend to be damping modes.

The most important finding is that, even if a mode is a growing mode, the e-folding time of mode growth is much longer than the remaining time before the core collapse. The long e-folding time of mode growth due to the ε-mechanism in the Si burning shell can be explained analytically to some extent. We assume that the work integral W can be approximately evaluated by the contribution from the mass interval ΔM where $\hat{\varepsilon}$ has the largest peak. We also obtain a lower limit of the mode energy E by only including the contribution from the same mass interval ΔM. Note that since mode energy is concentrated in the core, the actual E is much larger than this lower limit. We get

$$\begin{aligned} \tau &\gg \frac{\sigma_{\rm R}^2 \xi_r^2}{(\rho g \xi_r / P)^2 \hat{\varepsilon} \Delta M} \\ &= \left(\frac{P}{\rho g} \right)^2 \frac{\sigma_{\rm R}^2}{\hat{\varepsilon}} \simeq 5 \text{ sec}, \end{aligned} \tag{3.47}$$

where in the last step we used $\sigma_{\rm R} \simeq 3$ sec^{-1} and the values at $M \simeq 1.45 M_\odot$ ($\rho \simeq 1 \times 10^7$ g cm^{-3}, $P \simeq 3 \times 10^{24}$ g cm^{-1} s^{-2}, $g \simeq 5 \times 10^9$ cm s^{-2}, and $\hat{\varepsilon}_{\rm tot} \simeq$

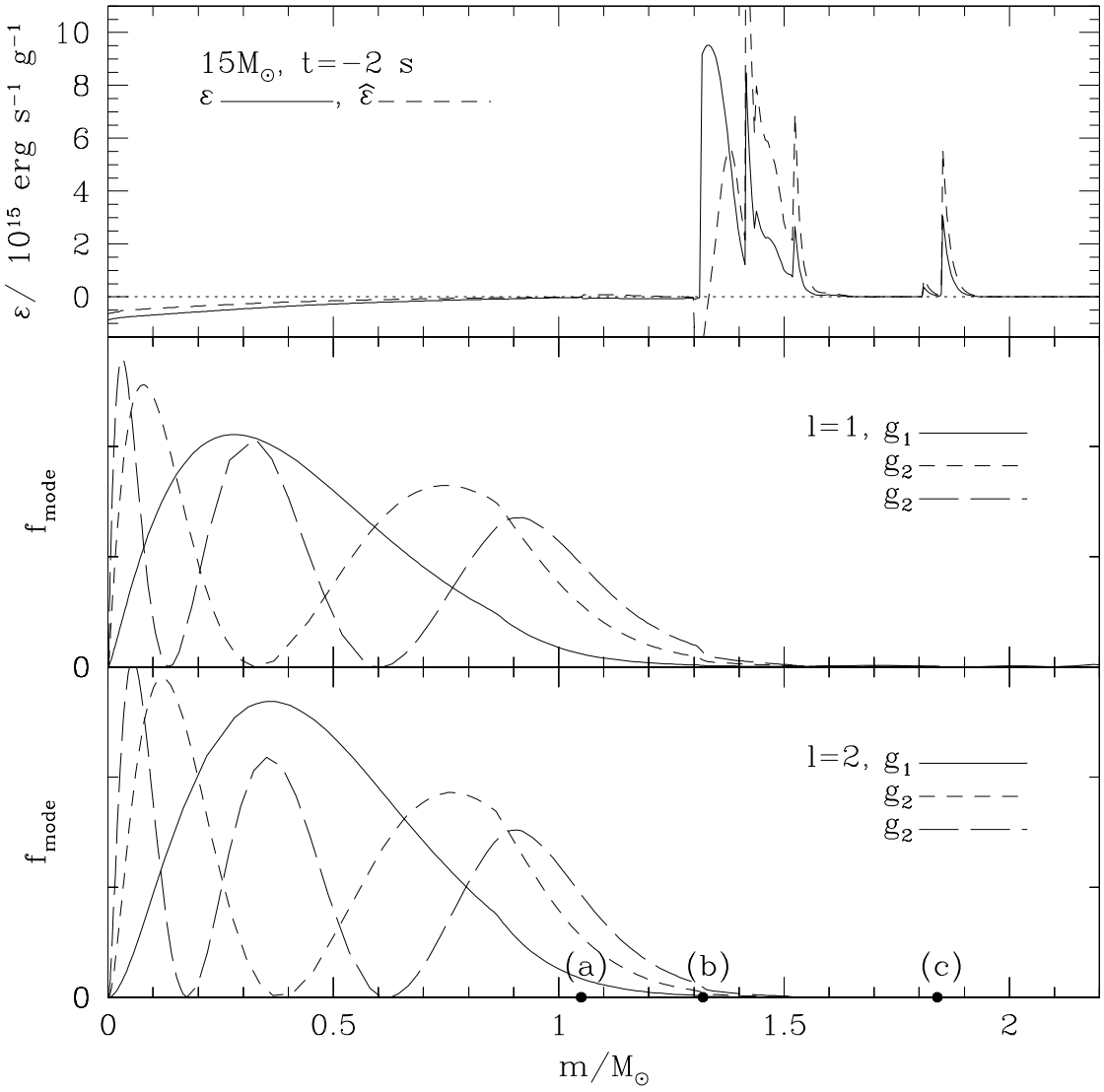

Figure 3.8: The top panel shows the total energy generation rate ε (solid line) and the quantity $\hat{\varepsilon}$ (dashed line) defined in Eq. (3.46) for the $15M_\odot$ model at $t = -2$ sec. The next two panels show $f_{\rm mode}$ (defined in the text) of the lowest order modes (g_1, g_2, and g_3) for $\ell = 1$ and $\ell = 2$, respectively. The three structural boundaries (a), (b), and (c) are indicated on the mass axis.

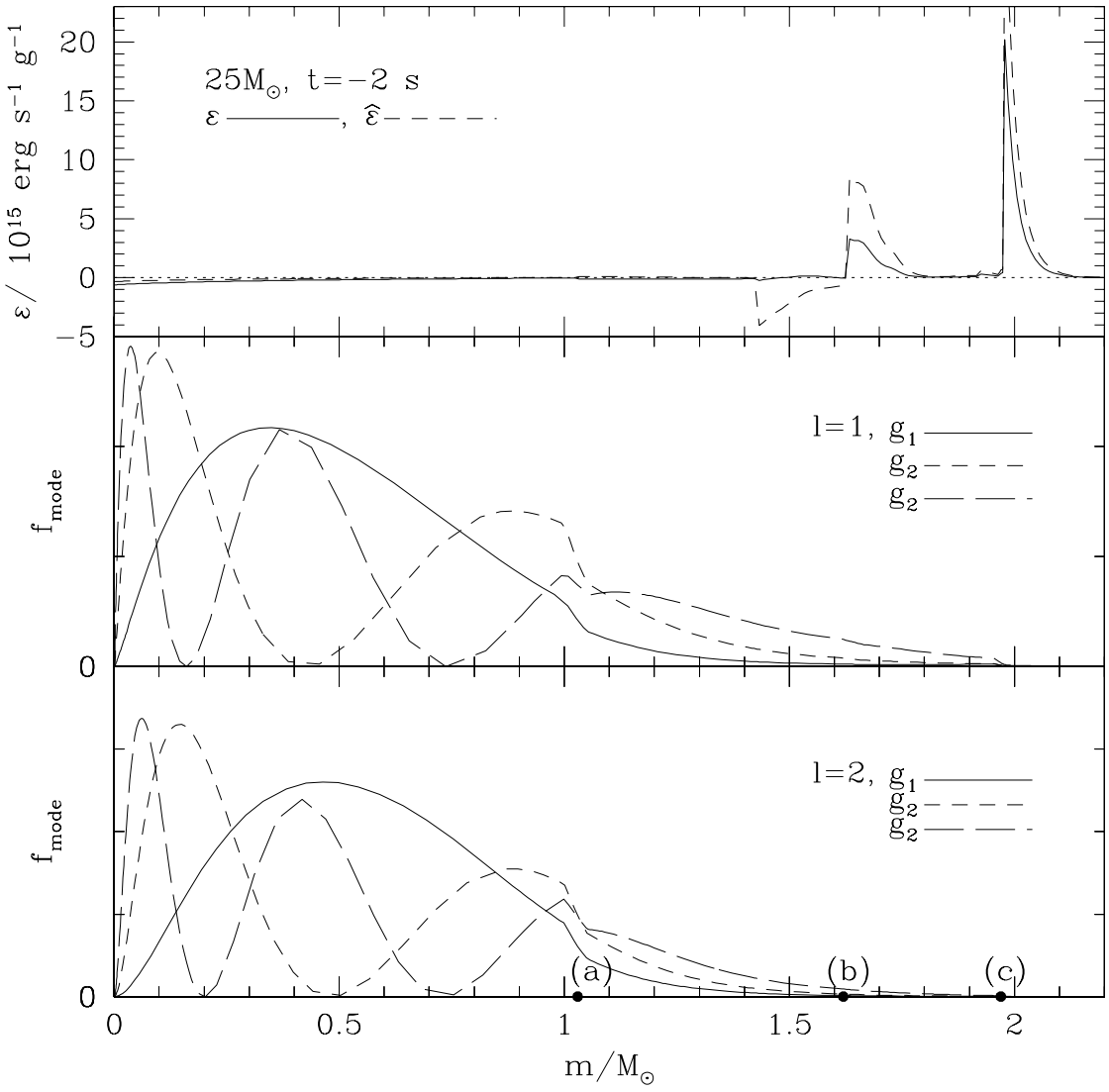

Figure 3.9: Similar to Fig. 3.8 but for the $25M_{\odot}$ model.

Table 3.1: Core g-modes for the $15M_\odot$ model

mode	$\sigma_{\rm R}$ [s^{-1}]	$\sigma_{\rm I} = \sigma_{\rm leak}$ [s^{-1}]	σ_ε [s^{-1}]	τ [s]
$t = -200$ s, $\ell = 1$				
g_1	2.84	-6.55×10^{-2}	-7.03×10^{-4}	-15.1
g_2	1.89	-1.42×10^{-2}	-8.70×10^{-4}	-66.4
g_3	1.39	-5.12×10^{-3}	-8.65×10^{-4}	-167
g_4	1.09	-4.09×10^{-3}	-7.90×10^{-4}	-205
g_5	0.901	-5.29×10^{-3}	-5.92×10^{-4}	-170
g_6	0.765	-7.42×10^{-3}	-4.16×10^{-4}	-128
$t = -20$ s, $\ell = 1$				
g_1	3.57	-7.51×10^{-2}	-2.73×10^{-3}	-12.8
g_2	2.36	-4.17×10^{-2}	-2.88×10^{-3}	-22.4
g_3	1.74	-1.24×10^{-2}	-2.63×10^{-3}	-66.7
g_4	1.38	-7.68×10^{-3}	-1.95×10^{-3}	-104
g_5	1.14	-7.89×10^{-3}	-9.91×10^{-4}	-113
g_6	0.969	-1.02×10^{-2}	1.69×10^{-6}	-97.8
$t = -2$ s, $\ell = 1$				
g_1	4.06	-1.11×10^{-1}	-7.01×10^{-3}	-8.44
g_2	2.70	-3.60×10^{-2}	-6.60×10^{-3}	-23.5
g_3	2.00	-1.43×10^{-2}	-5.10×10^{-3}	-51.6
g_4	1.59	-8.32×10^{-3}	2.38×10^{-3}	-168
g_5	1.33	-1.04×10^{-2}	2.59×10^{-2}	64.4
g_6	1.17	-1.17×10^{-2}	5.29×10^{-2}	24.3
$t = -2$ s, $\ell = 2$				
g_1	5.20	-8.40×10^{-3}	-7.76×10^{-3}	-61.9
g_2	3.77	-3.43×10^{-3}	-7.92×10^{-3}	-88.1
g_3	2.93	-2.05×10^{-3}	-6.95×10^{-3}	-111
g_4	2.39	-1.14×10^{-3}	-4.37×10^{-3}	-181
g_5	2.03	-1.02×10^{-3}	5.86×10^{-3}	207
g_6	1.78	-1.69×10^{-3}	4.20×10^{-2}	24.8

Table 3.2: Core g-modes for the $25M_\odot$ model

mode	$\sigma_{\rm R}$ [s^{-1}]	$\sigma_{\rm I} = \sigma_{\rm leak}$ [s^{-1}]	σ_ε [s^{-1}]	τ [s]
$t = -200$ s, $\ell = 1$				
g_1	2.21	-6.42×10^{-2}	-4.64×10^{-4}	-15.5
g_2	1.48	-2.49×10^{-2}	-7.41×10^{-4}	-38.9
g_3	1.09	-3.99×10^{-2}	-5.44×10^{-4}	-24.7
g_4	0.912	-5.79×10^{-2}	5.45×10^{-4}	-17.4
g_5	0.768	-3.93×10^{-2}	3.46×10^{-5}	-25.5
$t = -20$ s, $\ell = 1$				
g_1	2.59	-8.25×10^{-2}	-9.84×10^{-4}	-12.0
g_2	1.77	-2.25×10^{-2}	-1.43×10^{-3}	-41.8
g_3	1.30	-2.53×10^{-2}	-5.96×10^{-4}	-38.9
g_4	1.07	-3.95×10^{-2}	2.27×10^{-3}	-26.8
g_5	0.914	-2.26×10^{-2}	7.75×10^{-4}	-45.7
g_6	0.770	-2.20×10^{-2}	-1.38×10^{-4}	-45.2
$t = -2$ s, $\ell = 1$				
g_1	2.89	-8.13×10^{-2}	-2.09×10^{-3}	-12.0
g_2	1.96	-1.95×10^{-2}	-3.41×10^{-3}	-43.6
g_3	1.44	-1.83×10^{-2}	2.48×10^{-4}	-55.3
g_4	1.19	-3.56×10^{-2}	2.10×10^{-2}	-68.2
g_5	1.02	-1.98×10^{-2}	1.54×10^{-2}	-230
g_6	0.865	-1.02×10^{-2}	4.94×10^{-3}	-189
$t = -2$ s, $\ell = 2$				
g_1	3.70	-6.64×10^{-3}	-2.99×10^{-3}	-104
g_2	2.70	-1.78×10^{-3}	-4.71×10^{-3}	-154
g_3	2.06	-1.22×10^{-3}	-4.68×10^{-3}	-170
g_4	1.70	-3.00×10^{-3}	1.68×10^{-3}	-754
g_5	1.50	-5.28×10^{-3}	1.92×10^{-2}	72.1
g_6	1.33	-2.90×10^{-3}	1.38×10^{-2}	91.9

7×10^{15} erg g^{-1} s^{-1}) for the $15M_\odot$ model at $t = -2$ s. The oscillation frequency can be in principle obtained using the quantization condition in the WKB analysis. The quantization condition is given by $\int k_r dr = n\pi$ where the integration is over the g-mode resonant cavity (Unno et al. 1989). Using Eq. (3.1), this is rewritten as

$$\sigma_{\rm R} = \frac{[\ell(\ell+1)]^{1/2}}{n\pi} \int_{\rm cavity} \frac{N}{r} dr. \tag{3.48}$$

This gives values slightly larger but close to the ones obtained by numerical calculations.

We can see other trends in the numerical results given in Tables 3.1 and 3.2. First of all, the oscillation frequencies are higher for the $25M_\odot$ model than that for the $15M_\odot$ model. This is due to the higher Brunt-Väisälä frequency for the larger core. Similarly, for the same model, the oscillation frequencies are higher for later times than earlier times since more evolved cores tend to have higher Brunt-Väisälä frequencies. For different ℓ's, larger ℓ's tend to give greater oscillation frequencies. This can be understood by Eq. (3.48). The coupling between the core g-modes to the outgoing p-modes are smaller for larger ℓ's since the no-propagation region is wider for larger ℓ's.

3.5 Discussion and Conclusions

We performed a linear analysis of oscillation modes of the presupernova cores. We found that most of the modes are damping modes while there are some growing modes. Most importantly, we found that the e-folding time for mode growth is much longer than the remaining time until the onset of the core collapse. We thus conclude that the g-modes of a presupernova core cannot provide global asymmet-

ric perturbations that lead to an asymmetric supernova explosion / neutron star kick.

However, there may be other ways to provide global asymmetric perturbations in a presupernova core. In fact, our understanding of the final stage of a presupernova star evolution is still incomplete. Of particular concern is the treatment of convection in the burning region. The sound travel time, the convective turnover time, and the nuclear burning time are all of the same order of magnitude. The convective eddy speed can be significant fraction ($\simeq 1/4$) of the sound speed. Thus the mixing-length prescription may be problematic (Bazan & Arnett 1994). Therefore, at present, a complete picture of global asymmetries in presupernova stars is probably out of reach. However, the strongly convective Si burning shell implies that the Fe core may be not exactly spherically symmetric. This may give the necessary global asymmetric perturbations in a presupernova core that will be amplified during the core collapse and give rise to an asymmetric supernova explosion / neutron star kick.

Chapter 4

Thermal Evolution and Nucleosynthesis of Young Neutron Stars

4.1 Introduction

Neutron stars are created in the core collapse and subsequent supernova explosion of massive stars. Neutron stars are born extremely hot with their interior temperatures reaching $\sim 10^{11}$ K and they cool quickly by emitting neutrinos. In $\sim 10^3 - 10^4$ yrs, the interior temperatures of neuron stars drop to $\sim 10^8$ K, corresponding to the surface temperatures of $\sim 10^6$ K. At that time, photon emission takes over as the main cooling mechanism and the surface temperatures decrease gradually to $\sim 10^5$ K in the next $\sim 10^5 - 10^6$ yrs. Neutron stars can be observed as soft X-ray sources during this photon emission cooling phase.

Recent progress in X-ray observations has made it possible to study thermal radiation from neutron stars in detail. Thermal radiation from neutron star surfaces has been found in several radio pulsars (e.g., PSR B1055-52 and Geminga) and thermal radiation from neutron stars' hot spots has been found in a few other radio pulsars. Recent observations by *Chandra* has also revealed a number of compact central sources in supernova remnants with spectra consistent with thermal radiation from isolated neutron stars. In addition, several nearby, radio-quiet, isolated neutron stars have been discovered in the X-ray band in the *ROSAT* data and in the optical band. These radio-quiet, isolated neutron stars apparently have pure thermal radiation unlike the radio pulsars that also exhibit non-thermal radiation. Moreover, thermal radiation has been detected from the magneters that

have superstrong magnetic fields ($\gtrsim 10^{14}$ G).

Detailed theoretical models of neutron star atmospheres and spectra are needed in order to extract important information of neutron stars such as their surface chemical compositions, magnetic fields, effective surface temperatures, and gravitational redshifts from the observational data. There has been significant progress in this direction. Models of strongly magnetized neutron star atmospheres composed of hydrogen or helium have been constructed including all relevant physics (Ho & Lai 2001; Ho & Lai 2003; Ho et al. 2003). Atmospheres composed of mid-Z element (carbon, oxygen, or neon) have also been modeled (Mori & Ho 2006). In addition, radiation from non-gaseous, condensed surfaces composed of hydrogen or iron has been modeled (van Adelsberg et al. 2005). Comparison of the observational data and the theoretical models are currently underway (e.g., van Kerkwijk & Kaplan 2006).

Neutron star atmospheres are very important since they mediate the emergent radiation from neutron star surfaces to the observer. However, their chemical compositions are unknown and some chemical compositions are assumed in the atmosphere models mentioned above. Here, we want to find the innate chemical composition of a neutron star atmosphere. By the "innate" chemical composition, we mean that we will ignore its possible changes due to external effects such as accretion from the interstellar medium or from the binary companion. Our goal is to evolve the thermal structure and the chemical composition of a neutron star atmosphere from the earliest possible time. Early studies on the chemical compositions of neutron star atmospheres can be found in the works by Rosen and Rosen & Cameron, and more recently in the works by Chang & Bildsten and Chang, Arras, & Bildsten (Rosen 1968; 1969; Rosen & Cameron 1972; Chang & Bildsten 2002;

2004; Chang, Arras, & Bildsten 2004). However, these studies concern the evolutions at much later times assuming certain initial chemical compositions. In this chapter, we attempt to perform a nucleosynthesis calculation from a very early time when a neutron star atmosphere is hot enough that the nuclear statistical equilibrium composition can be used as the initial chemical composition.

The rest of the chapter is organized as follows. In § 4.2, we explain how we set up the problem. In § 4.3 – 4.7, we discuss several necessary components to solve the problem: static atmosphere models (§ 4.3), cooling of the bulk of a neutron star (§ 4.4), the nuclear statistical equilibrium composition (§ 4.5), nucleosynthesis calculations (§ 4.6), and the possible role of diffusion (§ 4.7). In § 4.8, we present discussion and conclusions.

4.2 Setup of the Problem

Our goal is to evolve the thermal structure and the chemical composition of a neutron star atmosphere from the earliest possible time, namely, when a neutron star is born.

A massive star ($\gtrsim 8M_\odot$) goes through successive stages of nuclear burning and eventually an iron core of mass $\simeq 1.5M_\odot$ is formed. Induced by photodissociation of iron-peak elements and electron captures by nuclei, the core starts to collapse due to its own gravity. The collapse of the inner core halts when the central density reaches about twice that of the atomic nucleus. The core rebounds and a shock wave is generated. The shock wave does not immediately give a supernova explosion but it stalls after losing its energy by disintegrating iron-peak elements in the outer core. Behind the stalled shock there is a competition between the infalling matter and the outgoing matter revived by neutrino heating. If the infalling matter

wins there will be no supernova explosion, instead a blackhole formation occurs. If the outgoing matter wins, there will be a successful supernova explosion and a neutron star formation. The physics behind the stalled shock is a complicated problem involving multi-dimensional numerical calculations of hydrodynamics and neutrino transports, possibly with the effects of the magnetic fields and rotation. According to these calculations the shock continues to stall for up to a second. When the stalled shock lifts off there is a significant amount of accretion onto the collapsed core but the accretion quickly settles. This is how a neutron star is born (see Prakash et al. 2001; Woosley & Janka 2005; Janka et al. 2006 for reviews).

A protoneutron star (i.e., newly-born neutron star) is a hot, lepton-rich, and bloated remnant of the core collapse. Due to its high temperature, a protoneutron star is opaque to neutrinos. It loses its leptons (deleptonization) and cools by neutrino diffusion (Burrows & Lattimer 1986). At the same time, it goes through gravitational contraction (the Kelvin-Helmholtz phase). The deleptonization and cooling continues for $\simeq$ 50 s until the neutron star becomes transparent to neutrinos. It is known that the intense neutrino fluxes from a cooling protoneutron star blows a "wind" from the protoneutron star surface (the protoneutron star wind; Salpeter & Shapiro 1981; Duncan, Shapiro, & Wasserman 1986; Thompson, Burrows, & Meyer 2001). The protoneutron winds typically last for $\sim$ 10 s. We are interested in a young neutron star atmosphere starting from the time when the protoneutron star wind has just ceased ($\sim$ 10 s after the core collapse).

We can separate the evolution of the atmosphere from that of the bulk of the neutron star. The bulk of the neutron star affects the atmosphere through providing the boundary conditions such as the base atmosphere temperature, and the luminosities and the mean energies of the neutrinos emitted from the bulk of

the neutron star. We evolve the thermal structure and chemical composition of a neutron star atmosphere in the following manner. For a given base atmosphere temperature, we construct a static atmosphere model. The atmosphere evolves together with the base atmosphere temperature. A nucleosynthesis calculation is performed in this cooling atmosphere.

There are several components involved in the problem: static atmosphere models for given base atmosphere temperatures, cooling of the bulk of a neutron star, the nuclear statistical equilibrium composition as an initial chemical composition, nucleosynthesis calculations in high temperatures, and the possible role of diffusion.

4.3 Static Atmosphere Models

We construct atmosphere models that are static both dynamically and thermally. We start with the general equations for a nonrelativistic fluid in a gravitational field. The equations for mass, momentum, and energy conservations are

$$\frac{\partial \rho}{\partial t} = -\nabla \cdot (\rho \mathbf{v}), \tag{4.1}$$

$$\frac{D\mathbf{v}}{Dt} = -\frac{1}{\rho}\nabla P - \nabla \phi, \tag{4.2}$$

$$\frac{Du}{Dt} + P\frac{D(1/\rho)}{Dt} = -\frac{1}{\rho}\nabla \cdot \mathbf{F} + \dot{q}, \tag{4.3}$$

where ρ is the density, $\mathbf{v}$ is the velocity, P is the pressure, u is the energy per unit mass, ϕ is the gravitational potential, $\mathbf{F}$ is the energy flux, and $\dot{q}$ is the energy generation rate per unit mass. The energy flux $\mathbf{F}$ should be obtained through the

energy transport equation. The auxiliary equations are

$$P = P(\rho,\ T,\ X_i), \tag{4.4}$$

$$u = u(\rho,\ T,\ X_i), \tag{4.5}$$

$$\dot{q} = \dot{q}(\rho,\ T,\ X_i), \tag{4.6}$$

where X_i is the mass fraction of the nuclei of species i. As we will see in § 4.6 and § 4.7 the mass fraction can change by nuclear reactions and diffusion.

For a spherical atmosphere in a central gravitational field of a neutron star of mass M, we have

$$\frac{D}{Dt} = \frac{\partial}{\partial t} + v\frac{\partial}{\partial r},\quad \nabla\phi = \frac{GM}{r^2},\quad \nabla\cdot(\rho\mathbf{v}) = \frac{1}{r^2}\frac{\partial}{\partial r}(r^2\rho v),\quad \nabla P = \frac{dP}{dr}, \tag{4.7}$$

where r is the radius and v is the radial component of $\mathbf{v}$. The flux divergence is given by

$$\nabla\cdot\mathbf{F} = \frac{1}{4\pi r^2}\frac{dL}{dr}, \tag{4.8}$$

where L is the luminosity

$$L = 4\pi r^2 F. \tag{4.9}$$

For a static atmosphere, Eqs. (4.1) – (4.3) reduce to the hydrostatic equation and the thermal balance equation

$$\frac{dP}{dr} = -\frac{GM}{r^2}, \tag{4.10}$$

$$-\frac{1}{4\pi\rho r^2}\frac{dL}{dr} + \dot{q} = 0. \tag{4.11}$$

We consider two cases in which the thermal balance [Eq. (4.11)] is achieved. In Case 1, we assume that the energy transport across the mass shells is negligible (i.e., dL/dr is ignored) compared to the energy generation in each mass shell. We then

construct a static atmosphere model under the condition that the thermal balance is achieved between the neutrino heating and cooling reactions that are relevant to the protoneutron star winds. In Case 2, we assume that the energy generation in each mass shell is negligible (i.e., $\dot{q}$ is ignored) compared to the energy transport across the mass shells. We then construct a static atmosphere model under the condition that the thermal balance is achieved between the photon and neutrino energy transports.

4.3.1 Case 1 (dL/dr Is Ignored): Thermal Balance Between Neutrino Heating and Cooling Reactions

We assume that neutrinos are emitted from the neutrinosphere of radius R_ν where matter becomes transparent to neutrinos. We adopt the neutrino heating and cooling rates given in Qian & Woosley (1996). The most important heating and cooling reactions in the protoneutron star winds are neutrino absorption by nucleons (heating) and electron and positron captures by nucleons (cooling)

$$\nu_e + n \rightleftharpoons p + e^-, \tag{4.12}$$

$$\bar{\nu}_e + p \rightleftharpoons n + e^+. \tag{4.13}$$

The specific heating rate due to neutrino absorption is

$$\begin{aligned} \dot{q}_{\nu N} &= \dot{q}_{\nu_e n} + \dot{q}_{\bar{\nu}_e p} \\ &\simeq 9.29 \times 10^{18} [X_n L_{\nu_e, 51} \varepsilon^2_{\nu_e, \mathrm{MeV}} + X_p L_{\bar{\nu}_e, 51} \varepsilon^2_{\bar{\nu}_e, \mathrm{MeV}}] \frac{1-x}{R^2_{\nu,6}} \ \mathrm{erg\,s^{-1}\,g^{-1}}, \end{aligned} \tag{4.14}$$

where $x = (1 - R^2_\nu/r^2)^{1/2}$ is a function of radius, $R_{\nu,6}$ is the neutrinosphere in 10^6 cm, $L_{\nu,51}$ is the neutrino luminosity in 10^{51} erg s^{-1}, and $\varepsilon_{\nu,\mathrm{MeV}}$ is an approximate neutrino energy in MeV defined as $\varepsilon^2_\nu \equiv \langle E^3_\nu \rangle / \langle E_\nu \rangle$. The specific cooling rate

due to electron and positron captures is given by

$$\dot{q}_{eN} = \dot{q}_{e^-p} + \dot{q}_{e^+n} \simeq 8.98 \times 10^{17} T_{10}^6 \text{ erg s}^{-1} \text{ g}^{-1}. \tag{4.15}$$

Another set of heating and cooling reactions are neutrino-antineutrino annihilation (heating) and electron-positron annihilation (cooling)

$$\nu + \bar{\nu} \rightleftharpoons e^- + e^+, \tag{4.16}$$

where neutrino-antineutrino pairs can be of any type. The specific heating rate due to neutrino-antineutrino annihilation is given by

$$\dot{q}_{\nu\bar{\nu}} \simeq 1.16 \times 10^{19} \left[L_{\nu_e,51} L_{\bar{\nu}_e,51} (\epsilon_{\nu_e,\text{MeV}} + \epsilon_{\bar{\nu}_e,\text{MeV}}) + \frac{6}{7} L^2_{\nu_\mu,51} \epsilon_{\nu_\mu,\text{MeV}} \right] \times \frac{\Phi(x)}{\rho_8 R^4_{\nu,6}} \text{ erg s}^{-1} \text{ g}^{-1}, \tag{4.17}$$

where $\Phi(x) = (1-x)^4(x^2+4x+5)$ is a geometric factor for neutrino-antineutrino encounters. On the other hand, the specific cooling rate due to electron-positron annihilation is given by

$$\dot{q}_{e^-e^+} \simeq 3.65 \times 10^{16} \frac{T_{10}^9}{\rho_8} \text{ erg s}^{-1} \text{ g}^{-1}. \tag{4.18}$$

In addition, there is heating due to scattering of neutrinos of all types off electrons and positrons. The specific heating rate due to these reactions is given by

$$\begin{aligned} \dot{q}_{e\nu} &= \dot{q}_{\nu_e e^-} + \dot{q}_{\nu_e e^+} + \dot{q}_{\bar{\nu}_e e^-} + \dot{q}_{\bar{\nu}_e e^+} + 2(\dot{q}_{\nu_\mu e^-} + \dot{q}_{\nu_\mu e^+} + \dot{q}_{\bar{\nu}_\mu e^-} + \dot{q}_{\bar{\nu}_\mu e^+}) \\ &\simeq 1.15 \times 10^{18} \frac{T_{10}^4}{\rho_8} \left(L_{\nu_e,51} \epsilon_{\nu_e,\text{MeV}} + L_{\bar{\nu}_e,51} \epsilon_{\bar{\nu}_e,\text{MeV}} + \frac{6}{7} L_{\nu_\mu,51} \epsilon_{\nu_\mu,\text{MeV}} \right) \\ &\quad \times \frac{1-x}{R^2_{\nu,6}} \text{ erg s}^{-1} \text{ g}^{-1}, \end{aligned} \tag{4.19}$$

where $\epsilon_{\nu,\text{MeV}}$ is $\epsilon_\nu \equiv \langle E_\nu^2 \rangle / \langle E_\nu \rangle$ in MeV.

We assume that the atmosphere is composed of nonrelativistic, nondegenerate nucleons (half protons and half neutrons, or $Y_e = 0.5$), and relativistic, arbitrarily

degenerate electron-positron pairs that are in thermal equilibrium with photons. Then we have

$$\begin{aligned} P &= P_N + P_e + P_\gamma \\ &= \frac{\rho kT}{m} + \frac{7\pi^2}{180}\left[1 + \frac{30}{7}\left(\frac{\eta_e}{\pi}\right)^2 + \frac{15}{7}\left(\frac{\eta_e}{\pi}\right)^4\right]\frac{(kT)^4}{(\hbar c)^3} + \frac{\pi^2}{45}\frac{(kT)^4}{(\hbar c)^3}, \end{aligned} \quad (4.20)$$

where m is the mean molecular mass currently set equal to the atomic mass unit m_u and η_e is the electron degeneracy parameter (see § 4.4). There is a relation between η_e and ρ (see § 4.4)

$$n_e = Y_e n_b = Y_e \frac{\rho}{m_u} = \frac{1}{\pi^2}\left(\frac{kT}{\hbar c}\right)^3\left(\frac{\eta_e^3}{3} + \frac{\pi^3\eta_e}{3}\right). \quad (4.21)$$

From Eqs. (4.10), (4.11), (4.20), and (4.21) we can calculate the temperature and density profiles in the thermal balance.

In order to do that, we need to know the neutrino fluxes and energies from the bulk of the protoneutron star as well as the neutrinosphere radius and the neutrinosphere temperature. These values are taken from a protoneutron star cooling calculation (e.g., Burrows & Lattimer 1986). For example, a set of values we have used is: $L_{\bar{\nu}_e,51} = 1.0$, $L_{\nu_e,51} \simeq L_{\bar{\nu}_e,51}/1.3$, $L_{\nu_\mu,51} \simeq L_{\bar{\nu}_e,51}/1.4$, $\epsilon_{\nu_e,\mathrm{MeV}} \simeq \varepsilon_{\nu_e,\mathrm{MeV}} \simeq 11.0\alpha$, $\epsilon_{\bar{\nu}_e,\mathrm{MeV}} \simeq \varepsilon_{\bar{\nu}_e,\mathrm{MeV}} \simeq 14.0\alpha$, $\epsilon_{\nu_\mu,\mathrm{MeV}} \simeq \varepsilon_{\nu_\mu,\mathrm{MeV}} \simeq 23.0\alpha$, where α is defined as

$$\alpha \equiv \left(\frac{L_{\bar{\nu}_e,51}}{8.0}\right)^{1/4}. \quad (4.22)$$

The corresponding neutrinosphere temperature $T(R_\nu)$ is estimated by the effective temperature assuming the blackbody neutrino emission

$$T(R_\nu) = \left[\frac{L_\nu}{4\pi R_\nu^2 (7\mathcal{N}_\nu/8)\sigma_{\mathrm{SB}}}\right]^{1/4} = 4.3 \times 10^{10}\ \mathrm{K}, \quad (4.23)$$

where $\mathcal{N}_\nu$ is the number of neutrino types. We choose the neutrinosphere radius to be $R_\nu = 10^6$ cm

We basically solve the following two equations at each radius for unknown density ρ and temperature T using the Newton-Raphson method (see Press et al. 1992).

$$P = P(\rho, T) \tag{4.24}$$

$$\dot{q}(\rho, T) = 0. \tag{4.25}$$

The base atmosphere temperature $T(R_\nu)$ is given [see Eq. (4.23)]. The hydrostatic equation, given in Eq. (4.10), is integrated outwardly to find the pressure P at the new radius.

So far, we have not found a static atmosphere solution under our assumptions. This might be due to the known inaccuracies of the neutrino heating rates near the neutrinosphere but our attempts of similar calculations with more elaborate neutrino rates given in Thompson, Burrows, & Meyer (2001) did not give a static atmosphere either. Another possibility is that this is due to the uncertainties in choosing the values of the neutrino luminosities and mean energies. We believe the issue requires further study.

4.3.2 Case 2 ($\dot{q}$ Is Ignored): Thermal Balance Between Photon and Neutrino Energy Transports

We want to construct a static atmosphere model in which the thermal balance is achieved between photon and neutrino energy transports. Then the thermal balance equation becomes

$$\frac{dL_\gamma}{dr} + \frac{dL_\nu}{dr} = 0. \tag{4.26}$$

We solve the hydrostatic equation and the thermal balance equation to obtain density and temperature profiles. The following argument essentially parallels the

static atmosphere models discussed in Duncan, Shapiro, & Wasserman (1986).

We assume that young neutron star atmospheres are optically thick to photons and optically thin to neutrinos. For the photon transport, we assume that the diffusion approximation, which is derived from the second moment of the photon transport equation, is valid. Then we have

$$\mathbf{F}_\gamma = -\frac{c}{3\kappa_\gamma \rho}\nabla U_\gamma, \tag{4.27}$$

where κ_γ is the Rosseland mean photon opacity and U_γ is the photon energy density which is given by the Planck energy density

$$U_\gamma = U_{\gamma,\,\mathrm{Planck}} = aT^4. \tag{4.28}$$

For the neutrino transport, we use the first moment of the neutrino transport equation integrated over frequencies

$$\nabla \cdot \mathbf{F}_\nu = c\kappa_\nu \rho (U_{\nu,\,\mathrm{Planck}} - U_\nu), \tag{4.29}$$

where κ_ν is the Rosseland mean neutrino opacity, $U_{\nu,\,\mathrm{Planck}}$ is the "Planck" neutrino energy density

$$U_{\nu,\,\mathrm{Planck}} \;=\; \frac{7\mathcal{N}_\nu}{8}(aT^4), \tag{4.30}$$

with $\mathcal{N}_\nu$ being the number of neutrino types, and U_ν is the actual neutrino energy density given by

$$U_\nu \;=\; \frac{7\mathcal{N}_\nu}{8}(aT_\nu^4). \tag{4.31}$$

Here T_ν is the neutrino temperature defined so that the neutrino energy density decreases in the inverse-square manner

$$T_\nu = T_{\nu 0}\left(\frac{R_\nu}{r}\right)^{1/2}, \tag{4.32}$$

where $T_{\nu 0} \equiv T_\nu(R_\nu) = T(R_\nu)$ is the temperature at the neutrinosphere.

We assume that the dominant source for photon opacity in the temperature range of our interest is photon scattering off free electrons. We use the Thomson scattering opacity

$$\kappa_\gamma = 0.40 Y_e \text{ cm}^2 \text{ g}^{-1}. \tag{4.33}$$

We also assume that the dominant neutrino opacity source is neutrino absorption by nuclei.

$$\nu_e + n \rightarrow p + e^-, \tag{4.34}$$

$$\bar{\nu}_e + p \rightarrow n + e^+. \tag{4.35}$$

For simplicity we treat the neutrino opacity as constant

$$\kappa_\nu = 2.6 \times 10^{-21} \left(\frac{T_{\nu 0}}{10^9 \text{ K}} \right)^2 \text{ cm}^2 \text{ g}^{-1}. \tag{4.36}$$

The complete equations for a static atmosphere are

$$\frac{1}{\rho} \frac{dP_N}{dr} = -\frac{GM}{r^2} \left(1 - \frac{4\pi r^2 F_\gamma}{L_\text{E}} \right), \tag{4.37}$$

$$\frac{dF_\gamma}{dr} + \frac{2F_\gamma}{r} = -ac\kappa_\nu \rho \frac{7\mathcal{N}_\nu}{8} \left[T^4 - T_{\nu 0}^4 \left(\frac{R_\nu}{r} \right)^2 \right], \tag{4.38}$$

$$F_\gamma = -\frac{ac}{3\kappa_\gamma \rho} \frac{dT^4}{dr}. \tag{4.39}$$

Here the Eddington luminotisy is given by

$$L_\text{E} = \frac{4\pi c G M}{\kappa_\gamma}. \tag{4.40}$$

We consider the plane-parallel limit where the radial extent of the atmosphere is much smaller than the radius of the neutron star

$$\frac{dF_\gamma}{dr} \gg \frac{F_\gamma}{r} \quad (r \simeq R_\nu). \tag{4.41}$$

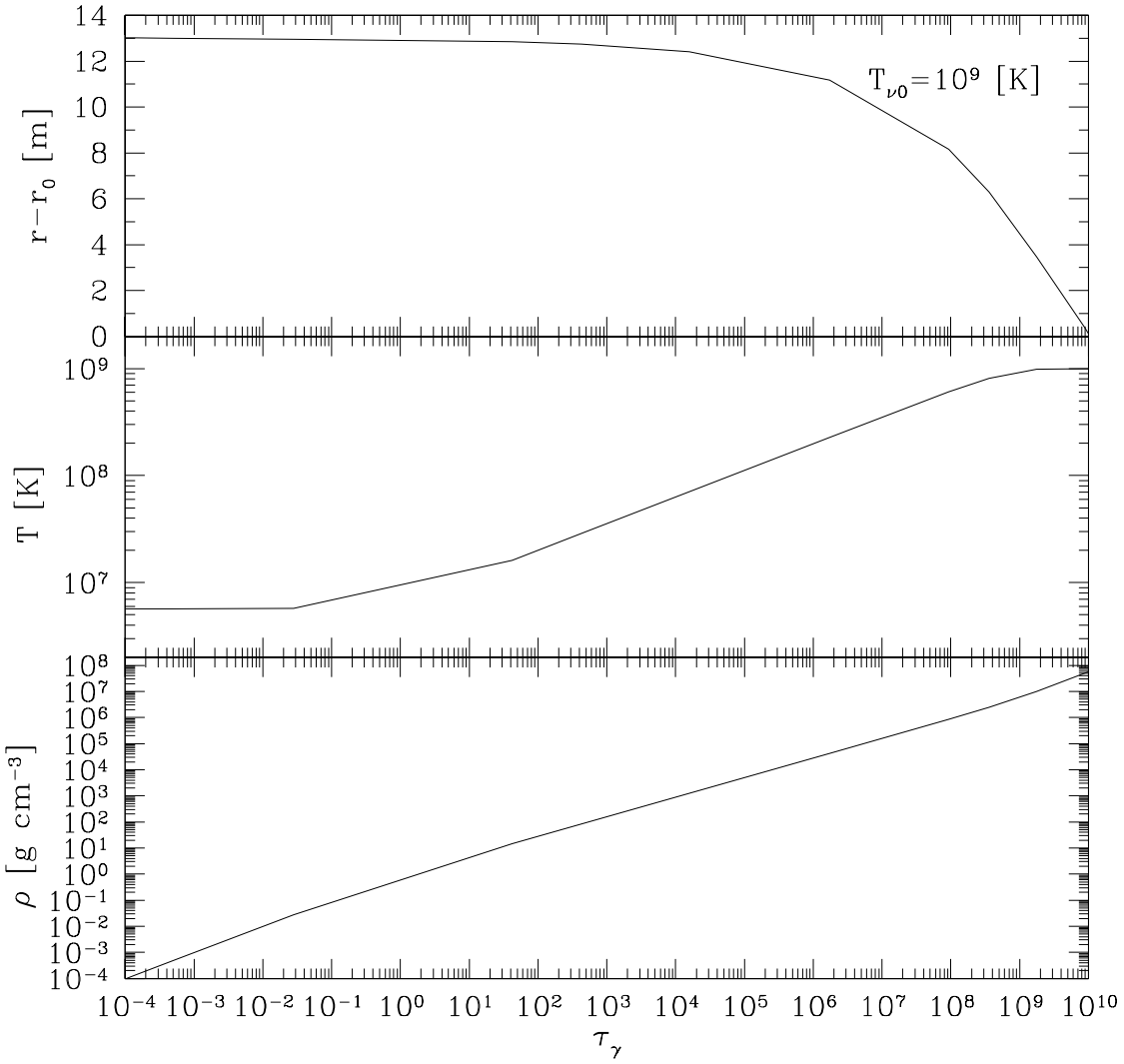

Figure 4.1: Static atmosphere model in Case 2 with $T_{\nu 0} = 10^9$ K. The radius, the temperature, and the density versus optical photon depth τ_γ are shown from top to bottom.

In terms of the photon optical depth τ_γ the equations can be written as

$$\frac{dr}{d\tau_\gamma} = -\frac{1}{\kappa_\gamma \rho}, \tag{4.42}$$

$$\frac{dP_N}{d\tau_\gamma} = \frac{GM}{\kappa_\gamma r^2}\left(1 - \frac{4\pi r^2 F_\gamma}{L_{\rm E}}\right), \tag{4.43}$$

$$\frac{dF_\gamma}{d\tau_\gamma} = ac\left(\frac{\kappa_\nu}{\kappa_\gamma}\right)\frac{7\mathcal{N}_\nu}{8}\left[T^4 - T_{\nu 0}^4\left(\frac{R_\nu}{r}\right)^2\right], \tag{4.44}$$

$$F_\gamma = \frac{ac}{3}\frac{dT^4}{d\tau_\gamma}. \tag{4.45}$$

Eqs. (4.44) and (4.45) yield

$$\frac{d^2T^4}{d\tau_\gamma^2} = \frac{21\mathcal{N}_\nu}{8}\left(\frac{\kappa_\nu}{\kappa_\gamma}\right)\left[T^4 - T_{\nu 0}^4\left(\frac{R_\nu}{r}\right)^2\right]. \tag{4.46}$$

This can be solved analytically with two boundary conditions

$$T = T_{\nu 0} \quad \text{for} \quad \tau_\gamma \to \infty, \tag{4.47}$$

$$F_\gamma = \frac{1}{2}acT^4 \quad \text{at} \quad \tau_\gamma = 0. \tag{4.48}$$

The solution is

$$\left(\frac{T}{T_{\nu 0}}\right)^4 = 1 - be^{-\chi\tau_\gamma}, \tag{4.49}$$

where

$$\chi = \left(\frac{21\mathcal{N}_\nu}{8}\frac{\kappa_\nu}{\kappa_\gamma}\right)^{1/2}, \tag{4.50}$$

and

$$b = \left(1 + \frac{2}{3}\chi\right)^{-1}. \tag{4.51}$$

In the limit of $\chi\tau_\gamma \ll 1$, we get

$$\left(\frac{T}{T_{\nu 0}}\right)^4 \simeq \frac{2}{3}\left(1 + \frac{3}{2}\tau_\gamma\right)\chi. \tag{4.52}$$

Therefore, we reproduce the Eddington atmosphere as

$$T^4 = \frac{2F_\gamma(0)}{ac}\left(1+\frac{3}{2}\tau_\gamma\right), \tag{4.53}$$

where $F_\gamma(0)$ is the emergent photon flux

$$F_\gamma(0) \simeq \frac{\chi}{3} acT_{\nu 0}^4. \tag{4.54}$$

It has been recognized that a static atmosphere does not exist for a high enough neutrinosphere temperature $T_{\nu 0}$ because of the protoneutron star wind. Deep inside the atmosphere, where the neutrino optical depth is large and $T \simeq T_\nu$, the ratio of photon flux to neutron flux is

$$\frac{F_\gamma}{F_\nu} \simeq \frac{\kappa_\nu}{\kappa_\gamma} \quad (\chi\tau_\gamma \gg 1). \tag{4.55}$$

However, near the top of the atmosphere the ratio of emergent fluxes is considerably larger

$$\frac{F_\gamma}{F_\nu} \simeq \left(\frac{\kappa_\nu}{\kappa_\gamma}\right)^{1/2} \quad (\chi\tau_\gamma \ll 1). \tag{4.56}$$

Therefore, an atmosphere that everywhere has a sub-Eddington neutrino flux may have a super-Eddington photon flux from the surface. We get

$$\frac{L_\gamma(0)}{L_E} = \left(\frac{21\mathcal{N}_\nu}{8}\kappa_\nu\kappa_\gamma\right)^{1/2}\frac{aT_{\nu 0}^4 R_\nu^2}{3GM}. \tag{4.57}$$

Thus the threshold value of $T_{\nu 0}$ above which the surface photon luminosity becomes super-Eddington is given by

$$\begin{aligned} T_{\nu 0} &> \left[\frac{21\mathcal{N}_\nu}{8}\kappa_\gamma\left(\frac{\kappa_\nu}{T_{\nu 0}^2}\right)\right]^{-1/10}\left(\frac{3GM}{aR_\nu^2}\right)^{1/5} \\ &= 4.3\times 10^9\left(\frac{R_\nu}{10\text{ km}}\right)^{-2/5}\left(\frac{M}{1.4M_\odot}\right)^{1/5}\text{ K}. \end{aligned} \tag{4.58}$$

Eqs. (4.42) and (4.43) can be solved numerically with appropriate boundary conditions. One boundary condition comes from the condition $P_N = 0$ at $\tau_\gamma = 0$. Integrating Eq. (4.43) to a given small optical depth $\tau_{\gamma,1}$, we get

$$P_{N,1} = \frac{GM}{\kappa_\gamma r_1^2}\left(1 - \frac{4\pi r_1^2 F_{\gamma,1}}{L_{\rm E}}\right)\tau_{\gamma,1}. \tag{4.59}$$

where $P_{N,1}$, $F_{\gamma,1}$, and r_1 are evaluated at $\tau_{\gamma,1}$. The other boundary conditions are imposed at the base of the atmosphere

$$r_2 = R_\nu, \tag{4.60}$$

$$F_{\gamma,2} = 0, \tag{4.61}$$

where r_2 and $F_{\gamma,2}$ are evaluated at large $\tau_{\gamma,2}$ whose value is to be adjusted to satisfy the above three boundary conditions.

In Fig. 4.1, we show a static atmosphere model for $T_{\nu 0} = 10^9$ K. We confirm the Eddington atmosphere feature as given in Eq. (4.53) in the temperature profile for $\tau_\gamma \ll 1$. The height of the atmosphere from the neutrinosphere is of order ~ 10 m. The temperature varies from $\simeq 10^9$ K (base) to $\simeq 10^7$ K (top), which is too low for our purpose. The highest base temperature for which we were able to construct a static atmosphere model is $T_{\nu 0} \simeq 10^9$ K, which is consistent with the threshold temperature given in Eq. (4.58).

4.4 Cooling of the Bulk of a Neutron Star

To obtain the evolution of the base atmosphere temperature, we simulate the cooling of the bulk of a neutron star. We start with a protoneutron star which is opaque to neutrinos. The protoneutron star deleptonizes and cools by neutrino diffusion until it becomes transparent to neutrinos in $\simeq 50$ s.

4.4.1 Equations

We set up our calculations in a similar manner as in Lai & Qian (1998). We consider a protoneutron star which deleptonizes and cools by neutrino diffusion. The equations that govern the deleptonization and thermal cooling are given by

$$\frac{\partial Y_L}{\partial t} = -\frac{1}{n_b}\nabla \cdot \mathbf{S}_L, \tag{4.62}$$

$$\frac{\partial U}{\partial t} = -\nabla \cdot \mathbf{F}, \tag{4.63}$$

where Y_L is the lepton number fraction, n_b is the baryon number density, $\mathbf{S}_L$ is the lepton number flux, U is the energy density, and $\mathbf{F}$ is the energy flux.

We assume that the protoneutron star is made of neutrons, protons, electrons, positrons, photons, and all types of neutrinos. The chemical potentials for the electron-type neutrinos (ν_e and $\bar{\nu}_e$) are non-zero whereas the chemical potentials for the other types of neutrinos are zero. Thus the electron-type neutrinos contribute to both $\mathbf{S}_L$ and $\mathbf{F}$ while the other types of neutrinos contribute only to $\mathbf{F}$, not to $\mathbf{S}_L$. We get

$$\mathbf{S}_L = \mathbf{S}_{\nu_e} - \mathbf{S}_{\bar{\nu}_e}, \tag{4.64}$$

$$\mathbf{F} = \mathbf{F}_{\nu_e} + \mathbf{F}_{\bar{\nu}_e} + \mathbf{F}_{\nu_\mu}, \tag{4.65}$$

where $\mathbf{S}_{\nu_e}$ is the number flux of ν_e, $\mathbf{S}_{\bar{\nu}_e}$ is the number flux of $\bar{\nu}_e$, $\mathbf{F}_{\nu_e}$ is the energy flux of ν_e, $\mathbf{F}_{\bar{\nu}_e}$ is the energy flux of $\bar{\nu}_e$, and $\mathbf{F}_{\nu_e}$ is the energy flux of ν_μ, $\bar{\nu}_\mu$, ν_τ, and $\bar{\nu}_\tau$.

Now we obtain the specific number fluxes and the energy fluxes. The specific number flux $\mathbf{S}_E$ and the specific energy flux $\mathbf{F}_E$ are given by

$$\mathbf{S}_E = -\frac{c}{3\rho\kappa_E^{(\mathrm{tot})}}\nabla n_E, \tag{4.66}$$

$$\mathbf{F}_E = -\frac{c}{3\rho\kappa_E^{(\mathrm{tot})}}\nabla U_E, \tag{4.67}$$

where n_E is the specific number density, U_E is the specific energy density, and

$$\kappa_E^{(\mathrm{tot})} = \kappa_E^{(\mathrm{abs})} + \kappa_E^{(\mathrm{sc})} \tag{4.68}$$

is the total specific opacity including the absorption and the scattering effects. For a given neutrino species i, we assume that the total specific opacity is of the form

$$\kappa_{E,\,i}^{(\mathrm{tot})} = \kappa_{E,\,i}^{(\mathrm{abs})} + \kappa_{E,\,i}^{(\mathrm{sc})} = \kappa_i \left(\frac{E}{E_0}\right)^2, \tag{4.69}$$

where E_0 is a fiducial constant energy. The specific number density and the specific energy density are given by

$$n_{E,\,i} = \frac{U_{E,\,i}}{E} = \frac{1}{2\pi^2(\hbar c)^3} \frac{E^2 dE}{e^{(E-\mu_i)/kT}+1}, \tag{4.70}$$

where μ_i is the chemical potential for the neutrino species i. Integrating over E, we get the number flux and the energy flux of ν_e as

$$\mathbf{S}_{\nu_e} = -\frac{cE_0^2}{6\pi^2(\hbar c)^3 \rho \kappa_\nu} \nabla[(kT)F_0(\eta_\nu)], \tag{4.71}$$

$$\mathbf{F}_{\nu_e} = -\frac{cE_0^2}{6\pi^2(\hbar c)^3 \rho \kappa_\nu} \nabla[(kT)^2 F_1(\eta_\nu)], \tag{4.72}$$

where $\eta_\nu \equiv \eta_{\nu_e} \equiv \mu_{\nu_e}/kT$ is the degeneracy parameter for ν_e and $F_k(\eta)$ is the Fermi-Dirac integral defined as

$$F_k(\eta) \equiv \int_0^\infty \frac{x^k dx}{e^{(x-\eta)}+1}. \tag{4.73}$$

Similarly, the number flux and the energy flux of $\bar{\nu}_e$ are given by

$$\mathbf{S}_{\bar{\nu}_e} = -\frac{cE_0^2}{6\pi^2(\hbar c)^3 \rho \kappa_{\nu_e}} \nabla[(kT)F_0(-\eta_\nu)], \tag{4.74}$$

$$\mathbf{F}_{\bar{\nu}_e} = -\frac{cE_0^2}{6\pi^2(\hbar c)^3 \rho \kappa_{\nu_e}} \nabla[(kT)^2 F_1(-\eta_\nu)], \tag{4.75}$$

where we have used $\eta_{\bar{\nu}_e} = -\eta_{\nu_e} = -\eta_\nu$. Then we get

$$\mathbf{S}_{\nu_e} - \mathbf{S}_{\bar{\nu}_e} = -\frac{cE_0^2}{6\pi^2(\hbar c)^3 \rho \kappa_{\nu_e}} \nabla[(kT)\eta_\nu], \tag{4.76}$$

$$\mathbf{F}_{\nu_e} + \mathbf{F}_{\bar{\nu}_e} = -\frac{cE_0^2}{6\pi^2(\hbar c)^3 \rho \kappa_{\nu_e}} \nabla[(kT)^2 \left(\frac{\eta_\nu^2}{2} + \frac{\pi^2}{6}\right)], \tag{4.77}$$

where we have used the following identities (Bludman & Van Riper 1978)

$$F_0(\eta) - F_0(\eta) = \eta, \tag{4.78}$$

$$F_1(\eta) + F_1(\eta) = \frac{\eta^2}{2} + \frac{\pi^2}{6}. \tag{4.79}$$

The energy flux of ν_μ, $\bar{\nu}_\mu$, ν_τ, and $\bar{\nu}_\tau$ is given by

$$\mathbf{F}_{\nu_\mu} = -\frac{cE_0^2}{18\pi^2\rho\kappa_{\nu_\mu}}\frac{1}{(\hbar c)^3}\nabla[(kT)^2]. \tag{4.80}$$

The lepton number fraction Y_L can be written as

$$Y_L = Y_e + Y_\nu \equiv (Y_{e^-} - Y_{e^+}) + (Y_{\nu_e} - Y_{\bar{\nu}_e}). \tag{4.81}$$

where Y_{e^-}, Y_{e^+}, Y_{ν_e}, and $Y_{\bar{\nu}_e}$ are the number fractions of e^-, e^+, ν_e, and $\bar{\nu}_e$, respectively.

The number density of relativistic fermions of species i is given by

$$n_i = \frac{1}{\pi^2}\left(\frac{kT}{\hbar c}\right)^3 F_2(\eta_i), \tag{4.82}$$

where $\eta_i \equiv \mu_i/kT$ is the degenracy parameter with μ_i being the chemical potential excluding the rest mass energy. Then we get

$$n_e \equiv n_{e^-} - n_{e^+} = Y_e n_b = \frac{1}{\pi^2}\left(\frac{kT}{\hbar c}\right)^3\left(\frac{\eta_e^3}{3} + \frac{\pi^3\eta_e}{3}\right), \tag{4.83}$$

$$n_\nu \equiv n_{\nu_e} - n_{\bar{\nu}_e} = Y_\nu n_b = \frac{1}{\pi^2}\left(\frac{kT}{\hbar c}\right)^3\left(\frac{\eta_\nu^3}{3} + \frac{\pi^3\eta_\nu}{3}\right), \tag{4.84}$$

where we have used the following identity (Bludman & Van Riper 1978)

$$F_2(\eta) - F_2(-\eta) = \frac{\eta^3}{3} + \frac{\pi^3\eta}{3}. \tag{4.85}$$

On the other hand, the number density of nonrelativistic fermions of species i is given by

$$n_i \equiv \frac{1}{2\pi^2\hbar^3}(2m_i kT)^{3/2}F_{1/2}(\eta_i). \tag{4.86}$$

Then we get

$$n_n = (1 - Y_e)n_b = \frac{1}{2\pi^2\hbar^3}(2m_n kT)^{3/2} F_{1/2}(\eta_n), \tag{4.87}$$

$$n_p = Y_e n_b = \frac{1}{2\pi^2\hbar^3}(2m_p kT)^{3/2} F_{1/2}(\eta_p). \tag{4.88}$$

In β-equilibrium, the following relationship holds.

$$\mu_p + \mu_e = \mu_n + \mu_{\nu_e} + 1.293 \text{ MeV}. \tag{4.89}$$

From Eqs. (4.81), (4.83), (4.84), (4.87), (4.87), and (4.89), for a given Y_L, we can obtain Y_e and Y_ν.

The energy density is given by

$$U = U_e + U_\nu + U_{\nu_\mu} + U_\gamma + U_n + U_p, \tag{4.90}$$

where U_e is the energy density of electrons and positrons, U_ν is the energy density of electron-type neutrinos, U_{ν_μ} is the energy density of the other types of neutrinos, U_γ is the energy density of photons, U_n is the energy density of neutrons, and U_p is the energy density of protons. The energy density of relativistic fermions of species i is given by

$$U_i = \frac{1}{\pi^2}\left(\frac{kT}{\hbar c}\right)^3 (kT) F_3(\eta_i). \tag{4.91}$$

Then we get

$$U_e \equiv U_{e^-} + U_{e^+}$$

$$= \frac{7\pi^2}{60}\left[1 + \frac{30}{7}\left(\frac{\eta_e}{\pi}\right)^2 + \frac{15}{7}\left(\frac{\eta_e}{\pi}\right)^4\right]\frac{(kT)^4}{(\hbar c)^3}, \tag{4.92}$$

$$U_\nu \equiv U_{\nu_e} + U_{\bar{\nu}_e}$$

$$= \frac{7\pi^2}{60}\left[1 + \frac{30}{7}\left(\frac{\eta_\nu}{\pi}\right)^2 + \frac{15}{7}\left(\frac{\eta_\nu}{\pi}\right)^4\right]\frac{(kT)^4}{(\hbar c)^3}, \tag{4.93}$$

$$U_{\nu_\mu} = \frac{7\pi^2}{30}\frac{(kT)^4}{(\hbar c)^3}, \tag{4.94}$$

where we have used the following identity (Bludman & Van Riper 1978)

$$F_3(\eta) + F_3(-\eta) = \frac{7\pi^4}{60} + \frac{\pi^2}{2}\eta^2 + \frac{1}{4}\eta^4. \tag{4.95}$$

The energy density of photons is given by

$$U_\gamma = \frac{\pi^2}{15}\frac{(kT)^4}{(\hbar c)^3}. \tag{4.96}$$

The energy density of nonrelativistic fermions of species i is given by

$$U_i = \frac{1}{2\pi\hbar^3}(2m_i kT)^{3/2} kT F_{3/2}(\eta_i). \tag{4.97}$$

Then we get

$$U_n = \frac{1}{2\pi\hbar^3}(2m_n kT)^{3/2} kT F_{3/2}(\eta_n) + (1.293\ \mathrm{MeV})\, n_n, \tag{4.98}$$

$$U_p = \frac{1}{2\pi\hbar^3}(2m_p kT)^{3/2} kT F_{3/2}(\eta_p), \tag{4.99}$$

where U_n includes the rest mass energy.

Eqs. (4.62) and (4.63) can now be written as

$$\frac{\partial Y_L}{\partial t} = \frac{cE_0^2}{6\pi^2(\hbar c)^3 n_b r^2}\frac{\partial}{\partial r}\left(\frac{r^2}{\rho\kappa_{\nu_e}}\frac{\partial G}{\partial r}\right), \tag{4.100}$$

$$\frac{\partial U}{\partial t} = \frac{cE_0^2}{6\pi^2(\hbar c)^3 r^2}\frac{\partial}{\partial r}\left(\frac{r^2}{\rho\kappa_{\nu_e}}\frac{\partial H}{\partial r}\right), \tag{4.101}$$

where

$$G = (kT)\eta_\nu, \tag{4.102}$$

$$H = \frac{1}{2}(kT)^2\left(\eta_\nu^2 + \frac{\pi^2}{3}\right) + \frac{\pi^2\kappa_{\nu_e}}{3\kappa_{\nu_\mu}}(kT)^2. \tag{4.103}$$

4.4.2 Neutrino Opacities

For the neutrino opacities, we essentially follow the description by Burrows & Lattimer (1986). The most important reactions are scattering of all types of neutrinos

off nucleons

$$\nu + n \;\rightarrow\; \nu + n, \tag{4.104}$$

$$\nu + p \;\rightarrow\; \nu + p, \tag{4.105}$$

and absorption of electron-type neutrinos by nucleons

$$\nu_e + n \rightarrow e^- + p, \tag{4.106}$$

$$\bar{\nu}_e + p \rightarrow e^+ + n. \tag{4.107}$$

The cross sections to the above reactions for different regimes are given in Burrows & Lattimer (1986). For neutrino scattering off neutrons, we have

$$\sigma_n = \begin{cases} \sigma_{\rm ref} = (\sigma_0/4)(E_\nu/m_e c^2)^2 & \text{for } n\text{ND},\ \nu\text{ND or } \nu\text{D} \\ \sigma_{\rm ref}(1+4g_A^2)/5(\langle E_\nu\rangle/p_{F,\,n}c) & \text{for } n\text{D},\ \nu\text{ND} \\ \sigma_{\rm ref}(\pi^2/16)(1+2g_A^2) & \\ \times(kT/\langle E_\nu\rangle)(kT/p_{F,\,n}c)(m_n c^2/E_{F,\,n}) & \text{for } n\text{D},\ \nu\text{D}. \end{cases} \tag{4.108}$$

For neutrino scattering off protons, we have

$$\sigma_p = \begin{cases} \sigma_n & \text{for } p\text{ND},\ \nu\text{ND or } \nu\text{D} \\ \sigma_n(Y_n/Y_p)^{1/3} & \text{for } p\text{D},\ \nu\text{ND} \\ \sigma_n(Y_n/Y_p) & \text{for } p\text{D},\ \nu\text{D}. \end{cases} \tag{4.109}$$

Finally, for neutrino absorption by nucleons, we have

$$\sigma_{\rm a} = \begin{cases} \sigma_{\rm ref}(1+3g_A^2) & \text{for } n\text{ND},\ \nu\text{ND} \\ \sigma_{\rm ref}(1+3g_A^2)2Y_p/(Y_n+Y_p) & \text{for } n\text{D},\ \nu\text{ND or } \nu\text{D},\ \text{opaque} \\ \sigma_{\rm ref}(1+3g_A^2)(3\pi^2/32)\times(kT/\langle E_\nu\rangle) & \\ \times(m_n c^2/E_{F,\,n})(Y_e/Y_n)^{1/3} & \text{for } n\text{D},\ \nu\text{D} \\ 0 & \text{for } n\text{D},\ \mathrm{Y_L} < 0.08. \end{cases} \tag{4.110}$$

Here "ND" stands for nondegenerate, "D" stands for degenerate, E_ν is the neutrino energy, $\langle E_\nu \rangle$ is the averaged neutrino energy, $p_{F,n}$ is the neutron Fermi momentum, $E_{F,n}$ is the neutron Fermi energy, $g_A = 1.254$ is the axial-vector coupling constant, and σ_0 is defined as

$$\sigma_0 \equiv \frac{4}{\pi}\left(\frac{\hbar}{m_e c^2}\right)^{-4}\left(\frac{G_F}{m_e c^2}\right)^2 = 1.76 \times 10^{-44}\ \mathrm{cm}^2. \tag{4.111}$$

We note that all cross sections scale as E_ν^2 as we have assumed in Eq. (4.69).

4.4.3 Numerical Results

We now describe our numerical methods. We solve Eqs. (4.100) and (4.101) using the explicit finite difference method. We use 50 equally spaced grid points. For a given grid size Δr, the diffusive timescales for Eqs. (4.100) and (4.101) are given by

$$(\Delta t)_{Y_L} = \frac{6\pi^2(\hbar c)^3 n_b r^2}{c E_0^2}\frac{(\Delta r)^2 Y_L}{G}, \tag{4.112}$$

$$(\Delta t)_U = \frac{6\pi^2(\hbar c)^3 r^2}{c E_0^2}\frac{(\Delta r)^2 U}{H}. \tag{4.113}$$

The actual timestep Δt is chosen so that it is smaller than the above diffusive timescales and is small enough to guarantee the numerical of the code. For the calculations of the Fermi integrals $F_{1/2}(\eta)$, $F_{2/3}(\eta)$, and their inverses we use the fitting formulae given by Antia (1993).

We fix the density profile throughout the evolution. We use a $\Gamma = 3$ polytrope which resembles a relatively stiff equation of state. The model has a mass of $1.53 M_\odot$, a radius of 11.8 km, and a central density of $7.88 \times 10^{14}\ \mathrm{g\,cm^{-3}}$. The outer boundary is located at a density of $1.6 \times 10^{14}\ \mathrm{g\,cm^{-3}}$. For the initial lepton fraction and the temperature profiles, we use the "hot" model described in Keil &

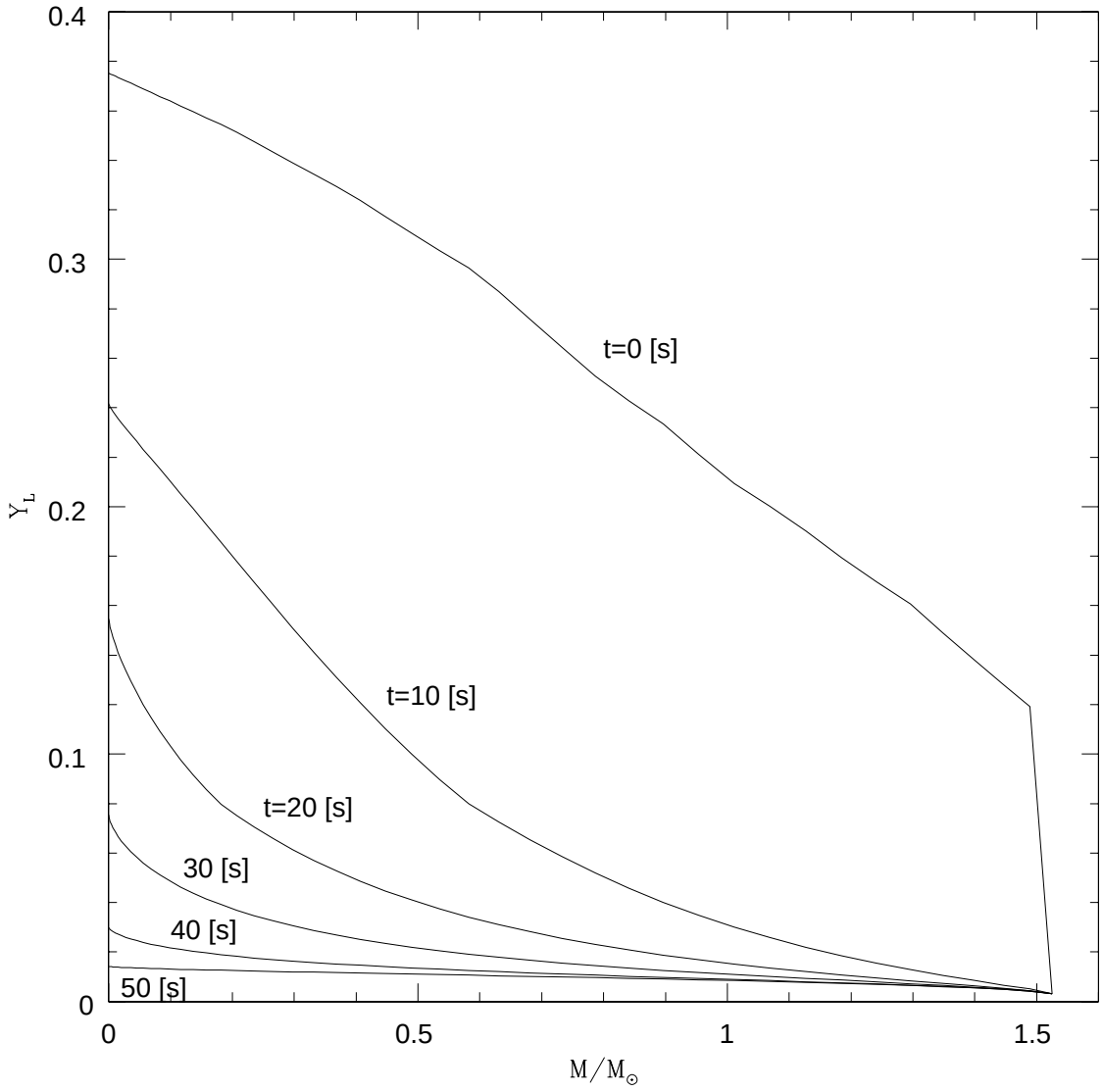

Figure 4.2: Evolution of the lepton fraction Y_L of a protoneutron star.

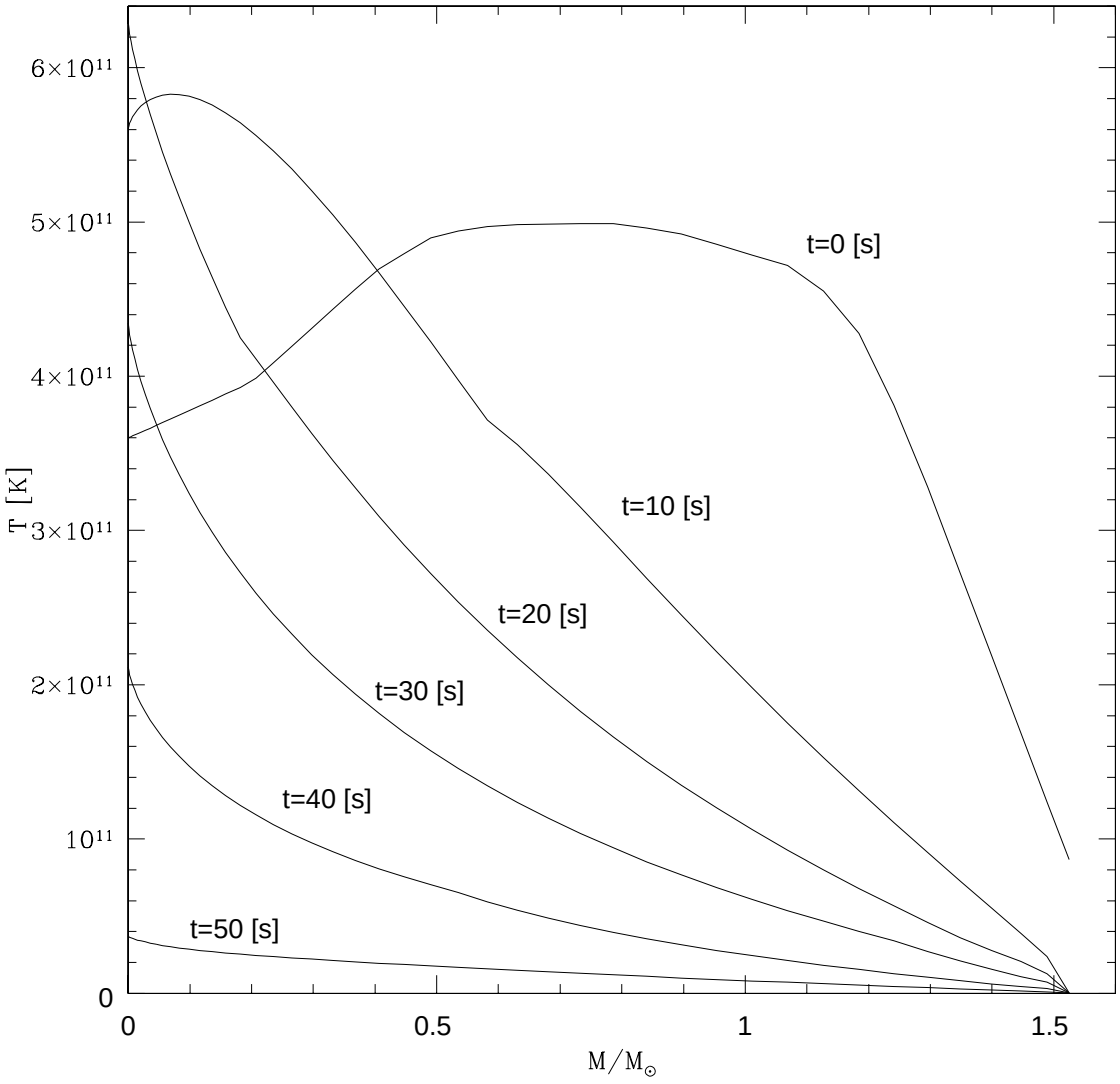

Figure 4.3: Evolution of the temperature T of a protoneutron star.

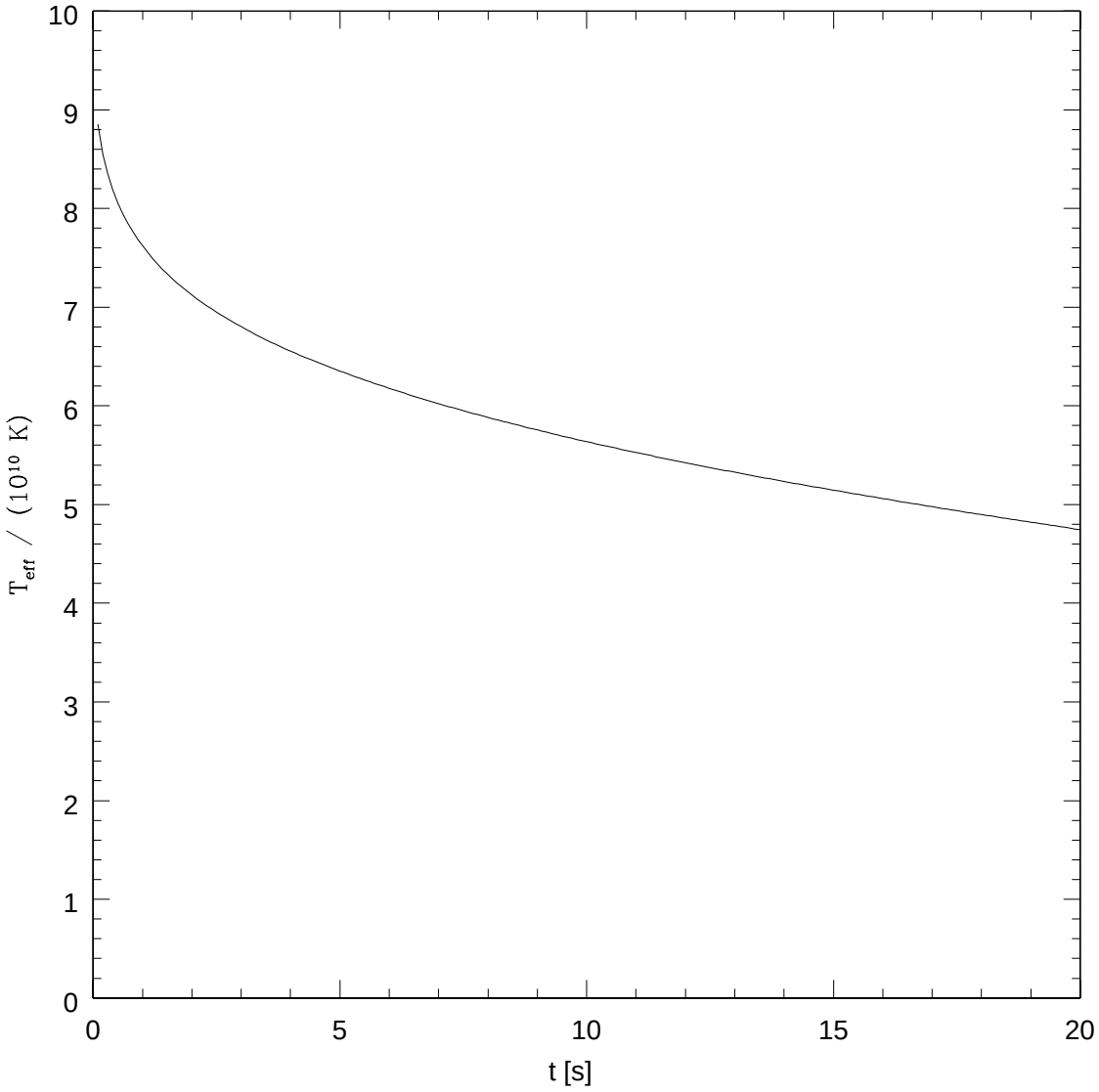

Figure 4.4: Time evolution of the effective temperature $T_{\rm eff}(t)$ of a protoneutron star up tp $t = 20$ s.

Janka (1995). For the spatial boundary conditions, we set $dY_L/dr = dU/dr = 0$ at the center, and $Y_L = 4.0 \times 10^{-3}$ and $T = 1.0 \times 10^9$ K at the outer boundary.

Here are the results of our calculations. The evolutions of the lepton number fraction Y_L and the temperature T up to $t = 50$ s are shown in Figure 4.2 and Figure 4.3, respectively.

We estimate the effective temperature $T_{\rm eff}(t)$ of the protoneutron star from the total neutrino energy flux $F(t)$. From Eqs.(4.63) and (4.101), we get

$$F(t) = -\frac{cE_0^2}{6\pi^2(\hbar c)^3}\frac{1}{\rho\kappa_{\nu_e}}\frac{\partial H_0}{\partial r}. \tag{4.114}$$

Then we get get $T_{\rm eff}(t)$ assuming the blackbody neutrino emission

$$F(t) = \frac{7\mathcal{N}_\nu}{8}\sigma_{\rm SB}T_{\rm eff}(t)^4, \tag{4.115}$$

where $\sigma_{\rm SB}$ is the Stephan-Boltzmann constant. The time evolution of the effective temperature $T_{\rm eff}(t)$ is shown in Figure 4.4. This can be used as a measure of the neutrinosphere temperature $T_{\nu 0}(t)$.

The longest time we were able to run the code before we encountered any numerical problems was $\simeq$ 50 s. This is due to a breakdown of the diffusion approximation for neutrinos in the neutron star. For $\gtrsim$ 50 s, we need an alternative treatment for the cooling of the neutron star.

4.5 Nuclear Statistical Equilibrium Composition

Nuclear statistical equilibrium (NSE) is realized when all the possible nuclear reactions are in equilibrium. We will use the NSE composition as the initial chemical composition for our nucleosynthesis calculation. Whether NSE holds or not for a system depends on the timescale of the system's thermal evolution and the

timescales of (the slowest) nuclear reactions. For most astrophysical systems, it is considered that the NSE holds for temperatures $\gtrsim 3 \times 10^9$ K.

We safely assume that all nuclei and nucleons are nonrelativistic and nondegenerate in young neutron star atmospheres. The chemical potential $\mu(Z, A)$ of the nuclei with atomic number Z and mass number A is given by

$$\frac{\mu(Z,A) - m(Z,A)c^2}{kT} = \ln\left[\frac{n(Z,A)}{g(Z,A)}\left(\frac{2\pi\hbar^2}{m(Z,A)kT}\right)^{3/2}\right], \tag{4.116}$$

where $m(Z, A)$, $n(Z, A)$, and $g(Z, A)$ are the mass, the number density, and the statistical weight of the nuclei, respectively. In the NSE, all the possible nuclear reactions are in equilibrium. Typical reactions are of the forms

$$(Z,A) + p \;\rightleftharpoons\; \gamma + (Z+1, A+1), \tag{4.117}$$

$$(Z,A) + n \;\rightleftharpoons\; \gamma + (Z, A+1), \tag{4.118}$$

as well as reactions such as (α, γ), (α, p), (α, n), (p, n), and so on. The condition for all the possible reactions to be in equilibrium is given by the balance of chemical potentials for the nucleus and its constituent nucleons

$$\mu(Z,A) = Z\mu_p + (A-Z)\mu_n, \tag{4.119}$$

where μ_p and μ_n are the chemical potentials for the proton and the neutron, respectively. Using the expression of the chemical potential given in Eq. (4.116), we get

$$n(Z,A) = \frac{g(Z,A)A^{3/2}}{2^A\theta^{A-1}} n_p^Z n_n^{A-Z} \exp\left[\frac{Q(Z,A)}{kT}\right], \tag{4.120}$$

where n_p and n_n are the number densities of the protons and neutrons,

$$Q(Z,A) = c^2[Zm_p + (A-Z)m_n - M(Z,A)] \tag{4.121}$$

is the nuclear binding energy, and

$$\theta \equiv \left(\frac{m_u kT}{2\pi\hbar^2} \right)^{3/2}, \tag{4.122}$$

with m_u being the atomic mass unit. The baryon and charge conservations give

$$\sum_{(Z,A)} n(Z,A)A = \frac{\rho}{m_u} = n_b, \tag{4.123}$$

$$\sum_{(Z,A)} n(Z,A)Z = n_b Y_e, \tag{4.124}$$

where n_b is the baryon number density. If a group of nuclei and the binding energy of each nuclear species is specified for a given set of ρ, T, and Y_e, all the nuclear statistical equilibrium number densities n_p, n_n, and n_i's will be determined from Eqs. (4.120) – (4.124).

We use the NSE code (Timmes 2003) that includes the same 46 isotopes included in the nuclear reaction network used in § 4.6. The 46 isotopes are ^{2}H, ^{3}He, ^{7}Li, $^{7-8}$Be, ^{8}B, $^{12-13}$C, $^{13-15}$N, $^{14-18}$O, $^{17-19}$F, $^{18-20}$Ne, ^{23}Na, $^{23-24}$Mg, ^{27}Al, $^{27-28}$Si, $^{30-31}$P, $^{31-32}$S, ^{35}Cl, ^{36}Ar, ^{39}K, ^{40}Ca, ^{43}Sc, ^{44}Ti, ^{47}V, ^{48}Cr, ^{51}Mn, ^{52}Fe, ^{55}Co, ^{56}Ni, n, p, and ^{4}He.

We calculated the NSE compositions for densities ranging from $\rho = 10^{-4}$ g cm^{-3} to 10^{8} g cm^{-3} at two different temperatures $T = 10^{10}$ K and $T = 3 \times 10^{9}$ K, with $Y_e = 0.5$ fixed. The results are shown in Fig. 4.5.

Once a static atmosphere model is constructed in a high enough temperature regime, the NSE composition of the atmosphere can be calculated in a similar manner as done in this section and can be used as the initial chemical composition.

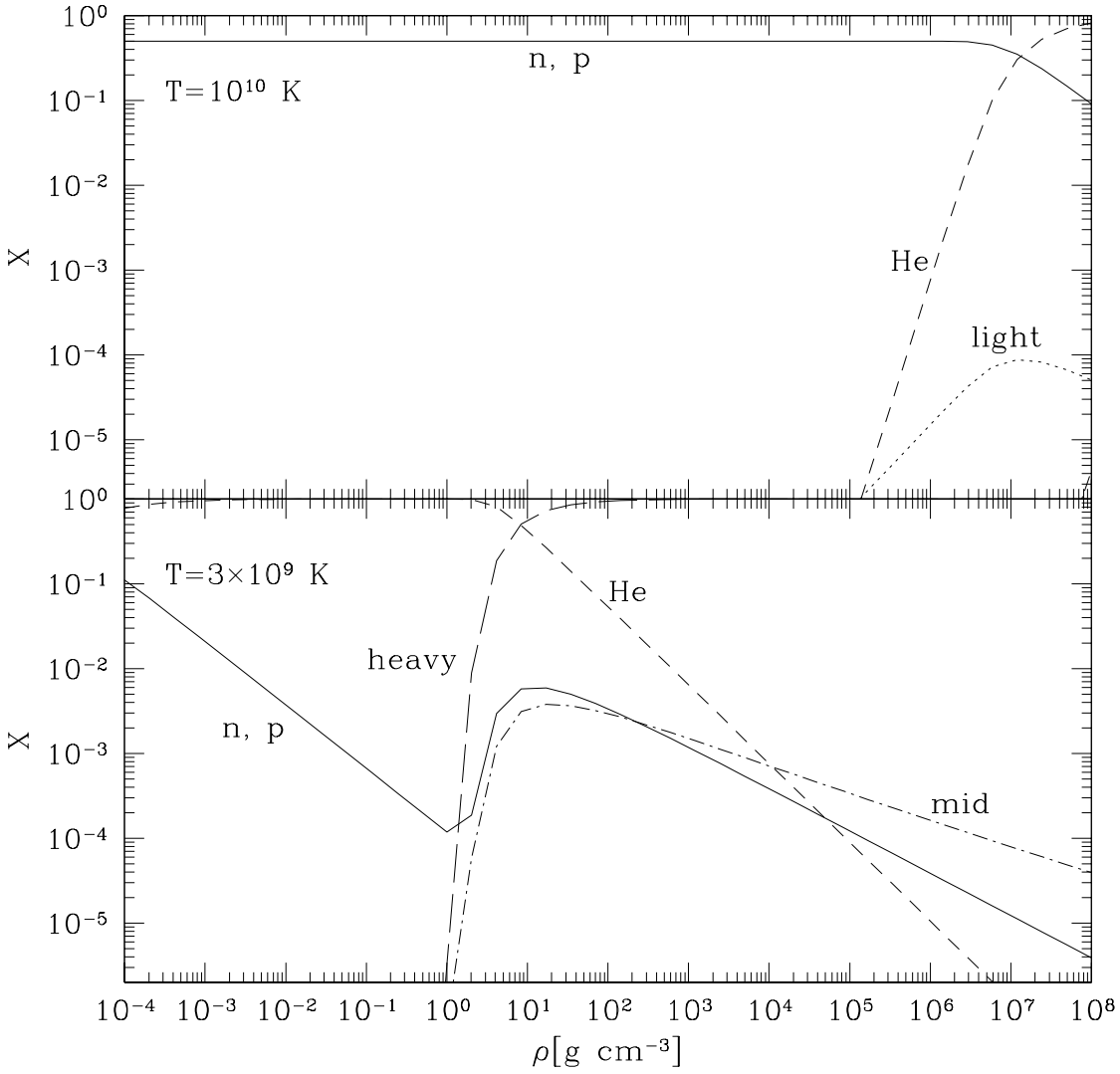

Figure 4.5: NSE composition for a range of densities at two different temperatures $T = 1.0 \times 10^{10}$ K (top panel) and $T = 3.0 \times 10^{9}$ K (bottom panel). We set $Y_e = 0.5$. The solid line is for the proton (neutron) mass fraction, the short dash line is for the ^{4}He mass fraction, the dotted line is for the mass fraction of the light elements (from ^{2}H to ^{8}B except ^{4}He), the dot-short dash line is for the mass fraction of the intermediate mass elements (from ^{12}C to ^{40}Ca), and the long dash line is for the mass fraction of the heavy elements (from ^{43}Sc to ^{56}Ni).

4.6 Nucleosynthesis Calculation

Our goal is to perform a nucleosynthesis calculation in a cooling, young neutron star atmosphere. As a first step, we perform a nucleosynthesis calculation in a single mass shell of the atmosphere.

We start with nucleons at a very high temperature ($\simeq 10^{10}$ K). Protons will combine into helium by high-temperature tails of the pp-chains and the CNO-cycles. At the same time, protons and neutrons will go back to iron-peak elements directly by the reverse reactions of photodissociation. Once ^{4}He nuclei are formed, the α-chains will become important. In order to take into account these reactions, we adopt the "torch47" nuclear reaction network (Timmes 2003) which includes 47 isotopes. The 47 isotopes are ^{1}H, ^{2}H, ^{3}He, ^{7}Li, $^{7-8}$Be, ^{8}B, $^{12-13}$C, $^{13-15}$N, $^{14-18}$O, $^{17-19}$F, $^{18-20}$Ne, ^{23}Na, $^{23-24}$Mg, ^{27}Al, $^{27-28}$Si, $^{30-31}$P, $^{31-32}$S, ^{35}Cl, ^{36}Ar, ^{39}K, ^{40}Ca, ^{43}Sc, ^{44}Ti, ^{47}V, ^{48}Cr, ^{51}Mn, ^{52}Fe, ^{55}Co, ^{56}Ni, n, p, and ^{4}He. We note that, in the original "torch47" network that concerns the nuclear burnings in a star, ^{1}H which stands for the hydrogen already present in the star and p which stands for the protons produced by photodissociation are tracked separately. Here we make no distinction between ^{1}H and p. The 47 isotope reaction network has hydrogen burning reactions such as the pp-chains and the CNO cycles, the α-chains, heavy ion reactions such as ^{12}C $+^{12}$ C, ^{12}C $+^{16}$ O, and ^{16}O $+^{16}$ O, the $(\alpha,\, p)\,(p,\, \gamma)$ links, and photodissociation of iron-peak elements.

In addition to energy generation due to nuclear reactions, energy loss due to neutrino processes are included in the "torch47" code. The included neutrino processes are pair annihilation: $e^- + e^+ \rightarrow \nu + \bar{\nu}$, photoannihilation: $e^- + \gamma \rightarrow e^- + \nu + \bar{\nu}$, bremsstrahlung: $e^- + (Z, A) \rightarrow (Z, A) + e^- + \nu + \bar{\nu}$, plasmon decay, and recombination neutrino process (a neutrino pair is produced when a free electron

is captured in the K-shell around a fully ionized nucleus of atomic charge Z) as well as the neutrio processes in the pp-chains and the CNO-cycles.

We use the "torch47" code (Timmes 2003) for our calculations. The calculations are done in the "self-heating mode" in which the density of matter is fixed as the internal energy, the temperature, and the chemical composition change. The change of internal energy U is written as

$$\frac{dU}{dt} = \frac{dU}{dT}\frac{dU}{dt} + \frac{dU}{d\rho}\frac{d\rho}{dt} + \sum_i \frac{dU}{dX_i}\frac{dX_i}{dt}, \tag{4.125}$$

$$\frac{d\rho}{dt} = 0. \tag{4.126}$$

In Fig. 4.6, we show the results of a "torch47" network calculation for an initial chemical composition $^1\mathrm{H} = n = 0.5$ and an initial temperature $T_i = 10^{10}$ K with a fixed density of $\rho = 10^{-2}$ g cm^{-3} for a duration of $t_f = 10^8$ s. The final chemical composition is mostly ^{4}He followed by nucleons and intermediate mass elements ($^4\mathrm{He} = 9.999 \times 10^{-1}$, $p = n = 5.803 \times 10^{-5}$, $^{32}\mathrm{S} = 2.064 \times 10^{-7}$, $^{28}\mathrm{Si} = 6.627 \times 10^{-8}$, and etc.). The final temperature is $T_f = 9.9 \times 10^8$ K. The temperature evolution is shown in Fig. 4.7.

We attempted a similar calculation using a smaller nuclear reaction network "aprox19" (Timmes 2003) which is essentially a simpler version of the "torch47" code. In the "aprox19" code, the included 19 nuclei are ^{1}H, ^{3}He, ^{4}He, ^{12}C, ^{14}N, ^{16}O, ^{20}Ne, ^{24}Mg, ^{28}Si, ^{32}S, ^{36}Ar, ^{40}Ca, ^{44}Ti, ^{48}Cr, ^{52}Fe, ^{54}Fe, ^{56}Ni, n, and p. As in "torch47" the nuclear reactions taken into account are hydrogen burning reactions such as the pp-chains and the CNO cycles, the α-chains, heavy ion reactions such as $^{12}\mathrm{C}+^{12}\mathrm{C}$, $^{12}\mathrm{C}+^{16}\mathrm{O}$, and $^{16}\mathrm{O}+^{16}\mathrm{O}$, the $(\alpha,\, p)\,(p,\, \gamma)$ links, and photodissociation of iron-peak elements. The difference from the "torch47" is an approximate treatment of the $(\alpha,\, p)\,(p,\, \gamma)$ link and photodissociation of iron-peak elements. We tried the

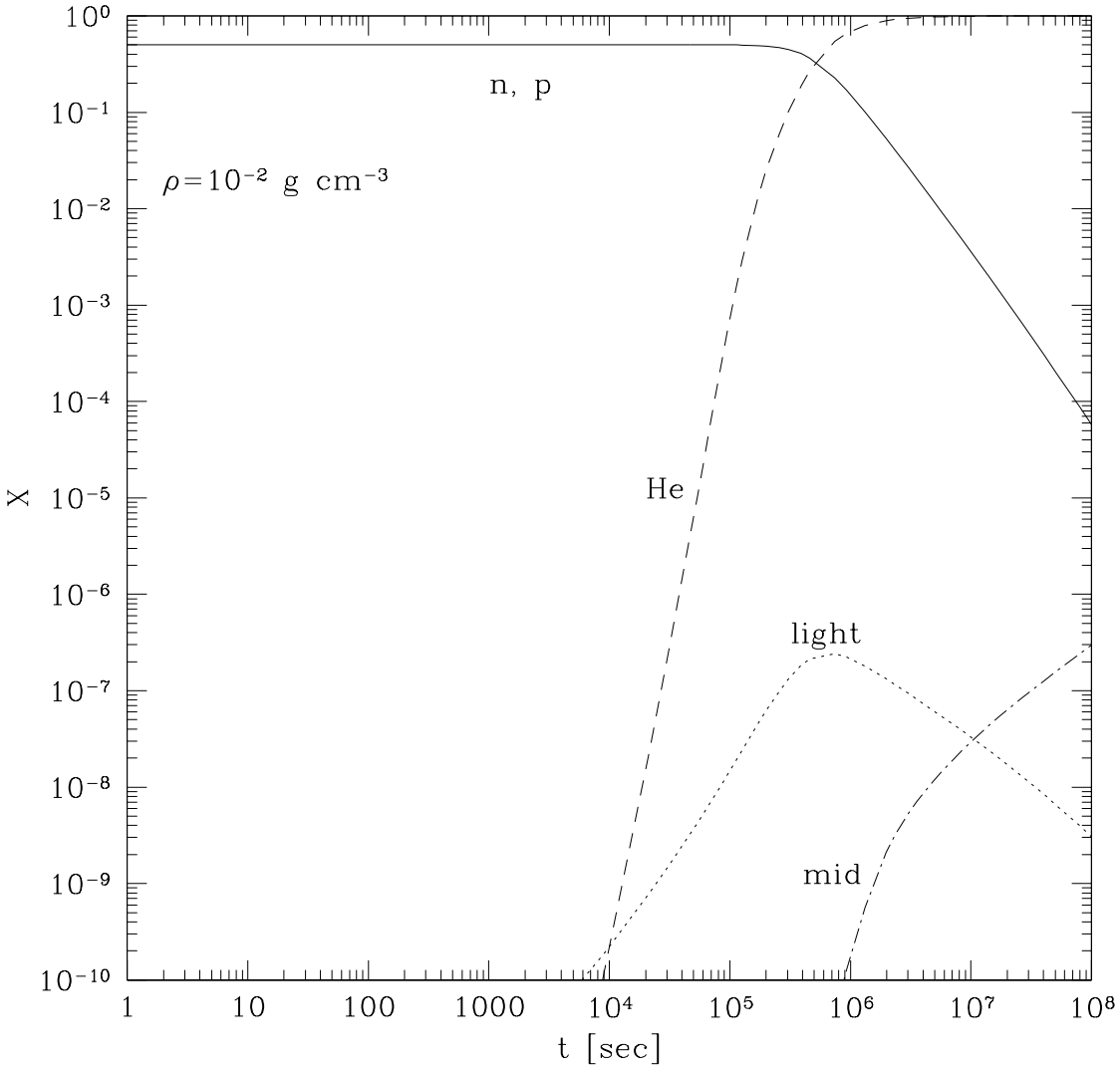

Figure 4.6: Evolution of the mass fractions as functions of time. The calculation is for a half-proton, half-neutron mixture with and initial temperature $T_i = 10^{10}$ K and fixed density $\rho = 10^{-2}$ g cm^{-3} for a duration of $t_f = 10^8$ s. The conventions for the lines are the same as in Fig. 4.5. The solid line is for proton (neutron) mass fraction, the short dash line is for ^{4}He mass fraction, the dotted line is for the mass fraction of the light elements (from ^{2}H to ^{8}B except ^{4}He), the dot-short dash line is for the mass fraction of the intermediate mass elements (from ^{12}C to ^{40}Ca), and the long dash line is for the mass fraction of the heavy elements (from ^{43}Sc to ^{56}Ni).

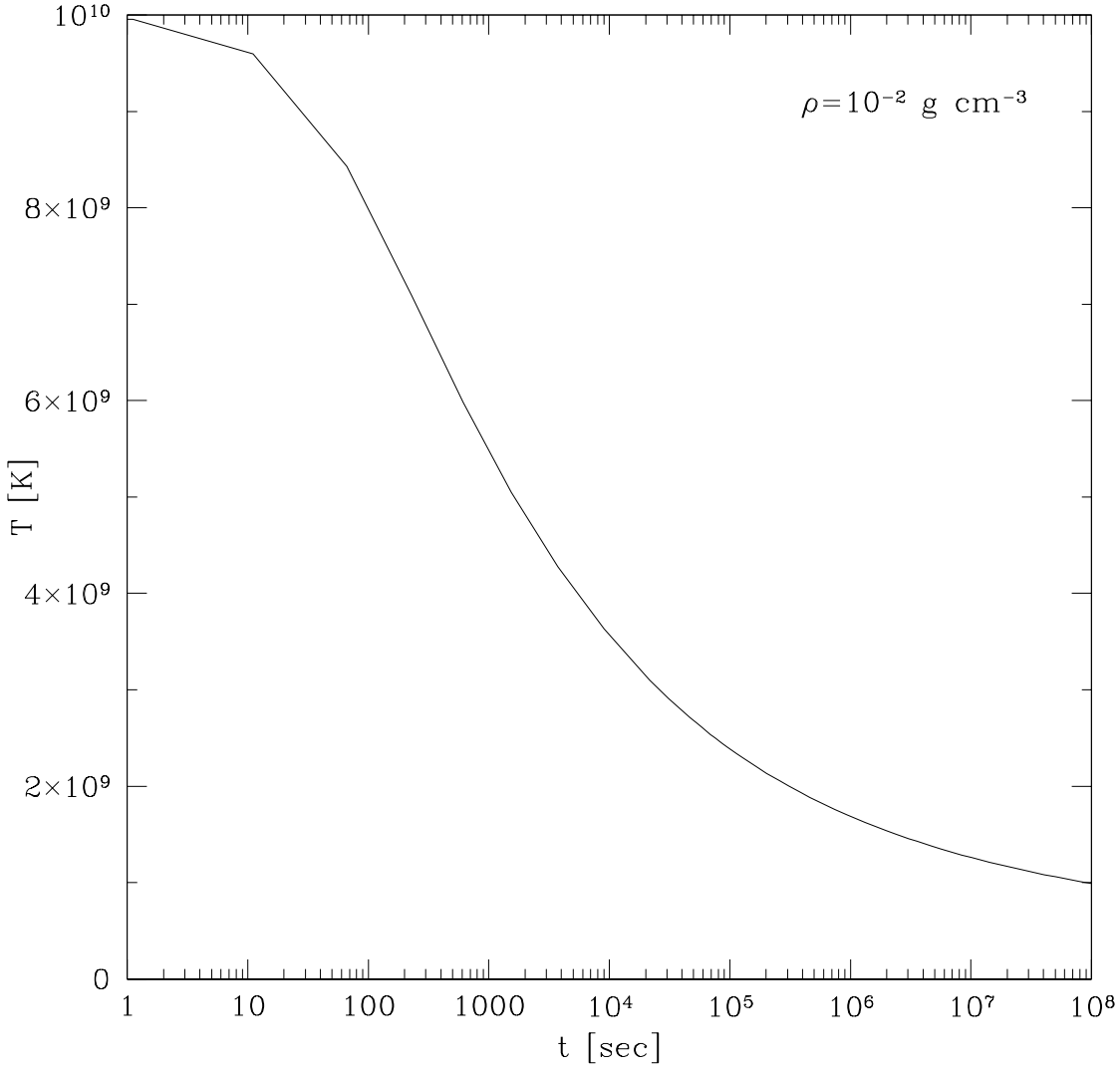

Figure 4.7: Temperature evolution in the same nucleosynthesis calculation as in Fig. 4.6.

same calculation: the same initial chemical composition $^1\mathrm{H} = n = 0.5$ and an initial temperature $T_i = 10^{10}$ K with a fixed density of $\rho = 10^{-2}$ g cm^{-3} for a duration of $t_f = 10^8$ s. However, we encountered a numerical instability during the calculation. This is due to the high initial temperature ($T_i = 10^{10}$ K). For a system which is close to nuclear equilibrium, the nucleosynthesis calculations tend to develop numerical instabilities by doing calculations such as subtraction of a large number from a large number. For a lower initial temperature (e.g., $T_i = 10^8$ K), we comfirmed that the "aprox19" code is numerically stable and produces the same results as the "torch47".

4.7 Possible Role of Diffusion

We discuss how diffusion can affect the evolution of the chemical composition of a young neutron star atmosphere. For a neutron star atmosphere, it is known that gravitational settling (i.e., pressure diffusion) is so efficient that it quickly stratifies the elements in the atmosphere into layers, from the lightest element on the top to the heaviest element at the bottom. Here we estimate the timescale of gravitational settling for a hot neutron star atmosphere. The estimated timescale should be compared with the timescales of nuclear reactions to determine whether diffusion plays an important role in the evolution of the chemical composition of a young neutron star atmosphere. We also discuss the equilibrium concentration that may be useful if diffusion turns out to be important.

We use the two-particle diffusion approximation. We consider a trace limit in which the number density n_1 of the main element (element 1) is much larger than the number density n_2 of the trace element (element 2). We also assume that the particles are nondegenrate and fully ionized, interacting solely by the Coulomb

interaction. The relative diffusion velocity of the element 2 to the main element 1 in the radial direction is given by (see Fontaine & Michaud 1979)

$$v_2 - v_1 = D_{12} \left\{ -\frac{d \ln c_2}{dr} + (1+f) \left[\frac{A_2}{A_1}(1+Z_1) - Z_2 - 1 \right] \frac{d \ln P}{dr} \right\}, \quad (4.127)$$

where D_{12} is the diffusion coefficient, f gives the relative importance of the thermal diffusion to the pressure diffusion, Z_i is the chrage number of the species i, A_i is the mass number of the species i, and c_2 is the concentration of the trace element (element 2) [$c_2 \equiv n_2/(n_1+n_2) \simeq n_2/n_1$]. The first term describes the concentration diffusion that can be ignored here. It is also known that the thermal diffusion is negligible compared to the pressure diffusion (i.e., $f \ll 1$; Fontaine & Michaud 1979). The diffusion coefficient D_{12} is given by

$$D_{12} = \frac{3(kT)^{5/2}}{2(2\pi)^{1/2}[A_1 A_2/(A_1+A_2)]^{1/2} m_u^{1/2} n_1 Z_1^2 Z_2^2 e^4 \ln \Lambda}, \quad (4.128)$$

where $\ln \Lambda$ is the Coulomb logarithm. We can see from Eq. (4.127) that if the coefficient of the pressure gradient $[(A_2/A_1)(Z_1+1) - Z_2 - 1]$ is positive the trace element (element 2) diffuses downward due to gravitational settling and this is usually the case if the trace element (element 2) is heavier than the main element (element 1).

The downward diffusion velocity of the trace element (element 2) due to gravitational settling alone is then given by

$$\begin{aligned} v_g &= D_{12} \left[\frac{A_2}{A_1}(1+Z_1) - Z_2 - 1 \right] \frac{\rho g}{P}, \\ &\simeq \frac{3A_1}{2(2\pi)^{1/2}[A_1 A_2/(A_1+A_2)]^{1/2}} \left[\frac{A_2}{A_1}(1+Z_1) - Z_2 - 1 \right] \\ &\quad \times \frac{(kT)^{3/2} m_u^{1/2} g}{n_1 Z_1^2 Z_2^2 e^4 \ln \Lambda}, \end{aligned} \quad (4.129)$$

where in the first line we have used $dP/dr = -\rho g$ and in the second line we have used $\rho \simeq n_1 A_1 m_u$, $P \simeq n_1 kT$, and the expression for D_{12} given in Eq. (4.128).

Then the timescale of gravitational settling over the pressure scale height $H = |P/(dP/dr)| \simeq kT/A_1 m_u g$ is given by

$$\begin{aligned} t &\simeq \frac{H}{v_g} \\ &\simeq \frac{2(2\pi)^{1/2}[A_1 A_2/(A_1+A_2)]^{1/2}}{3A_1^2}\left[\frac{A_2}{A_1}(1+Z_1)-Z_2-1\right]^{-1} \\ &\quad \times \frac{n_1 Z_1^2 Z_2^2 e^4 \ln\Lambda}{(kT)^{1/2} m_u^{3/2} g^2}. \end{aligned} \tag{4.130}$$

Consider, for example, a trace of helium in a background of hydrogen ($Z_1 = 1$, $A_1 = 2$, $Z_2 = 2$, and $A_2 = 4$) in the neutron star atmosphere. Then we get

$$t \simeq 1.0 \times 10^{-2} \left(\frac{\rho}{10^{-2}\ \mathrm{g\,cm^{-3}}}\right)\left(\frac{T}{10^{10}\ \mathrm{K}}\right)^{-1/2}\ \mathrm{s}, \tag{4.131}$$

where we have used $n_1 \simeq \rho/(A_1 m_u)$, $g \simeq 2.1 \times 10^{14}\ \mathrm{cm\,s^{-2}}$ and $\ln\Lambda \simeq 15$. This gravitational settling timescale should be compared with the timescales of nuclear reactions. If the gravitational settling timescale is comparable to or smaller than the timescales of nuclear reactions, diffusion plays an important role in the evolution of the chemical composition of a young neutron star atmosphere. This is likely the case.

A simple way to estimate the timescale of gravitational settling is as follows. Consider a trace of element 2 embedded in the background of element 1. The downward drift speed is estimated as

$$v_{\mathrm{drift}} = g\, t_{\mathrm{fric}}, \tag{4.132}$$

where t_{fric} is the friction timescale and g is the gravitational acceleration. We estimate t_{frict} as

$$\frac{A_1 m_u}{t_{\mathrm{fric}}} \sim n_1 \sigma_{\mathrm{Coul}} A_1 m_u w_1. \tag{4.133}$$

Here $\sigma_{\rm Coul}$ is the Coulomb collision cross section given by

$$\sigma_{\rm Coul} \sim \frac{Z_1^2 Z_2^2 e^4}{(kT)^2} \ln\Lambda \tag{4.134}$$

with $\ln\Lambda$ being the Coulomb logarithm and w_1 is the thermal velocity of element 1 given by

$$w_1 \sim \left(\frac{kT}{A_1 m_u}\right)^{1/2}. \tag{4.135}$$

Then we get

$$v_{\rm drift} \sim \frac{A_2}{A_1^{1/2}} \frac{(kT)^{3/2} m_u^{1/2} g}{n_1 Z_1^2 Z_2^2 e^4 \ln\Lambda}, \tag{4.136}$$

which reproduces, in the $A_2 \gg A_1$ limit, the diffusion velocity obtained in Eq. (4.129) up to the constant proportionality.

The equilibrium concentration can be obtained analytically (Fontaine & Michaud 1979). Setting the RHS of Eq. (4.127) zero (with $f = 0$), we get

$$\frac{\partial \ln c_2}{\partial r} - \left[\frac{A_2}{A_1}(1+Z_1) - Z_2 - 1\right] \frac{d\ln P}{d\ln r} = 0 \tag{4.137}$$

This immediately gives the power law solution

$$c_2(P) = c_2(P_0) \left(\frac{P}{P_0}\right)^{\delta}, \tag{4.138}$$

where $\delta = (A_2/A_1)(Z_1+1) - Z_2 - 1$ and P_0 is the pressure at some arbitrary point.

4.8 Discussion and Conclusions

The goal our study is to evolve the thermal structure and the chemical composition of a neutron star atmosphere from the earliest possible time to predict the innate chemical composition of the atmosphere. It turned out that the problem is complex, involving several ingredients such as determination of the evolving

atmosphere outside the neutrinosphere, cooling of a protoneutron star, nuclear reaction network at high temperatures, and the possible role of diffusion. We have attempted to explore the physics of all these ingredients. Although combining all these ingredients into a complete picture that can be used to predict the innate chemical composition of a neutron star atmosphere is our original goal, this goal has turned out to be beyond the scope of the thesis due to various uncertainities and complications. Nevertheless, our research into various components of the whole problem provides useful insight into the problem and lesson for future works.

Here is a direction for future works. As we have done in this chapter, one can separate the evolution of a neutron star atmosphere from that of the bulk of the neutron star. As we have seen in § 4.3.1, determining a static atmosphere for a young neutron star can be challenging since neutrinos tend to drive the static atmosphere into a wind. If one is able to make an atmosphere model whose temperature is high enough, the NSE composition can be used as the initial chemical composition and Timmes's "torch47" nuclear network can be used to handle the complicated nuclear reactions in the high temperature regime. It is to note, however, that "torch47" code only includes the thermal neutrino reactions in a single mass shell, other possible neutrino cooling/heating reactions and the energy transport across the mass shells should be appropriately taken into account. The evolution of the base atmosphere temperature is obtained in our simulation for up to 50 s from the birth of a protoneutron star. Diffusion will play an important role if the timescale of diffusion is comparable to or shorter than the timescales of nuclear reactions.

BIBLIOGRAPHY

[1] Aller, L. H. & Chapman, S. 1960, ApJ, 132, 461

[2] Alpar, M. A., & Shaham, J. 1985, Nature, 316, 239

[3] Aly, J. J. 1980, A&A, 86, 192

[4] Aly, J. J., & Kuijpers, J. 1990, A&A, 227, 473

[5] Angelini, L., Stella, L., & Parmar, A. N. 1989, ApJ, 346, 906

[6] Antia, H. M. 1993, ApJS, 84, 101

[7] Anzer, U., & Börner, G. 1980, A&A, 83, 133

[8] Anzer, U., & Börner, G. 1983, A&A, 122, 73

[9] Arzoumanian, Z., Chernoff, D. F., & Cordes, J. M. 2002, ApJ, 568, 289

[10] Bardeen, J. M., & Petterson, J. A. 1975, ApJ, 195, L65

[11] Bardeen, J. M., Press, W. H., & Teukolsky S. A. 1972, ApJ, 178, 347

[12] Bazan, G. & Arnett, D. 1994, ApJ, 433, L41

[13] Bildsten, L., Salpeter, E. E., & Wasserman, I. 1992, ApJ, 384, 143

[14] Bludman, S. A. & Van Riper, K. A. 1978, ApJ, 224, 631

[15] Boroson, B., et al. 2000, ApJ, 545, 399

[16] Burrows, A. & Lattimer, J. M. 1986, ApJ, 307, 178

[17] Campbell, C. G. 1997, Magnetohydrodynamics in Binary Stars (Kluwer, Dordrecht)

[18] Chakrabarty, D. 1998, ApJ, 492, 342

[19] Chakrabarty, D., et al. 2001, ApJ, 562, 985

[20] Chang, P. & Bildsten, L. 2003, ApJ, 585, 464

[21] Chang, P. & Bildsten, L. 2004, ApJ, 605, 830

[22] Chang, P., Arras, P., & Bildsten, L. 2004, ApJ, 616, L147

[23] Chatterjee, S., & Cordes, J. 2002, ApJ, 575, 407

[24] Chatterjee, S., Vlemmings, W. H. T., Cordes, J. M., & Chernoff, D. F. 2005, ApJ, submitted

[25] Chiu, H. Y. & Salpeter, E. E. 1964, Phys. Rev. Let., 15, 413

[26] Choi, C. S., Nagase, F., Makino, F., Dotani, T., & Min, K. W. 1994, ApJ, 422, 799

[27] Cordes, J. M., & Chernoff, D. F. 1998, ApJ, 505, 315

[28] Cumming, A., Zweibel, E. G., & Bildsten L. 2001, ApJ, 557, 958

[29] Duncan, R. C., Shapiro, L. S., & Wasserman, I. 1986, ApJ, 309, 141

[30] Fendt, C., & Elstner, D. 2000, A&A, 363, 208

[31] Finger, M. H., Wilson, R. B., & Harmon., B. A. 1996, ApJ, 459, 288

[32] Fontaine, G. & Michaud G. 1979, ApJ, 231, 826

[33] Ford, E. C., & van der Klis, M. 1998, ApJ, 506, L39

[34] Frank, J., King, A., & Raine, D. 1992, Accretion Power in Astrophysics (Cambridge University Press)

[35] Fryer, C., Burrows, A., & Benz, W. 1998, ApJ, 496, 333

[36] Ghosh, P., & Lamb, F. K. 1979, ApJ, 234, 296

[37] Ghosh, P., & Lamb, F. K. 1992, in X-Ray Binaries and Recycled Pulsars, ed. E. P. J. van den Heuval & S. A. Rappaport (Kluwer, Dordrecht), p.487

[38] Goldreich, P., Lai, D., & Sahrling, M. 1997, in Unsolved Problems in Astrophysics, ed. J. N. Bahcall & J. P. Ostriker (Princeton University Press)

[39] Goodson, A. P., Winglee, R. M., & Böhm, K.-H. 1997, ApJ, 489, 199

[40] Grove J. E., et al. 1995, ApJ, 438, L25

[41] Gunn, J. E., & Ostriker, J. P. 1970, ApJ, 160, 979

[42] Hansen, B. M. S., & Phinney, E. S. 1997, MNRAS, 291, 569

[43] Harding, A. K. & Lai, D. 2006, Repts. Prog. Phys., 69, 2631

[44] Harrison, E. R., & Tademaru, E. 1975, ApJ, 201, 447

[45] Hayashi, M. R., Shibata, K., & Matsumoto, R. 1996, ApJ, 468, L37

[46] Heger, A. 2004, private communication.

[47] Heindl, W. A., Coburn, W., Gruber, D. E., Pelling, M. R., & Rothschild, R. E. 1999, ApJ, 521, L49

[48] Ho, W. C. G. & Lai, D. 2001, MNRAS, 327, 1081

[49] Ho, W. C. G. & Lai, D. 2003, MNRAS, 338, 233

[50] Ho, W. C. G., Lai, D., Potekhin, A. Y., & Chabrier, G. 2003, ApJ, 599, 1293

[51] Hobbs, G., Lorimer, D. R., Lyne, A. G., & Kramer, M. 2005, MNRAS, 360, 974

[52] Homan, J., et al. 2002, ApJ, 568, 878

[53] Hwang, U., et al. 2004, ApJ, 615, 117

[54] Iben, I., & Tutukov, A. V. 1996, ApJ, 456, 738

[55] in't Zand, J. J. M., Baykal, A., & Strohmayer, T. E. 1998, ApJ, 496, 386

[56] Janka, H.-Th., Langanke, K., Marek, A., Martínez-Pinedo, G., & Müller, B. 2006, submitted to Bethe Centennial Volume of Physics Reports, also in astro-ph/0612072

[57] Janka, H.-Th., Scheck, L., Kifonidis, K., Muller, E., & Plewa, T. 2004, to be published in The Fate of the Most Massive Stars, Proc. Eta Carinae Science Symposium (Jackson Hole), also in astro-ph/0408439

[58] Jonker, P.G., et al. 2000, ApJ, 537, 374

[59] Kaspi, V. M., Bailes, M., Manchester, R. M., Stappers, B. W., & Bell, J. F. 1996, Nature, 381, 584

[60] Keil, W. & Janka, H.-Th. 1995, A&A, 296, 145

[61] Kramer, M. 1998, ApJ, 509, 856

[62] Kumar, P., & Quataert, E. J. 1997, ApJ, 479, L51

[63] La Barbera, A., Burderi, L., Di Salvo, T., Iaria, R., Robba, N. R. 2001, ApJ, 553, 375

[64] Lai , D. 1996, ApJ, 466, L35

[65] Lai, D. 1998, ApJ, 502, 721

[66] Lai, D. 1999, ApJ, 524, 1030

[67] Lai, D., Bildsten, L., & Kaspi, V. M. 1995, ApJ, 452, 819

[68] Lai, D., Lovelace, R., Wasserman, I. 1999, unpublished, in astro-ph/9904111

[69] Lai, D. & Qian, Y.-Z. 1998, ApJ, 495, L103

[70] Lai, D., Rasio, F. A., & Shapiro, S. L. 1993, ApJS, 88, 205

[71] Lai, D., Rasio, F. A., & Shapiro, S. L. 1994, ApJ, 423, 344

[72] Lamb, F. K., Shibazaki, N., Alpar, M. A., & Shaham, J. 1985, Nature, 317, 681

[73] Larwood, J. D., Nelson, R. P., Papaloizou, J. C. B., Terquem, C. 1996, MNRAS, 282, L597

[74] Li, J., Wickramasinge, D. T., & Rüdiger, G. 1996, ApJ, 469, 765.

[75] Lipunov, V. M., Semënov, E. S., & Shakura, N. I. 1981, Sov. Astron., 25, 439.

[76] Lorimer, D. R., Bailes, M., & Harrison, P. A. 1997, MNRAS, 289, 592

[77] Lovelace, R. V. E., Romanova, M. M., & Bisnovatyi-Kogan, G. S. 1995, MNRAS, 275, 244.

[78] Lovelace, R. V. E., Romanova, M. M., & Bisnovatyi-Kogan, G. S. 1999, ApJ, 514, 368

[79] Lyne, A. G., & Lorimer, D. R. 1994, Nature, 369, 127

[80] Makishima, K., & Mihara., T. 1992, in Proc. of Yamada Conf. 28, Frontiers of X-Ray Astronomy, ed. Y. Tanaka & K. Koyama (Universal Academy, Tokyo), 23

[81] Makishima, K., Mihara, T., Nagase, F., & Tanaka, Y. 1999, ApJ, 525, 978

[82] Makishima, K1990, ApJ, 365, L59

[83] Marković, D., & Lamb, F. K. 1998, ApJ, 507, 316

[84] Meyer, B. S. 1993, Phys. Rep., 227, 257

[85] Miller, K. A., & Stone, J. M. 1997, ApJ, 489, 890

[86] Moon, D-.S., & Eikenberry, S. S. 2001a, ApJ, 549, L225

[87] Moon, D-.S., & Eikenberry, S. S. 2001b, ApJ, 552, L135

[88] Morsink, S. M., & Stella, L. 1999, ApJ, 513, 827

[89] Murphy, J., Burrows, A., & Heger, A. 2004, ApJ, 615, 460

[90] Novikov, I. D., & Thorne, K. S. 1973, in Black Holes, ed. C. DeWitt & B. DeWitt (Gordon & Breach, New York), 343

[91] Ogilvie, G. I., & Dubus, G. 2001, MNRAS, 320, 485

[92] Ogilvie, G. I. 1999, MNRAS, 304, 557

[93] Ogilvie, G.I. 2000, MNRAS, 317, 607

[94] Ogilvie, G.I., & Dubus, G. 2001, MNRAS, 320, 485.

[95] Orlandini, M., et al. 1998, ApJ, 500, 163

[96] Papaloizou, J. C., & Pringle, J. E. 1983, MNRAS, 202, 1181

[97] Papaloizou, J. C., & Terquem, C. 1995, MNRAS, 274, 987

[98] Paul, B., & Rao, A. R. 1998, A&A, 337, 815

[99] Prakash, M., Lattimer, J. M., Pons, J. A., Steiner, A. W., & Sanjay, R. 2001, LNP, 578, 364

[100] Press, W. H., Teukolsky, S., Vetterling, W. T., & Flannery, B. P. 1992, Numerical Recipes (Cambridge University Press)

[101] Pringle, J. E. 1992, MNRAS, 258, 811

[102] Pringle, J. E. 1996, MNRAS, 281, 857

[103] Pringle, J. E., & Rees, M. J. 1972, A&A, 21, 1

[104] Psaltis, D., Belloni, T., & van der Klis, M. 1999, ApJ, 520, 262

[105] Psaltis, D., et al. 1999, ApJ, 520, 763

[106] Qian, Y.-Z., & Woosley, S. E. 1996, ApJ, 471, 331

[107] Remillard, R.A. 2001, in Evolution of Binary and Multiple Stars, eds. P. Podsiadlowski et al. (ASP, San Francisco), also in astro-ph/0103431

[108] Rosen, L. C. 1968, Ap & SS, 1, 327

[109] Rosen, L. C. 1969, Ap & SS, 5, 150

[110] Rosen, L. C., & Cameron, A. G. W. 1972, Ap & SS, 15, 137

[111] Salpeter, E. E. & Shapiro, S. L. 1981, ApJ, 251, 311

[112] Scheck, L., Plewa, T., Janka, H.-T., Kifonidis, K., & Muller, E. 2004, PRL, 92, 1103

[113] Shakura, N. I., & Sunyaev, R. A. 1973, A&A, 24, 337

[114] Shinoda, K., Kii, T., Mitsuda, K., Nagase, F., Tanaka, Y., Makishima, K., & Shibazaki, N. 1990, PASJ, 42, L27

[115] Shirakawa, A., & Lai, D. 2002, ApJ, 564, 361

[116] Shirakawa, A., & Lai, D. 2002, ApJ, 565, 1134

[117] Shu, F. H., et al. 1994, ApJ, 429, 781

[118] Soong, Y., & Swank, J. H. 1989, in Proc. 23rd ESLAB Symposium on Two Topics in X-ray Astronomy, ed. N. E. White, J. J. Hunt, & B. Battrick (ESA, Paris), 617

[119] Spruit, H. C., & Taam, R. E. 1993, ApJ, 402, 593

[120] Stairs, I. H., Manchester, R. N., Lyne, A. G., Kramer, M., Kaspi, V. M., Camilo, F., & D'Amico, N. 2003, "The Massive Binary Pulsar J1740-3052", in proceedings of Radio Pulsars, Astronomical Society of the Pacific

[121] Stella, L., & Vietri, M. 1998, ApJ, 492, L59

[122] Strohmayer, T. E. 2001, Advances in Space Research, also in astro-ph/0012516

[123] Takeshima, T., Dotani, T., Mitsuda, K., & Nagai, F. 1991, PASJ, 43, L43

[124] Takeshima, T., Dotani, T., Mitsuda, K., & Nagase, F. 1994, ApJ, 436, 871

[125] Tauris, T. M., Fender R. P., van den Heuvel, E. P. J., Johnston, H. M., & Wu K. 1999, MNRAS, 310, 1165

[126] Terquem, C. 1998, ApJ, 509, 819

[127] Terquem, C., & Papaloizou, J.C.B. 2000, A&A, 360, 1031

[128] Thompson, T. A., Burrows, A., & Meyer, B. S. 2001, ApJ, 562, 887

[129] Thorstensen, J. R., Fesen, R. A., & van den Bergh, S. 2001, AJ, 122, 297

[130] Timmes, F. X., 2003, `http://www.cococubed.com/codes_pages/`

[131] Timmes, F. X. 1999, ApJ, 124, 241

[132] Tubbs,D. L. & Schramm, D. N. 1975, ApJ, 201, 467

[133] Unno, W., Osaki, Y., Ando, H., Saio, H., and Shibahashi, H. 1989, Nonradial Oscillations of Stars, 2nd ed. (University of Tokyo Press)

[134] van Adelsberg, M., Lai, D., Potekhin, A. Y., & Arras, P. 2005, ApJ, 628, 902

[135] van Ballegooijen, A. A. 1994, Space Science Rev., 68, 299

[136] van den Heuvel E. P. J., & van Paradijs, J. 1997, ApJ, 483, 399

[137] van der Klis, M. 1995, in X-Ray Binaries, ed. W. H. G. Lewin, J. van Paradijs, & E. P. J. van den Heuvel (Cambridge University Press), 252

[138] van der Klis, M. 2000, ARAA, 38, 717

[139] van der Klis, M., et al. 1987, ApJ, 316, 411

[140] van Kerkwijk, M. H. & Kaplan, D. L. 2006, submitted to Ap & SS, also in astro-ph/067320

[141] Wang, C., Johnston, S., & Manchester, R. N. 2004, MNRAS, 351, 599

[142] Wang, C., Lai, D., & Han, J. L. 2006, ApJ, 639, 1007

[143] Wang, Y.-M. 1987, A&A, 183, 257

[144] Wang, Y.-M. 1995, ApJ, 449, L153

[145] Wex, N., Kalogera, V., & Kramer, M. 2000, ApJ, 528, 401

[146] Wijnands, R., & van der Klis, M. 1998 Nature, 394, 344

[147] Wijnands, R. A. D. et al. 1996, ApJ, 469, L5

[148] Wojdowski, P., Clark, G. W., Levine, A. M., Woo, J. W., & Zhang, S. N. 1998, ApJ, 502, 253

[149] Woosley, S. & Janka, T. 2005, Nature Physics 1, 147